



HAL
open science

Robust analysis under uncertainties of bladed disk vibration with geometrical nonlinearities and detuning

Anthony Picou

► **To cite this version:**

Anthony Picou. Robust analysis under uncertainties of bladed disk vibration with geometrical nonlinearities and detuning. Mechanical engineering [physics.class-ph]. Université Paris-Est, 2019. English. ⟨NNT : 2019PESC2038⟩. ⟨tel-02513425⟩

HAL Id: tel-02513425

<https://theses.hal.science/tel-02513425v1>

Submitted on 20 Mar 2020

HAL is a multi-disciplinary open access archive for the deposit and dissemination of scientific research documents, whether they are published or not. The documents may come from teaching and research institutions in France or abroad, or from public or private research centers.

L'archive ouverte pluridisciplinaire **HAL**, est destinée au dépôt et à la diffusion de documents scientifiques de niveau recherche, publiés ou non, émanant des établissements d'enseignement et de recherche français ou étrangers, des laboratoires publics ou privés.



HAL Authorization

Université Paris-Est Marne-la-Vallée
École doctorale Sciences, Ingénierie et Environnement

THÈSE

présentée et soutenue publiquement le 16 décembre 2019

pour l'obtention du

Doctorat de l'Université Paris-Est Marne-la-Vallée

Discipline: mécanique

par

Anthony Picou

Robust analysis under uncertainties of bladed-disk vibration with geometrical nonlinearities and detuning

Composition du jury

<i>Président :</i>	Jean-François Deü	Professeur – CNAM
<i>Rapporteurs :</i>	Didier Clouteau	Professeur – CentraleSupélec
	Jean-François Deü	Professeur – CNAM
<i>Examineurs :</i>	Évangéline Capiez-Lernout	Co-encadrante – UPEM
	Moustapha Mbaye	Ingénieur de recherche – Safran Tech
	Fabrice Thouverez	Professeur – Ecole Centrale Lyon
<i>Directeur de thèse :</i>	Christian Soize	Professeur – UPEM

Mis en page avec la classe thesul.

Acknowledgment

Je souhaite remercier tout d'abord les Professeurs Didier Clouteau et Jean-François Deü d'avoir accepté de rapporter mon manuscrit de thèse, ainsi que le Professeur Fabrice Thouverez d'avoir accepté d'examiner ma thèse, pour le temps qu'ils ont consacré à la lecture de ce manuscrit et leur participation au jury de ma thèse.

Mes remerciements vont à présent à mon directeur de thèse, le Professeur Christian Soize, pour sa rigueur et le temps qu'il m'a accordé durant ces 3 années de thèse. Je tiens également à remercier mes encadrants, Evangéline Capiez-Lernout et Moustapha Mbaye pour leur investissement, leur aide, et leurs conseils.

Je tiens également à remercier l'ensemble de Safran Tech, les permanents et non permanents du laboratoire MSME, plus particulièrement le bureau 118, Anthony, Brian, Justin, Quentin, Vincent, pour la très bonne ambiance qui y régnait et leur bonne humeur permanente.

Enfin, je tiens à remercier ma famille et Émilie pour leur présence et leur soutien.

Résumé

Le désaccordage intentionnel, plus communément appelé *detuning*, a été identifié comme une possible technologie pour réduire la sensibilité du comportement dynamique de roues aubagées soumises au désaccordage involontaire, aussi appelé *mistuning*, causé par les dispersions matérielle d'une aube à une autre engendrées lors du processus de fabrication et par la variabilité des propriétés mécaniques des matériaux. Le désaccordage intentionnel est mis en place par l'introduction de motifs à partir desquels différents types de secteurs générateurs, ayant des propriétés géométriques et matérielles différentes, sont assemblés. Cependant, les récentes innovations technologiques impliquant l'utilisation d'aubes de plus en plus flexibles et plus légères conduisent à de grands niveaux de déplacements et de déformations, requérant l'utilisation des équations dynamiques non linéaires tenant compte des non-linéarités géométriques. Ce travail est dédié à l'analyse robuste des effets des non-linéarités géométriques sur la dynamique non linéaire de roues aubagées désaccordées intentionnellement, en rotation, en présence de désaccordage involontaire. Le désaccordage involontaire correspond à des incertitudes dans le modèle numériques et sont prises en compte par une approche probabiliste. Cette thèse de nouveaux résultats concernant la dynamique non linéaire des roues aubagées désaccordées intentionnellement en présence de non-linéarités géométriques et en présence de désaccordage involontaire. Les analyses dynamiques sont effectuées dans le domaine temporel et analysées dans le domaine fréquentiel. L'analyse fréquentielle des réponses non-linéaires mettent en évidence des réponses significatives en dehors de la bande d'excitation. Les intervalles de confiance des réponses stochastiques permettent d'analyser la robustesse du modèle vis-à-vis des incertitudes, c'est-à-dire du niveau de désaccordage involontaire. La roue aubagées utilisée pour les simulations numériques est composée de 24 secteurs pour lesquels différents motifs de roues aubagées désaccordées intentionnellement sont analysés, avec ou sans désaccordage involontaire.

Abstract

The intentional mistuning, also called *detuning*, has been identified as an efficient technological way for reducing the sensitivity of the forced response of bladed-disks to unintentional mistuning (simply called *mistuning*), caused by the manufacturing tolerances and the small variations in the mechanical properties from blade to blade. The intentional mistuning consists in detuning the bladed-disk structure by using partial or alternating patterns of different sector types. However, the recent technological improvements that include the use of more flexible and lighter blades can lead to large strains/displacements, which requires the use of nonlinear dynamic equations involving geometric nonlinearities. This work is devoted to the robust analysis of the effects of geometric nonlinearities on the nonlinear dynamic behavior of rotating detuned bladed-disks in presence of mistuning. The detuning corresponds to uncertainties in the computational model, and are taken into account by a probabilistic approach. This thesis presents a series of novel results in dynamics of rotating bladed-disks with mistuning and detuning in presence of nonlinear geometrical effects. The structural responses are computed in the time domain and are analyzed in the frequency domain. The frequency analysis exhibits responses outside the frequency band of excitation. The confidence region of the stochastic responses allows the robustness to be analyzed with respect to uncertainties, that is to say with respect to the level of mistuning. The bladed-disk structure, which is used for the numerical simulations, is made up of 24 blades for which several different detuned patterns are investigated with and without mistuning.

Contents

List of Figures	ix
List of Tables	xv
1 Introduction	1
1.1 Context of research	1
1.1.1 Mistuning definition	1
1.1.2 Combining detuning and mistuning	3
1.1.3 Effects of geometric nonlinearities	4
1.2 Objectives of research	7
1.3 Organization of the manuscript and definition of the used terminology	8
2 Nonlinear dynamics of rotating detuned bladed-disks	11
2.1 Introduction	11
2.2 Notations	12
2.3 Dynamic problem of a rotating detuned bladed-disk	13
2.3.1 Assumptions and terminology	13
2.3.2 Nonlinear boundary value problem in the rotating frame . .	14
2.3.3 Weak formulation of the nonlinear boundary value problem .	16
2.3.4 Expression and properties of the linear and multilinear forms	17
2.4 Finite element discretization	20
2.4.1 Linear and nonlinear finite element model of the detuned bladed-disk structure	20
2.4.2 Block writing of the matrices related to a given sector type .	21
2.4.3 Particular case of the tuned bladed-disk structure	23
3 Construction of the nominal (or mean) nonlinear reduced-order model	25
3.1 Introduction	25

3.2	First NonLinear Reduced-Order Model (NL-ROMF) for a detuned bladed-disk	27
3.3	Second nonlinear reduced-order model (NL-ROM) for a detuned bladed-disk	28
4	Nonlinear computational dynamics of a detuned bladed-disk structure	31
4.1	Introduction	32
4.2	Computational model for the tuned and for the detuned bladed-disk structure	32
4.2.1	Computational model of the tuned bladed-disk structure	32
4.2.2	Computational model of the detuned bladed-disk structure	35
4.3	Modal analysis of the rotating tuned bladed-disk structure and numerical validation	35
4.3.1	Modal analysis	35
4.3.2	Numerical validation	36
4.4	Nonlinear deterministic analysis	37
4.4.1	Definition of the external load (excitation)	37
4.4.2	Definition of the observations	41
4.4.3	Numerical aspects	44
4.4.4	Convergence analysis with respect to the dimension of the NL-ROM	44
4.4.5	Sensitivity analysis of the deterministic responses for the nonlinear tuned rotating bladed-disk with respect to amplitude s_0 of the excitation	46
4.4.6	Linear and nonlinear dynamic analyses in the time domain using the L-ROM and NL-ROM	48
4.4.7	Analysis of the nonlinear dynamic time responses in the frequency domain	49
5	Probabilistic model of mistuning	53
5.1	Introduction	54
5.2	Ensemble SG_0^+ of positive-definite random matrices	54
5.2.1	Available information	54
5.2.2	Probability distribution of random matrix $[\mathbf{G}]$	55
5.2.3	Dispersion parameter	55
5.2.4	Algebraic representation of random matrix $[\mathbf{G}]$	56
5.3	Ensemble SE_0^+ of positive-definite random matrices	56

5.4	Construction of linear and nonlinear stochastic reduced-order models	57
5.4.1	Global stiffness matrix	57
5.4.2	Stochastic nonlinear reduced-order model NL-SROM1 of a rotating detuned bladed-disk structure with mistuning . . .	57
5.4.3	Stochastic nonlinear reduced-order model NL-SROM2 of a rotating detuned bladed-disk structure with mistuning . . .	59
5.4.4	Stochastic linear reduced-order model L-SROM of a rotating detuned bladed-disk with mistuning	59
6	Nonlinear stochastic computational dynamics	61
6.1	Introduction	61
6.2	Convergence analyses	62
6.2.1	Convergence analysis with respect to \tilde{N}_K	62
6.2.2	Stochastic convergence analysis with respect to n_s	63
6.3	Linear and nonlinear stochastic analyses	65
6.3.1	Random dynamic amplification	65
6.3.2	Sensitivity analysis with respect to parameter s_0 for the rotating tuned and detuned bladed-disk structure in presence of mistuning	65
6.3.3	Stochastic analysis of nonlinear rotating tuned and detuned bladed-disk structure in presence of mistuning for different patterns	72
6.4	Discussion	72
7	Robust nonlinear computational dynamics	75
7.1	Introduction	75
7.2	Detuned bladed-disk structure without mistuning	76
7.3	Stochastic analysis of nonlinear structures	76
7.4	Robust analysis with respect to sub-frequency bands	79
8	Quantitative nonlinear analysis in terms of modal participation	83
8.1	Introduction	83
8.2	Nonlinear deterministic analyses related to modes 2B and 1T	84
8.3	Stochastic nonlinear analyses of modes 2B and 1T	84
8.4	Quantification concerning the energy transfer according to the modal excitation	86
	Conclusion and Perspectives	91

A	Construction of the geometric stiffness matrix	93
B	Table of patterns	95
C	Implementation of three 3D finite elements in the house-code	97
C.1	Hexahedral finite element with 20 nodes	97
C.1.1	Interpolation functions	98
C.1.2	Numerical integration points	99
C.2	Pyramidal elements with 13 nodes	101
C.2.1	Interpolation functions	102
C.2.2	Numerical integration points	103
C.3	Tetrahedral element with 10 nodes	104
C.3.1	Interpolation functions	104
C.3.2	Numerical integration points	104
	Bibliography	107

List of Figures

1.1	Amplification factors from measurement results [1]	2
1.2	Variation of the maximum amplification factor with respect to the rate of mistuning [2]	3
1.3	Blade undergoing small (grey blade) and large displacements (blue blade)	5
1.4	Amplification factor with respect to the mistuning rate: the continuous curves with circles (and non continuous curves with triangles) are related to the tuned (and detuned) bladed-disk structure. The lower, middle, and upper curves correspond respectively to a probability level $p=0.50$, $p=0.95$, and $p=0.99$). From [3].	8
2.1	Reference configuration of the bladed-disk structure in the rotating frame	15
2.2	Blade sector	21
4.1	Finite element model of the bladed-disk with 24 blades in which the dot symbols (red color) correspond to the excitation points (left figure). Zoom of the finite element model of a sector (right figure).	33
4.2	Zoom of the finite element sector: grey, red and green finite elements are respectively related to hexahedral, pyramidal, and tetrahedral finite elements	33
4.3	Tuned bladed-disk structure $\mathcal{P}_0 = 24A$ (left figure) and detuned bladed-disk configuration $\mathcal{P}_{31} = (6A6B)_2$ with red blade for B and blue blade for A (right figure).	35
4.4	Graph of $\Omega \mapsto \nu_\alpha(\Omega)$ defining the Campbell diagram of the eigenfrequencies (in Hz) of the linear tuned rotating bladed-disk structure (pattern \mathcal{P}_0) as a function of the rotation speed (in RPM), where EO denotes the engine order, and where the vertical dashed line identifies the speed of rotation that is considered.	37

4.5	Graph of $h \mapsto \nu_\alpha(h)$ of the eigenfrequencies ν_α of the linear tuned rotating bladed-disk structure (pattern \mathcal{P}_0) for rotation speed $\Omega = 4440$ RPM as a function of the circumferential wave number h	38
4.6	Representation of the mode shapes of the tuned rotating bladed-disk structure for circumferential wave number $h = 4$. First bending mode related to eigenfrequency $\nu_1 = 484$ Hz (left figure) and second bending mode related to eigenfrequency $\nu_2 = 1170$ Hz (right figure)	39
4.7	Representation of the mode shapes of the tuned rotating bladed-disk structure for circumferential wave number $h = 4$. First torsional mode related to eigenfrequency $\nu_3 = 1490$ Hz (left figure) and third bending mode related to eigenfrequency $\nu_4 = 2234$ Hz (right figure)	39
4.8	Graph of function $\alpha \mapsto Err(\alpha)$ corresponding to the case $\Omega = 0$ rad.s ⁻¹ (blue line) and to the case $\Omega = 1000$ rad.s ⁻¹ (red line)	40
4.9	Definition of the excitation: graph of the time-function excitation, $t \mapsto g(t)$, defines on interval $[-0.065, 0.18]$ s (top figure) and zoom on $[-0.02, 0.02]$ s interval (down figure).	42
4.10	Graph of function $\nu \mapsto \widehat{g}(2\pi\nu) $ in log scale.	43
4.11	Convergence analysis with respect to the reduced order m of the NL-ROMF: graphs of function $m \mapsto Conv_1(m)$ for patterns $\mathcal{P}_0 = 24A$, $\mathcal{P}_2 = (AB)_{12}$, and $\mathcal{P}_{13} = 6B12A3B3A$	45
4.12	Convergence analysis with respect to the reduced order N of the NL-ROM for $m = 145$: graphs of function $N \mapsto Conv_2(m, N)$ for patterns $\mathcal{P}_0 = 24A$, $\mathcal{P}_2 = (AB)_{12}$, and $\mathcal{P}_{13} = 6B12A3B3A$	46
4.13	Sensitivity analysis with respect to parameter s_0 using the NL-ROMF for the nonlinear tuned rotating bladed-disk structure (pattern $\mathcal{P}_0 = 24A$): graph of function $s_0 \mapsto i_{NL}(s_0)$. The red dashed line represents the boundary between the linear and nonlinear regimes	47
4.14	Sensitivity analysis with respect to parameter s_0 of the responses computed with the NL-ROMF and analyzed in the frequency domain: graphs of function $\nu \mapsto \ \widehat{\mathbf{u}}^{j_0}(2\pi\nu)\ $ for $s_0 = 0.04$ (left top figure), $s_0 = 0.25$ (right top figure), $s_0 = 1$ (left down figure), and $s_0 = 4.0$ (right down figure). The light yellow zone corresponds to the excitation frequency band \mathbb{B}_e	48

4.15	Zoom on the time interval $[-0.01, 0.1]$ s of the linear dynamic analysis in the time domain performed with the L-ROM: graph of function $t \mapsto u_{2,L}^{j_0}(t)$ defined on the time interval $[-0.05, 1.5]$ s for the patterns \mathcal{P}_0 (left top figure), \mathcal{P}_6 (right top), \mathcal{P}_{11} (left down), and \mathcal{P}_{25} (right down).	49
4.16	Zoom on the time interval $[-0.01, 0.1]$ s of the nonlinear dynamic analysis in the time domain performed with the NL-ROM: graph of function $t \mapsto u_{2,NL}^{j_0}(t)$ defined on the time interval $[-0.05, 1.5]$ s for the patterns \mathcal{P}_0 (left top figure), \mathcal{P}_6 (right top), \mathcal{P}_{11} (left down), and \mathcal{P}_{25} (right down).	50
4.17	Frequency analysis of the time responses computed with the NL-ROM: graphs of functions $\nu \mapsto b_L(2\pi\nu)$ (red smooth thin lines) and $\nu \mapsto b_{NL}(2\pi\nu)$ (blue irregular thick lines) for patterns \mathcal{P}_0 (left top figure), \mathcal{P}_6 (right top figure), \mathcal{P}_{11} (left down figure), and \mathcal{P}_{25} (right down figure). The excitation frequency band \mathbb{B}_e is in light grey area.	51
6.1	Convergence analysis with respect to parameter \tilde{N}_K : graph of function $\tilde{N}_K \mapsto \text{err}(\tilde{N}_K)$ in log-scale.	63
6.2	Convergence analysis with respect to the number n_s of realizations for the Monte-Carlo numerical simulation of the NL-SROM1: graph of function $n_s \mapsto \text{Conv}(n_s)$	64
6.3	For $\delta_K = 0.1$, graphs of function $s_0 \mapsto \hat{u}_{\max}(s_0)$ such that $\text{Proba}\{\hat{U}_{\max}(s_0) \leq \hat{u}_{\max}(s_0)\} \leq 0.95$ for the tuned rotating bladed-disk structure (pattern \mathcal{P}_0) and for the detuned pattern \mathcal{P}_6 . Calculation with L-SROM (red line with crosses) and with NL-SROM2 (blue line with circles).	67
6.4	For $\delta_K = 0.1$, confidence region (yellow region) of $\nu \mapsto \ \hat{U}^{j_0}(2\pi\nu)\ $ corresponding to a probability level 0.95, computed using NL-SROM2 for the tuned rotating bladed-disk structure (pattern \mathcal{P}_0) and for $s_0 = 0.01$. The dashed-line is the response of the deterministic nominal (mean) model. The vertical grey region corresponds to excitation frequency band \mathbb{B}_e . Linear scale (left figure) and log scale (right figure)	68
6.5	For $\delta_K = 0.1$, confidence region (yellow region) of $\nu \mapsto \ \hat{U}^{j_0}(2\pi\nu)\ $ corresponding to a probability level 0.95, computed using NL-SROM2 for the detuned pattern \mathcal{P}_6 and for $s_0 = 0.01$. The dashed-line is the response of the deterministic nominal (mean) model. The vertical grey region corresponds to excitation frequency band \mathbb{B}_e . Linear scale (left figure) and log scale (right figure)	68

- 6.6 For $s_0 = 0.15$ and for $\delta_K = 0.1$, confidence region (yellow region) of $\nu \mapsto \|\widehat{\mathbf{U}}^{j_0}(2\pi\nu)\|$ corresponding to a probability level 0.95, computed using NL-SROM2 for the tuned rotating bladed-disk structure (pattern \mathcal{P}_0). The dashed-line is the response of the deterministic nominal (mean) model. The vertical grey region corresponds to excitation frequency band \mathbb{B}_e . Linear scale (left figure) and log scale (right figure) 69
- 6.7 For $s_0 = 0.15$ and for $\delta_K = 0.1$, confidence region (yellow region) of $\nu \mapsto \|\widehat{\mathbf{U}}^{j_0}(2\pi\nu)\|$ corresponding to a probability level 0.95, computed using NL-SROM2 for detuned pattern \mathcal{P}_6 and for $s_0 = 0.15$. The dashed-line is the response of the deterministic nominal (mean) model. The vertical grey region corresponds to excitation frequency band \mathbb{B}_e . Linear scale (left figure) and log scale (right figure) 69
- 6.8 For $s_0 = 1$ and for $\delta_K = 0.1$, confidence region (yellow region) of $\nu \mapsto \|\widehat{\mathbf{U}}^{j_0}(2\pi\nu)\|$ corresponding to a probability level 0.95, computed using NL-SROM2 for the tuned rotating bladed-disk structure (pattern \mathcal{P}_0). The dashed-line is the response of the deterministic nominal (mean) model. The vertical grey region corresponds to excitation frequency band \mathbb{B}_e . Linear scale (left figure) and log scale (right figure) 70
- 6.9 For $s_0 = 1$ and for $\delta_K = 0.1$, confidence region (yellow region) of $\nu \mapsto \|\widehat{\mathbf{U}}^{j_0}(2\pi\nu)\|$ corresponding to a probability level 0.95, computed using NL-SROM2 for detuned pattern \mathcal{P}_6 . The dashed-line is the response of the deterministic nominal (mean) model. The vertical grey region corresponds to excitation frequency band \mathbb{B}_e . Linear scale (left figure) and log scale (right figure) 70
- 6.10 For $s_0 = 1$, graphs of function $\delta_K \mapsto b_L^{+, \infty}(\delta_K)$ for tuned pattern \mathcal{P}_0 and detuned ones, $\mathcal{P}_2, \mathcal{P}_3, \mathcal{P}_5, \mathcal{P}_6, \mathcal{P}_{12}$, and \mathcal{P}_{31} defined in Appendix B. 71
- 6.11 For $s_0 = 1$ and for $\delta_K = 0.03$, confidence region (yellow region) of the random amplification factor, $B_{\text{NL}}(2\pi\nu)$, estimated with a probability level of 0.95 using NL-SROM1, for the tuned rotating bladed-disk structure (pattern \mathcal{P}_0) (left top figure), and for detuned patterns, \mathcal{P}_6 (right top), \mathcal{P}_{11} (left down), and \mathcal{P}_{25} (right down). The dashed-line is the nominal amplification factor $b_{\text{NL}}(2\pi\nu)$. The vertical grey region corresponds to excitation frequency band \mathbb{B}_e 73

6.12	For $s_0 = 1$ and for $\delta_K = 0.1$, confidence region (yellow region) of the random amplification factor, $B_{\text{NL}}(2\pi\nu)$, estimated with a probability level of 0.95 using NL-SROM1, for the tuned rotating bladed-disk structure (pattern \mathcal{P}_0) (left top figure), and for detuned patterns, \mathcal{P}_6 (right top), \mathcal{P}_{11} (left down), and \mathcal{P}_{25} (right down). The dashed-line is the nominal amplification factor $b_{\text{NL}}(2\pi\nu)$. The vertical grey region corresponds to excitation frequency band \mathbb{B}_e	74
7.1	For $s_0 = 1$, graphs of functions $\nu \mapsto b_{\text{NL}}^{\pm}(2\pi\nu)$ (black irregular thick lines) and $\nu \mapsto b_{\text{NL}}^{\text{tuned}}(2\pi\nu)$ (red irregular thin line) corresponding to the upper (+) and the lower (-) envelopes of the dynamic amplification factor among the investigated patterns. Linear scale (top figure) and log scale (down figure)	77
7.2	For $\delta_K = 0.1$ and $s_0 = 1$, confidence region (yellow/grey region) of the random amplification factor, $B_{\text{NL}}^{\text{all}}(2\pi\nu)$, related to the 46 patterns, estimated with a probability level of 0.95 using NL-SROM1. The dashed-line is the amplification factor $b_{\text{NL}}^{\text{tuned}}(2\pi\nu)$ of the tuned system without mistuning. The thick solid line is the median value of random variable $B_{\text{NL}}^{\text{all}}(2\pi\nu)$. The vertical grey region corresponds to excitation frequency band \mathbb{B}_e . Linear scale (top figure), log scale (down figure)	78
7.3	For $s_0 = 1$ and for band \mathbb{B}_{med} , lower (thin solid line) and upper (thick solid line) envelopes of the regions containing the 46 graphs of functions $\delta_K \mapsto b_{\text{NL}}^{+, \infty, \text{med}}(\delta_K)$ for the 46 patterns using NLSROM1. The upper envelope corresponds to detuned pattern \mathcal{P}_{33} and the lower one to detuned pattern \mathcal{P}_1	80
7.4	For $s_0 = 1$ and for band \mathbb{B}_{low} , lower (thin solid line) and upper (thick solid line) envelopes of the regions containing the 46 graphs of functions $\delta_K \mapsto b_{\text{NL}}^{+, \infty, \text{low}}(\delta_K)$ for the 46 patterns using NLSROM1. The upper envelope corresponds to detuned pattern \mathcal{P}_{26} and the lower one to detuned pattern \mathcal{P}_{37}	81
7.5	For $s_0 = 1$ and for band \mathbb{B}_{high} , lower (thin solid line) and upper (thick solid line) envelopes of the regions containing the 46 graphs of functions $\delta_K \mapsto b_{\text{NL}}^{+, \infty, \text{high}}(\delta_K)$ for the 46 patterns using NLSROM1. The upper envelope corresponds to detuned pattern \mathcal{P}_9 and the lower one to \mathcal{P}_8	81

8.1	For $s_0 = 1$, frequency analysis of the time responses related to mode 1B (left figure) and mode 1T (right figure). In each figure, the computation with the L-ROM is in red color and with the NL-ROM in blue color: graph of function $\nu \mapsto \ \widehat{\mathbf{u}}^{j_0}(2\pi\nu)\ $ for the tuned rotating bladed-disk structure (pattern \mathcal{P}_0). The excitation frequency band \mathbb{B}_e is in light grey area.	85
8.2	For $s_0 = 1$ and for $\delta_K = 0.1$, confidence region (yellow/grey region) of $\nu \mapsto \ \widehat{\mathbf{U}}^{j_0}(2\pi\nu)\ $ corresponding to a probability level 0.95, computed using NL-SROM1 for the tuned rotating bladed-disk structure (pattern \mathcal{P}_0) related to mode 2B (left figure) and mode 1T (right figure). The dashed-line is the response of the deterministic mean (nominal) model. The vertical grey region corresponds to excitation frequency band \mathbb{B}_e	85
8.3	Graph of the evolution of the ratio $\mathcal{R}(\nu_\alpha)$ with respect to the rotation speed Ω	86
8.4	Graphs of function $\nu \mapsto \ \widehat{\mathbf{u}}^{j_0}(2\pi\nu)\ $ for $s_0 = 0.05$ (left figure) and $s_0 = 0.3$ (right figure). The light blue zone corresponds to the excitation frequency band \mathbb{B}_e	87
8.5	Graphs of function $\nu \mapsto \ \widehat{\mathbf{u}}^{j_0}(2\pi\nu)\ $ for $s_0 = 0.7$ (left figure) and $s_0 = 1$ (right figure). The light blue zone corresponds to the excitation frequency band \mathbb{B}_e	88
8.6	Graphs of function $\nu \mapsto \ \widehat{\mathbf{u}}^{j_0}(2\pi\nu)\ $ for $s_0 = 0.05$ (left figure) and $s_0 = 0.3$ (right figure). The light blue zone corresponds to the excitation frequency band \mathbb{B}_e	88
8.7	Graphs of function $\nu \mapsto \ \widehat{\mathbf{u}}^{j_0}(2\pi\nu)\ $ for $s_0 = 0.7$ (left figure) and $s_0 = 1$ (right figure). The light blue zone corresponds to the excitation frequency band \mathbb{B}_e	89
C.1	20-node solid finite element.	98
C.2	13-node solid finite element	102
C.3	10-node solid finite element	104

List of Tables

4.1	Geometric characteristics of the bladed-disk structure	34
4.2	Element, nodes, and dofs of the finite element model	34
4.3	Numerical integration points used by ANSYS commercial finite element software	34
C.1	Interpolation functions related to the HEX20 finite element	99
C.2	Localization of the 27 numerical integration points in the HEX20 finite element	100
C.3	Localization of the 14 numerical integration points in the HEX20 finite element	101
C.4	Interpolation functions related to the PYR13 finite element	102
C.5	Localization of the 6 numerical integration points in the PYR13 finite element	103
C.6	Interpolation functions related to the TET10 finite element	105
C.7	Localization of the 4 numerical integration points in the TET10 finite element	105

List of Tables

Chapter 1

Introduction

Contents

1.1	Context of research	1
1.1.1	Mistuning definition	1
1.1.2	Combining detuning and mistuning	3
1.1.3	Effects of geometric nonlinearities	4
1.2	Objectives of research	7
1.3	Organization of the manuscript and definition of the used terminology	8

1.1 Context of research

1.1.1 Mistuning definition

In this section, we briefly recall the origins of the mistuning phenomenon in bladed-disk structure and how it affects their dynamic behavior. Typically, a bladed-disk is an assembly of blade sectors designed to be identical from one to another one. However, there are unavoidable variations and discrepancies in the structural properties of individual blades due to manufacturing tolerances, material or geometric discrepancies. Such a phenomenon is called mistuning. These variations modify the natural frequencies of the bladed-disk structure from its nominal design. Research about the origins of mistuning phenomenon in bladed-disk structures has first been investigated in the 1960's [4, 5]. Then, Whitehead investigated the influence of mistuning on the forced vibration behavior of bladed-disk structures [6].

This pioneered work has been followed by those of Ewins [7], Dye and Henry [8], where the amplification factor has been introduced in order to measure the consequences of the mistuning into the dynamic response. This amplification factor is defined as the ratio of the two following quantities. The first one is the highest forced response of a given mistuned bladed-disk structure. The second one is the highest forced response level of the tuned bladed-disk structure submitted to the same excitation [9]. The uncertainties associated with the structural, material, manufacturing, and assembly characteristics of a bladed-disk structure, affect the modal properties of the tuned system. The eigenfrequencies and the mode shapes are modified [7, 10]. The presence of mistuning could possibly lead to mode localization, in which the blades vibration energy is transferred and confined to only one or few blades [11], inducing larger dynamic amplitudes compared to the tuned one [12, 13, 14, 15]. Localization phenomenon has received wide attention in the literature. It appears in various types of engineering structures, such as the small disordering of periodic truss beams [16, 17], and of cyclic structures [18, 19, 1] (cf Figure 1.1). Hodge [10] showed that the mode localization of a bladed-disk struc-

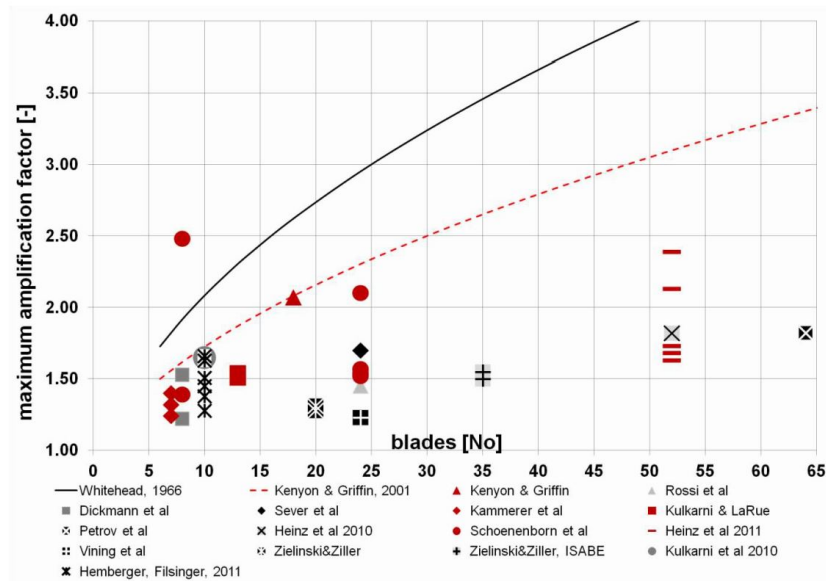


Figure 1.1 – Amplification factors from measurement results [1]

ture becomes worse either with increasing mistuning levels, or by decreasing the mechanical coupling between blades. The role played by inter-blade coupling has also been investigated by Ottarsson and Pierre [11]. They showed that a weak coupling could significantly increase the forced response amplitudes, each blade acting

as an isolated part avoiding of the vibration energy to be transferred between the other blades whereas a very strong inter-blade coupling allows the energy to be spacially distributed, and therefore reducing the possibility of mode localization. Previous work published in [11, 20] also indicates that the sensitivity of the forced response to mistuning is associated with the frequency-veering region. When there is mistuning, the modes in the veering region tend to generate a disk-blade motion yielding a strong inter-blade coupling and then a mode localization with a significant dynamic amplitudes levels [21]. Furthermore, the mode localization strongly depends on the mistuning levels of the blades, and the maximum amplitude factor is very sensitive to small perturbations levels. Indeed, in references [7] and [21], it has been proved that the maximum amplitude of the blade disk dynamic response increases with the increasing of the mistuning only up to a certain level, after which mistuning leads to lower forced response amplitudes. An example of such phenomenon is shown in Figure 1.2 [2].

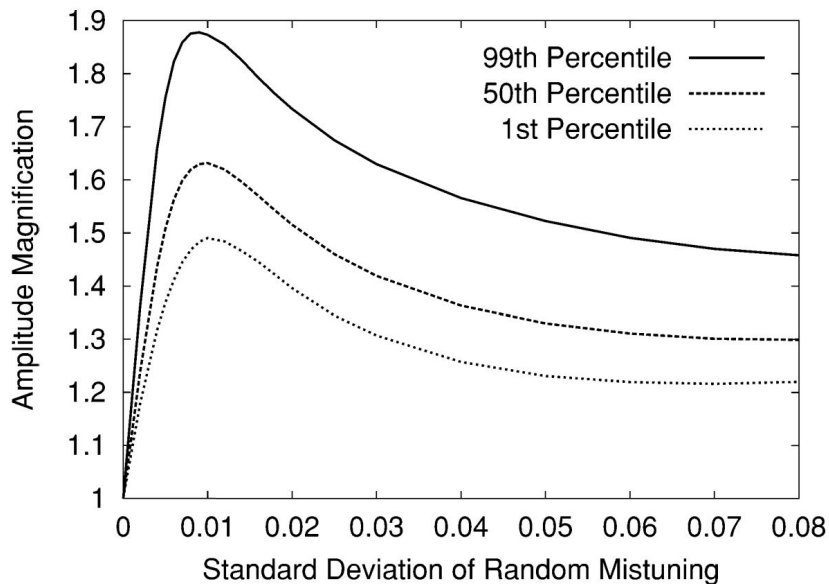


Figure 1.2 – Variation of the maximum amplification factor with respect to the rate of mistuning [2]

1.1.2 Combining detuning and mistuning

The detuning (called intentional mistuning) consists in voluntarily breaking the cyclic symmetry of a tuned bladed-disk that is only made up from a given *gen-*

erating sector. The breaking is obtained by substituting one or several sectors of the tuned bladed-disk by a *perturbed sector*. A perturbed sector is obtained by modifying the geometry and or the mechanical properties of the generating sector. A given assembly of sectors is defined as a pattern.

Such a strategy has been shown to be efficient for mitigating the harmful effects generated by the mistuning. Indeed, it has been reported that the maximum blade forced response levels can be decreased by detuning the tuned design [22, 23, 24, 25]. Using two or more designs of blades with nominally different natural frequencies can make the detuned bladed-disk structure more robust with respect to the mistuning effects [3]. However, the effectiveness of such strategy, which consists in detuning the tuned design strongly depends on the selected pattern [26, 27, 28, 29, 30, 31, 32, 33, 34]. In order to select the detuned pattern leading to the smallest dynamic amplification, a design optimization can be performed. It should be noted that the optimization of the detuning, which consists in finding the optimal pattern, requires the calculation of a very large number of detuned patterns in presence of mistuning, that is to say, using a stochastic computation model. Consequently, the computational cost becomes very large for a bladed-disk made up with a large number of blades. More recently, the technological improvements that include the use of more flexible and lighter blades can lead to large strains/displacements (as shown in Figure 1.3) so that the linearization of the dynamic equations can no longer be used. In this context, the geometric nonlinearities have to be taken into account as proposed in [35], and there is a growing interest for including geometric nonlinearities in the dynamic analyses of detuned bladed-disks.

1.1.3 Effects of geometric nonlinearities

Research dealing with geometric nonlinearities have been mainly focused on geometric nonlinear problems of beams, plates, and shells [36, 37, 38, 39]. Moreover, one can find a lot of scientific literature about theoretical and numerical algorithms adapted to such context. Among them, we can cite books from Belytschko [40, 41], Bonet [42] and Crisfield [43]. Nowadays, because of the use of more lighter, more slender, and more flexible structural components, the structure may undergo large displacements in structural dynamics and for fluid-structure interactions.

In the framework of cyclic structures, the effects of nonlinearities on the dynamics have first been considered by [44] for a simple generic cyclic structure exhibiting nonlinear stiffness connections (and not for nonlinear geometric effects,

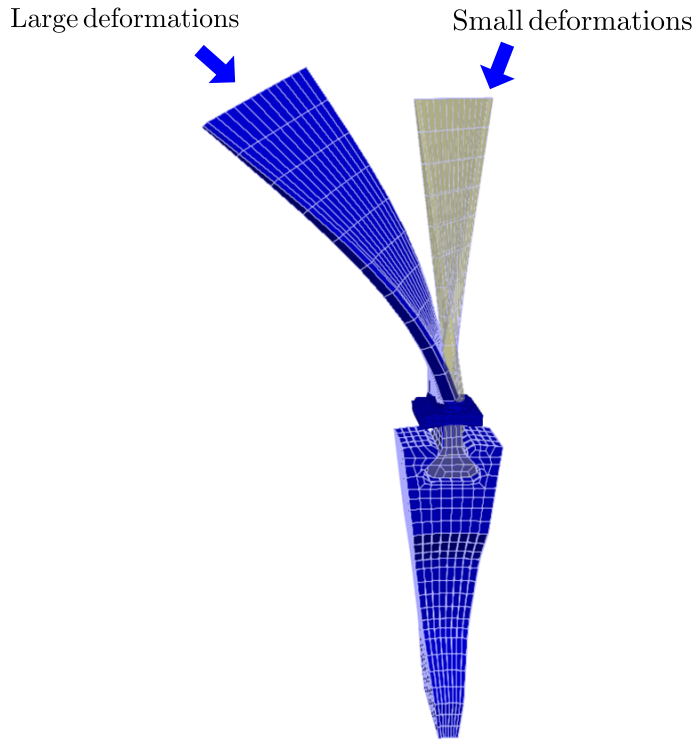


Figure 1.3 – Blade undergoing small (grey blade) and large displacements (blue blade)

and furthermore, without mistuning). For the nonlinear dynamic analysis of rotating bladed-disk structures with flexible blades, geometric nonlinearities can no longer be neglected [35, 45, 46]. Note that the need to accurately predict the dynamic response of such geometric nonlinear dynamical systems becomes essential for the designer.

In the framework of cyclic geometric structures, many research have been carried out in order to include local nonlinearities such as dry friction [47, 48, 49, 50, 51, 52]. Furthermore, due to the complexity of modern structures with cyclic geometry, large finite element computational models are needed. Consequently, research on the construction of adapted nonlinear reduced-order models for bladed-disk structures have also been largely investigated [53, 54, 55, 56, 57, 58, 59].

One of strategy that can be used for constructing nonlinear reduced-order models is the Stiffness Evaluation Procedure (STEP) proposed in [60, 61], which is applicable to a wide class of problems carried out with commercial finite element codes having a geometrically nonlinear static capability. The methodology is based on the use of a standard commercial finite element code for which no further nu-

merical development is needed, only requiring a series of nonlinear static computations with prescribed displacements [62, 63]. Such method has been used in several contexts (see for instance, [64, 65, 66, 67]). In the framework of the STEP method, methodologies for constructing non-intrusive reduced-order models have been reviewed by [61].

Another approach for analyzing nonlinear dynamical systems is the Harmonic Balance Method (HBM) (see for instance [68] for friction problems and [69] for geometric nonlinear problems). In 2011, Grolet *et al* investigated nonlinear systems with cyclic symmetry submitted to geometric nonlinearities [70] followed by the work presented in [71] and solved by using HBM. Note that all these works do not take into account neither detuning nor mistuning phenomena. Likewise, Martin *et al* proposed in [72] an investigation of a stator vane composed of nonlinear beams subjected to nonlinear effects and proposes an original coupling of several methods used for the study of nonlinear systems. The nonlinear effects of each substructure are reduced by using linear normal modes (LNMs) completed with modal derivatives (MD) [73, 74]. The reduced nonlinear stiffnesses associated with the basis are determined using the STEP method [60, 75]. The nonlinear effects exhibits strong localizations on the structure at low amplitudes, which must be avoided to ensure the integrity of the components.

The classical Proper Orthogonal Decomposition (POD) method is an efficient tool for constructing the vector basis, which allows nonlinear reduced-order models to be constructed [76, 77, 78, 79, 80, 81, 82], and which is commonly used in many applications.

For nonlinear dynamic systems, another overview concerning the construction of vector bases used for obtaining the reduced-order model has been carried out in [83], where the robustness and the performance of these bases are investigated. More recently, an autonomous geometric nonlinear reduced-order model for studying the solution of complex rotating structures has been presented in [84, 85]. For that purpose, the linear normal modes basis is used for the construction of the reduced-order model, the STEP method is applied to compute the nonlinear forces, and the assumption of nonlinear perturbations around the static equilibrium is considered. In [86], a methodology is presented to calculate the nonlinear dynamic response of cyclic structures undergoing large vibratory deformation under a traveling wave excitation using a double-sector model and transient dynamic analysis.

Some other works on the field of geometric nonlinearities with application on beam [87], coupled dynamic system [88], curved structure [89] and compos-

ite blades [90] have also been carried out.

In this work, the nonlinear reduced-order model is constructed using a novel approach. It consists in introducing a double projection approach [45, 46] followed by the use of the POD method for constructing the final vector basis. In addition, an explicit approach is used for directly constructing the reduced linear, quadratic, and cubic stiffness operators of the mean nonlinear computational model [91, 89, 35]. Such approach allows for analyzing industrial rotating integrally bladed-disks in order to quantify the impact of the nonlinear geometrical effects on the detuned-mistuned structure, in terms of dynamic amplification of the responses and of uncertainty propagation.

1.2 Objectives of research

As explained above, nonlinear complex phenomena remain to be understood and analyzed in order to integrate these new concepts in industrial issues, in particular concerning optimization problems. Moreover, the uncertainty quantification and numerical errors is nowadays recognized as necessary to improve the robustness of predictions for design optimization. Lot of studies have been conducted in the framework of the linear dynamic analysis for which the mistuning effects have been modeled using either parametric probabilistic approaches (see for instance, [24, 92, 93, 94, 95]), or using the nonparametric probabilistic approach ([96, 97, 98, 99]), and for which the optimization of alternating patterns has been studied (see for instance, [30, 100, 3, 32]). More recently, nonparametric probabilistic approach has been used for nonlinear structural vibration with nonlinear geometric effects [91, 89, 35, 101]. Blade optimization problems in nonlinear dynamics with nonlinear geometric effects and with uncertainty quantification is today considered as a real need for aeronautical industry. In this context, this research follows the works proposed in [102, 103], in which tuned and detuned bladed-disks in presence of mistuning have been investigated in the context of the linear dynamics. Particularly, it has been shown in [3] that detuning is an efficient technology to reduce the dynamic amplification due to the mistuning phenomena, as shown in Figure 1.4. This present work is devoted to the robust analysis of the effects of geometric nonlinearities on the nonlinear dynamic behavior of rotating detuned bladed-disk structures in presence of mistuning. The bladed-disk structure results from an assembly of reference sectors that constitute a given detuned pattern for which the dynamic analysis is carried out. Mistuning is taken into account

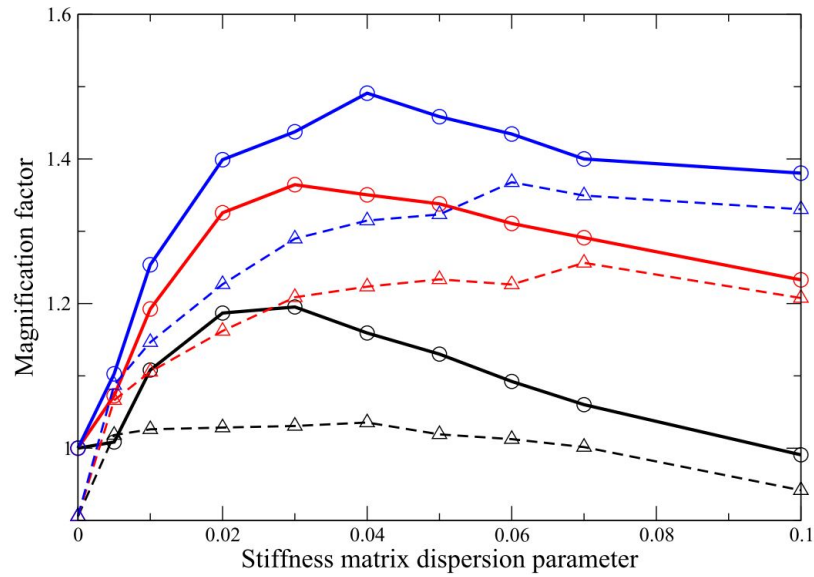


Figure 1.4 – Amplification factor with respect to the mistuning rate: the continuous curves with circles (and non continuous curves with triangles) are related to the tuned (and detuned) bladed-disk structure. The lower, middle, and upper curves correspond respectively to a probability level $p=0.50$, $p=0.95$, and $p=0.99$). From [3].

in the computational model by the nonparametric probabilistic approach [104, 99]. A complete methodology adapted to the robust dynamic analysis of rotating detuned bladed-disk structures in presence of both geometric nonlinear effects and mistuning is presented. The corresponding computational tool is constructed in an industrial context that involves large computational models. A series of novel results are then presented.

1.3 Organization of the manuscript and definition of the used terminology

Chapter 2 is devoted to the formulation of the nonlinear boundary value problem for a rotating detuned bladed-disk structure. This allows for constructing the weak formulation that is suitable for the use of the finite element method. We then obtain a nominal (mean) nonlinear computational model that will be called the **NonLinear High-Fidelity computational Model (NL-HFM)**. Its linear counterpart will be called the **Linear High-Fidelity computational Model**

(L-HFM)

Chapter 3 presents the construction of an adapted reduced-order basis, using a double projection method. A first *modal basis* is computed by solving the generalized eigenvalue problem associated with the L-HFM for which the gyroscopic coupling is neglected. By projecting the NL-HFM on the subspace spanned by this modal basis, we then obtain a **First NonLinear Reduced-Order Model (NL-ROMF)**. Another *vector basis* is then calculated using the Proper-Orthogonal Decomposition (POD) method from the nonlinear solution of the NL-ROMF. The final NL-ROM is then obtained by double projection of the NL-HFM. In the present context, it is necessary to explicitly construct all the nonlinear stiffness contributions related to the NL-ROM, in agreement with the use of the nonparametric probabilistic strategy.

In Chapter 4, four patterns corresponding to one tuned and three detuned configurations of an industrial rotating bladed-disk structure are analyzed in details. In particular, convergence analyses allow for optimizing the size of the NL-ROM. Such NL-ROM is then used for analyzing the sensitivity of the nonlinear response with respect to the load intensity that controls the amount of geometric nonlinearities. In this latter context, a comparison of the dynamical responses is performed between the linear case and the nonlinear one, in both time and frequency domain.

Chapter 5 is devoted to the construction of the **NonLinear Stochastic Reduced-Order Model (NL-SROM)**, based on the use of the nonparametric probabilistic approach.

In Chapter 6, convergence analyses are carried out with respect to the number of Monte-Carlo simulations and to the dimension of the random matrix germ for constructing the stochastic solution of the NL-SROM. The confidence regions of the stochastic dynamic responses allow for quantifying the robustness with respect to the level of uncertainties, that is to say with respect to the level of mistuning.

Chapter 7 presents a robust nonlinear dynamic analysis of the tuned, of the detuned, and of the mistuned-detuned rotating bladed-disk structure. The detuned cases consists in analyzing 46 patterns. The frequency analysis of the time responses is presented on a broad frequency band that is written as an interval union of three sub-frequency bands. The variability of the responses for these 46

mistuned patterns is analyzed in details.

The last chapter proposes a quantitative nonlinear analysis in terms of modal contribution. For the present industrial computational model, the mechanisms governing the different modal contributions are proposed.

This last Chapter is followed by a conclusion and perspective section, followed by three appendices: the first one is devoted to the construction of the geometric stiffness matrix; the second one defines the patterns, and finally the last one is devoted to the implementation of the 3D finite element in the house code.

Chapter 2

Nonlinear dynamics of rotating detuned bladed-disks

Contents

2.1	Introduction	11
2.2	Notations	12
2.3	Dynamic problem of a rotating detuned bladed-disk	13
2.3.1	Assumptions and terminology	13
2.3.2	Nonlinear boundary value problem in the rotating frame	14
2.3.3	Weak formulation of the nonlinear boundary value problem	16
2.3.4	Expression and properties of the linear and multilinear forms	17
2.4	Finite element discretization	20
2.4.1	Linear and nonlinear finite element model of the detuned bladed-disk structure	20
2.4.2	Block writing of the matrices related to a given sector type	21
2.4.3	Particular case of the tuned bladed-disk structure	23

2.1 Introduction

This chapter is devoted to the formulation of the dynamics of rotating detuned bladed-disks undergoing large displacements inducing nonlinear geometric effects. In section 2.3 the nonlinear boundary value problem and its weak formulation are

written. In section 2.4, the finite element method is used for discretizing the weak formulation in order to construct the nonlinear dynamic computational model.

As explained in Section 1, the detuned bladed-disk structure consists in voluntarily breaking the cyclic symmetry of the tuned bladed-disk that is made up of one given *generating sector*. The breaking is obtained by substituting in this tuned bladed-disk, one or several sectors by a *perturbed sector* (different from the generating sector). A perturbed sector is obtained by modifying the geometry and/or the mechanical properties of the blade of this sector. A given assembly of sectors is defined as a pattern. The construction of the computational model is obtained by assembling the computational model of each sector type. Note that the mesh of the computational model of two consecutive sectors is assumed to be compatible at their common interface. Such strategy allows for constructing the nominal (mean) nonlinear computational model for a given rotating detuned bladed-disk structure. As previously explained, this nonlinear computational model is referred as the **NonLinear High-Fidelity computational Model (NL-HFM)**. Similarly, the corresponding linear computational model is referred as the **Linear High-Fidelity computational Model (L-HFM)** (see Section 1.3).

2.2 Notations

For a better readability of the manuscript, the following notations are used.

- A real deterministic scalar is denoted by a lower case letter (for instance a)
- A real-valued random variable is denoted by an upper case letter (for instance A)
- A real deterministic vector is denoted by a boldface lower case letter (for instance $\mathbf{a} = (a_1, \dots, a_n)$)
- A real-valued random vector is denoted by a boldface upper case letter (for instance $\mathbf{A} = (A_1 \dots A_n)$)
- A real deterministic matrix is denoted by a lower or an upper case letter between brackets (for instance $[a]$ or $[A]$)
- A real-valued random matrix is denoted by a boldface upper case letter between brackets (for instance $[\mathbf{A}]$)
- A tensor is denoted by a blackboard letter (for instance $\mathbb{A} = \{\mathbb{A}_{ij}\}_{ij}$ for a second-order tensor or $\mathbb{A} = \{\mathbb{A}_{ijkl}\}_{ijkl}$ for a fourth-order tensor)

Furthermore, the convention of summation over repeated latin indices is generally used. For instance,

$$\mathbf{a} \cdot \mathbf{b} = \sum_{i=1}^n a_i b_i \quad \text{is written as} \quad a_i b_i \quad (2.1)$$

$$\{\mathbb{A} \mathbf{b}\}_i = \sum_{j=1}^n A_{ij} b_j \quad \text{is written as} \quad A_{ij} b_j \quad (2.2)$$

$$\mathbb{A} : \mathbb{B} = \sum_{i=1}^n \sum_{j=1}^n A_{ij} B_{ij} \quad \text{is written as} \quad A_{ij} B_{ij} \quad (2.3)$$

2.3 Dynamic problem of a rotating detuned bladed-disk

2.3.1 Assumptions and terminology

Although the terminology of the "tuned", "detuned", and "mistuned" has been defined in Section 1.3, for the sake of clarity and for helping the reading, we reintroduce below the terminology while defining the assumptions.

1. The **tuned structure** is related to the *conceptual structure*, which exhibits a perfect M -order *cyclic symmetry*. For this configuration denoted as \mathcal{P}_0 , the geometry, the constitutive equation of material, and the boundary conditions related to the reference sector are invariant under the $\frac{2\pi}{M}$ rotation around its symmetry axis, which corresponds to the rotational axis of the bladed-disk. In the case of a linear dynamic analysis, only one reference sector can be used and analyzed for deducing the linear dynamic response (L-HFM) of the rotating bladed-disk, introducing an appropriate phase-lag condition on the boundary [105, 106, 107].
2. The **detuned structure** (or **intentionally mistuned structure**) is related to the *conceptual structure* for which there is a *spatial distribution of different types of sectors*, defining a pattern. In the present work, two different sector types, denoted as A and B, are considered. These two sector types have identical geometry and differ by the material properties of the blades. The detuned structure is thus defined by an assembly of these two sector types. For a rotating bladed-disk with $M = 24$ blades, a pattern will

be defined, for instance, by 12B6A3B3A, which consists of 12 consecutive blades of type *B*, 6 of type *A*, 3 of type *B*, and 3 of type *A*.

3. The **mistuned structure** is related to the *real structure* that is manufactured from the *conceptual structure* (tuned structure). The **mistuned structure** is the tuned structure for which the cyclic symmetry is broken by discrepancies occurring during the manufacturing process. In this work, the **mistuning** phenomenon is modeled by using the nonparametric probabilistic approach of uncertainties [99].
4. The **detuned-mistuned structure** is the detuned structure in which there is mistuning.

The following hypothesis are introduced.

- H1 The bladed-disk is in rotation around its rotational axis at a constant rotation speed Ω (*rad/s*). The rotational axis has a fixed direction and consequently, there is no rigid body motion of the disk.
- H2 The boundary value problem of the rotating bladed-disk is written in the rotating frame.
- H3 The bladed-disk is made up of an elastic material that is modeled by the Saint Venant-Kirchhoff constitutive equation. A damping term will arbitrarily be added at the weak-formulation level of the conservative boundary value problem.
- H4 The amplitude of the external forces expressed in the rotating frame is assumed to be sufficiently large so that the structure undergoes geometric nonlinear effects.

2.3.2 Nonlinear boundary value problem in the rotating frame

We are interested in considering the nonlinear boundary value problem of the rotating detuned bladed-disk, considered as a structure in rotation. The boundary value problem is written in the rotating frame. In this rotating frame, a total Lagrangian formulation is used and the nonlinear dynamic equations are expressed with respect to a reference configuration (reference configuration that is defined in the rotating frame). Let \mathcal{R} be the rotating frame (cartesian coordinates system) and let $(O, \mathbf{e}_1, \mathbf{e}_2, \mathbf{e}_3)$ be its related basis. The rotation axis of the bladed-disk is defined as (O, \mathbf{e}_3) that is fixed. Let \mathcal{D} be the three-dimensional bounded open

domain corresponding to such reference configuration in the rotating frame and subjected to the body force field $\mathbf{g}(\mathbf{x}, t) = (g_1(\mathbf{x}, t), g_2(\mathbf{x}, t), g_3(\mathbf{x}, t))$, in which $\mathbf{x} = (x_1, x_2, x_3)$ denotes the position of a given point belonging to domain \mathcal{D} . The boundary $\partial\mathcal{D}$ is such that $\partial\mathcal{D} = \Gamma \cup \Sigma$ with $\Gamma \cap \Sigma = \emptyset$. The external unit normal to boundary $\partial\mathcal{D}$ is denoted by $\mathbf{n} = (n_1, n_2, n_3)$. The boundary part Γ corresponds to the fixed part of the structure (in the rotating frame) whereas the boundary part Σ is subjected to the external surface force field $\mathbf{G}(\mathbf{x}, t) = (G_1(\mathbf{x}, t), G_2(\mathbf{x}, t), G_3(\mathbf{x}, t))$. Note that, in the rotating frame, the external force fields are derived from the Lagrangian transport into the reference configuration of the physical body/surface. We then introduce the (3×3) rotation matrix $[R(\Omega)]$ that is written as

$$[R(\Omega)] = \begin{bmatrix} 0 & -\Omega & 0 \\ \Omega & 0 & 0 \\ 0 & 0 & 0 \end{bmatrix}, \quad (2.4)$$

in which Ω is the rotation speed.

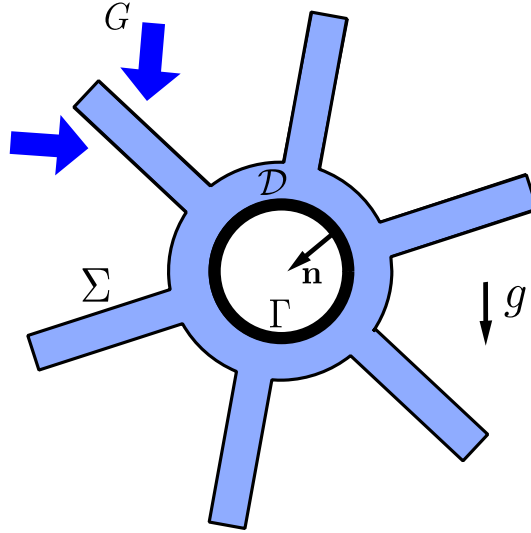


Figure 2.1 – Reference configuration of the bladed-disk structure in the rotating frame

Under the hypotheses H1 to H4 defined in Section 2.3.1, and in the rotating frame, the unknown displacement field is denoted as $\mathbf{u}(\mathbf{x}, t) = (u_1(\mathbf{x}, t), u_2(\mathbf{x}, t), u_3(\mathbf{x}, t))$ and is solution of the following nonlinear boundary value problem [108, 109, 110, 111], which is written, for $i = 1, 2, 3$, as

$$\rho \frac{\partial^2 u_i}{\partial t^2} + 2\rho [R]_{ij} \frac{\partial u_j}{\partial t} + \rho [R]_{ij} [R]_{jk} (x_k + u_k) - \frac{\partial}{\partial x_j} (\mathbb{F}_{ik} \mathbb{S}_{kj}) = g_i, \quad \forall \mathbf{x} \in \mathcal{D}, \quad (2.5)$$

$$\mathbb{F}_{ik}\mathbb{S}_{kj}n_j = G_i, \forall \mathbf{x} \in \Sigma, \quad (2.6)$$

$$u_i = 0, \forall \mathbf{x} \in \Gamma, \quad (2.7)$$

in which ρ is the mass density and where the second-order deformation gradient tensor \mathbb{F} is defined by

$$\mathbb{F}_{ij} = \frac{\partial u_i}{\partial x_j} + \delta_{ij}, \quad (2.8)$$

with δ_{ij} the Kronecker symbol such that $\delta_{ij} = 1$ if $i = j$ and 0 otherwise. The second-order Piola-Kirchhoff symmetric stress tensor \mathbb{S} can be decomposed as

$$\mathbb{S}_{ij} = \sigma_{ij}^{\text{geom}} + \mathbb{I}_{ij} \quad (2.9)$$

where σ^{geom} is the second-order prestress tensor induced by the centrifugal loads and where \mathbb{I} is the second-order symmetric stress tensor such that [108]

$$\mathbb{I}_{ij} = \mathfrak{c}_{ijkl}\mathbb{E}_{kl}. \quad (2.10)$$

In Eq. (2.10), \mathfrak{c} is the fourth-order elasticity tensor that is symmetric and positive definite and \mathbb{E} is the Green strain tensor that is written as

$$\mathbb{E}_{ij}(\mathbf{u}) = \mathfrak{e}_{ij}(\mathbf{u}) + \mathfrak{n}_{ij}(\mathbf{u}), \quad (2.11)$$

in which

$$\mathfrak{e}_{ij}(\mathbf{u}) = \frac{1}{2} \left(\frac{\partial u_i}{\partial x_j} + \frac{\partial u_j}{\partial x_i} \right), \quad \mathfrak{n}_{ij}(\mathbf{u}) = \frac{1}{2} \frac{\partial u_s}{\partial x_i} \frac{\partial u_s}{\partial x_j} \quad (2.12)$$

The second-order prestress tensor σ^{geom} is calculated from the following static boundary value problem that corresponds to the equilibrium of the reference configuration (in the rotating frame) submitted to the static centrifugal body forces and is written [108], for $i = 1, 2, 3$, as

$$\frac{\partial}{\partial x_j} \sigma_{ij}^{\text{geom}} = \rho [R]_{ij} [R]_{jk} x_k, \forall \mathbf{x} \in \mathcal{D}, \quad (2.13)$$

$$\sigma_{ij}^{\text{geom}} n_j = 0, \forall \mathbf{x} \in \Sigma, \quad (2.14)$$

$$u_i = 0, \forall \mathbf{x} \in \Gamma. \quad (2.15)$$

2.3.3 Weak formulation of the nonlinear boundary value problem

Let \mathcal{C}_{ad} be the space of the admissible displacements defined by

$$\mathcal{C}_{\text{ad}} = \{ \mathbf{x} \mapsto \mathbf{v}(\mathbf{x}) : \mathcal{D} \rightarrow \mathbb{R}^3, \mathbf{v} \text{ sufficiently regular, } \mathbf{v} = 0 \text{ on } \Gamma \}. \quad (2.16)$$

The weak formulation of the boundary value problem defined by Equation (2.5) to (2.12), with the arbitrarily linear damping term (see hypothesis H3), consists in finding the unknown displacement field $\mathbf{u}(\cdot, t)$ in \mathcal{C}_{ad} such that, for all \mathbf{v} in \mathcal{C}_{ad} ,

$$m(\ddot{\mathbf{u}}, \mathbf{v}) + c(\dot{\mathbf{u}}, \mathbf{v}) + d(\dot{\mathbf{u}}, \mathbf{v}) + k_e(\mathbf{u}, \mathbf{v}) + k_c(\mathbf{u}, \mathbf{v}) + k_g(\mathbf{u}, \mathbf{v}) + k_2(\mathbf{u}, \mathbf{u}, \mathbf{v}) + k_3(\mathbf{u}, \mathbf{u}, \mathbf{u}, \mathbf{v}) = \ell(\mathbf{v}), \quad (2.17)$$

in which $\dot{\mathbf{u}} = \partial\mathbf{u}/\partial t$ and $\ddot{\mathbf{u}} = \partial^2\mathbf{u}/\partial t^2$. The expressions and the properties of the linear, bilinear, and multilinear forms are detailed below. Furthermore, it is recalled that the external forces induced by the aerodynamics coupling forces are not taken into account in this work.

2.3.4 Expression and properties of the linear and multilinear forms

External loads

The linear form $\ell(\mathbf{v})$ defined on \mathcal{C}_{ad} , related to the external loads is such that

$$\ell(\mathbf{v}) = \int_{\mathcal{D}} \mathbf{g} \cdot \mathbf{v} \, d\mathbf{x} + \int_{\Sigma} \mathbf{G} \cdot \mathbf{v} \, ds_{\mathbf{x}} \quad (2.18)$$

Mass

The bilinear form $m(\mathbf{u}, \mathbf{v})$ defined on $\mathcal{C}_{\text{ad}} \times \mathcal{C}_{\text{ad}}$, related to the mass,

$$m(\mathbf{u}, \mathbf{v}) = \int_{\mathcal{D}} \rho \mathbf{u} \cdot \mathbf{v} \, d\mathbf{x}, \quad (2.19)$$

is symmetric and positive definite,

$$m(\mathbf{u}, \mathbf{v}) = m(\mathbf{v}, \mathbf{u}) \quad , \quad m(\mathbf{u}, \mathbf{u}) > 0. \quad (2.20)$$

Elastic stiffness

The bilinear form $k_e(\mathbf{u}, \mathbf{v})$ defined on $\mathcal{C}_{\text{ad}} \times \mathcal{C}_{\text{ad}}$, related to the elastic stiffness,

$$k_e(\mathbf{u}, \mathbf{v}) = \int_{\mathcal{D}} (\mathfrak{a}(\mathbf{x}) : \mathfrak{e}(\mathbf{u})) : \mathfrak{e}(\mathbf{v}) \, d\mathbf{x}, \quad (2.21)$$

is symmetric and positive definite,

$$k_e(\mathbf{u}, \mathbf{v}) = k_e(\mathbf{v}, \mathbf{u}) \quad , \quad k_e(\mathbf{u}, \mathbf{u}) > 0. \quad (2.22)$$

Geometric stiffness

The bilinear form $k_g(\mathbf{u}, \mathbf{v})$ defined on $\mathcal{C}_{\text{ad}} \times \mathcal{C}_{\text{ad}}$, related to the geometric stiffness,

$$k_g(\mathbf{u}, \mathbf{v}) = \int_{\mathcal{D}} \mathbb{G}^{\text{geom}} : \left(\frac{\partial \mathbf{u}^T}{\partial \mathbf{x}} \frac{\partial \mathbf{v}}{\partial \mathbf{x}} \right) d\mathbf{x}, \quad (2.23)$$

is symmetric,

$$k_g(\mathbf{u}, \mathbf{v}) = k_g(\mathbf{v}, \mathbf{u}). \quad (2.24)$$

The notation $\partial \mathbf{u} / \partial \mathbf{x}$ means the second-order tensor such that $\{\partial \mathbf{u} / \partial \mathbf{x}\}_{ij} = \partial u_i / \partial x_j$.

Centrifugal stiffness

The bilinear form $k_c(\mathbf{u}, \mathbf{v})$ defined on $\mathcal{C}_{\text{ad}} \times \mathcal{C}_{\text{ad}}$, related to the centrifugal stiffness,

$$k_c(\mathbf{u}, \mathbf{v}) = \int_{\mathcal{D}} \rho ([R]^2 \mathbf{u}) \cdot \mathbf{v} d\mathbf{x}, \quad (2.25)$$

is symmetric and negative semi-definite (as $[R]$ is skew-symmetric and not invertible matrix),

$$k_c(\mathbf{u}, \mathbf{v}) = k_c(\mathbf{v}, \mathbf{u}) \quad , \quad k_c(\mathbf{u}, \mathbf{u}) \leq 0. \quad (2.26)$$

Let $k_1(\mathbf{u}, \mathbf{v})$ be the bilinear form defined on $\mathcal{C}_{\text{ad}} \times \mathcal{C}_{\text{ad}}$ such that

$$k_1(\mathbf{u}, \mathbf{v}) = k_e(\mathbf{u}, \mathbf{v}) + k_c(\mathbf{u}, \mathbf{v}) + k_g(\mathbf{u}, \mathbf{v}). \quad (2.27)$$

It can be seen that $k_1(\mathbf{u}, \mathbf{v})$ is symmetric and is generally not positive definite. However, it will be assumed that this symmetric bilinear form is positive definite,

$$k_1(\mathbf{u}, \mathbf{v}) = k_1(\mathbf{v}, \mathbf{u}) \quad , \quad k_1(\mathbf{u}, \mathbf{u}) > 0. \quad (2.28)$$

For rotating bladed-disk structures, such hypothesis is reasonable considering that the operating regime associated with a given rotation speed Ω ensures the stability of the bladed-disk.

Damping

The arbitrarily linear damping term, which has been added to the weak formulation of the conservative system, is defined by the positive-definite symmetric bilinear form $d(\mathbf{u}, \mathbf{v})$ on $\mathcal{C}_{\text{ad}} \times \mathcal{C}_{\text{ad}}$, according to a Rayleigh model, which is written as

$$d(\mathbf{u}, \mathbf{v}) = \alpha m(\mathbf{u}, \mathbf{v}) + \beta k_e(\mathbf{u}, \mathbf{v}), \quad (2.29)$$

in which α and β are constant that are adjusted according to the critical damping rate coherent with the chosen elastic material. We then have

$$d(\mathbf{u}, \mathbf{v}) = d(\mathbf{v}, \mathbf{u}) \quad , \quad d(\mathbf{u}, \mathbf{u}) > 0. \quad (2.30)$$

Quadratic stiffness

The multilinear form $k_2(\mathbf{u}, \mathbf{v}, \mathbf{w})$ defined on $\mathcal{C}_{\text{ad}} \times \mathcal{C}_{\text{ad}} \times \mathcal{C}_{\text{ad}}$, related to the quadratic stiffness, is such that

$$k_2(\mathbf{u}, \mathbf{v}, \mathbf{w}) = \widehat{k}_2(\mathbf{u}, \mathbf{v}, \mathbf{w}) + \widehat{k}_2(\mathbf{v}, \mathbf{w}, \mathbf{u}) + \widehat{k}_2(\mathbf{w}, \mathbf{u}, \mathbf{v}) \quad (2.31)$$

where

$$\widehat{k}_2(\mathbf{u}, \mathbf{v}, \mathbf{w}) = \frac{1}{2} \int_{\mathcal{D}} \left(\mathbb{Q} : \left(\frac{\partial \mathbf{u}^T}{\partial \mathbf{x}} \frac{\partial \mathbf{v}}{\partial \mathbf{x}} \right) \right) : \frac{\partial \mathbf{w}}{\partial \mathbf{x}} d\mathbf{x}, \quad (2.32)$$

and satisfies the property

$$\widehat{k}_2(\mathbf{u}, \mathbf{v}, \mathbf{w}) = \widehat{k}_2(\mathbf{v}, \mathbf{u}, \mathbf{w}). \quad (2.33)$$

Consequently we have

$$k_2(\mathbf{u}, \mathbf{u}, \mathbf{v}) = \widehat{k}_2(\mathbf{u}, \mathbf{u}, \mathbf{v}) + 2\widehat{k}_2(\mathbf{v}, \mathbf{u}, \mathbf{u}). \quad (2.34)$$

Cubic stiffness

The multilinear form $k_3(\mathbf{u}, \mathbf{v}, \mathbf{w}, \mathbf{r})$ defined on $\mathcal{C}_{\text{ad}} \times \mathcal{C}_{\text{ad}} \times \mathcal{C}_{\text{ad}} \times \mathcal{C}_{\text{ad}}$, related to the cubic stiffness,

$$k_3(\mathbf{u}, \mathbf{v}, \mathbf{w}, \mathbf{r}) = \frac{1}{2} \int_{\mathcal{D}} \left(\mathbb{Q} : \left(\frac{\partial \mathbf{u}^T}{\partial \mathbf{x}} \frac{\partial \mathbf{v}}{\partial \mathbf{x}} \right) \right) : \left(\frac{\partial \mathbf{w}^T}{\partial \mathbf{x}} \frac{\partial \mathbf{r}}{\partial \mathbf{x}} \right), \quad (2.35)$$

satisfies the properties

$$k_3(\mathbf{u}, \mathbf{v}, \mathbf{w}, \mathbf{r}) = k_3(\mathbf{u}, \mathbf{v}, \mathbf{r}, \mathbf{w}) = k_3(\mathbf{w}, \mathbf{r}, \mathbf{u}, \mathbf{v}) \quad , \quad k_3(\mathbf{u}, \mathbf{v}, \mathbf{v}, \mathbf{u}) > 0. \quad (2.36)$$

Gyroscopic coupling

The bilinear form $c(\mathbf{u}, \mathbf{v})$ defined on $\mathcal{C}_{\text{ad}} \times \mathcal{C}_{\text{ad}}$, related to the gyroscopic coupling,

$$c(\mathbf{u}, \mathbf{v}) = 2 \int_{\mathcal{D}} \rho ([R]\mathbf{u}) \cdot \mathbf{v} d\mathbf{x}, \quad (2.37)$$

is skew-symmetric (since $[R]$ is skew-symmetric)

$$c(\mathbf{u}, \mathbf{v}) = -c(\mathbf{v}, \mathbf{u}) \quad , \quad c(\mathbf{u}, \mathbf{u}) = 0. \quad (2.38)$$

2.4 Finite element discretization

2.4.1 Linear and nonlinear finite element model of the detuned bladed-disk structure

The weak formulation related to the nonlinear boundary value problem is discretized using the finite element method [112, 113]. The unknown displacement field \mathbf{u} is approximated by projecting \mathbf{u} in the n -dimension subspace $\tilde{\mathcal{C}}_{\text{ad}}$ of \mathcal{C}_{ad} , spanned by the n basis functions $\mathbf{e}_1, \dots, \mathbf{e}_n$ deduced from the interpolation functions of the finite elements,

$$\mathbf{u}(\mathbf{x}) \simeq \sum_{i=1}^n U_i \mathbf{e}_i(\mathbf{x}), \quad (2.39)$$

where U_1, \dots, U_n are the degrees-of-freedom (dofs) of the finite element model. Let $\mathbf{U} = (U_1, \dots, U_n)$ be the vector in \mathbb{R}^n of all the dofs. For notational reasons, \mathbf{U} will be noted \mathbf{u} (the same notation will be used for the continuous field and its discretization; there will be no possible confusion). The nonlinear computational model of the detuned bladed-disk structure, which is identified as the NL-HFM, is written as,

$$[M] \ddot{\mathbf{u}}(t) + ([D] + [C(\Omega)]) \dot{\mathbf{u}}(t) + [K_1(\Omega)] \mathbf{u}(t) + \mathbf{f}^{\text{NL}}(\mathbf{u}(t)) = \mathbf{f}(t), \quad (2.40)$$

in which the $(n \times n)$ matrix $[K_1(\Omega)]$ is defined by

$$[K_1(\Omega)] = [K_e] + [K_c(\Omega)] + [K_g(\Omega)], \quad (2.41)$$

and is assumed to be symmetric positive definite. The mass, damping, and stiffness $(n \times n)$ real matrices $[M]$, $[D]$, $[K_e]$ are positive definite, the geometric stiffness $(n \times n)$ real matrix $[K_g(\Omega)]$ is symmetric, the gyroscopic coupling $(n \times n)$ real matrix $[C(\Omega)]$ is skew-symmetric, and the centrifugal stiffness $(n \times n)$ real matrix $[K_c(\Omega)]$ is negative semi-definite. More precisely, matrix $[K_g(\Omega)]$ corresponds to the discretization of the bilinear form $k_g(\mathbf{u}, \mathbf{v})$ that comes from the term $\rho[R]_{ij}[R]_{jk}x_k$ in Equation (2.5), matrix $[K_c(\Omega)]$ corresponds to the discretization of the bilinear form $k_c(\mathbf{u}, \mathbf{v})$ that comes from the term $\rho[R]_{ij}[R]_{jk}u_k$, and matrix $[C(\Omega)]$ corresponds to the discretization of the bilinear form $c(\mathbf{u}, \mathbf{v})$ that comes from the term $2\rho[R]_{ij}\frac{\partial u_j}{\partial t}$.

Their block writing is presented in Section 2.4.2. The \mathbb{R}^n -vector $\mathbf{f}(t)$ is the external force vector depending on time issued from the finite element discretization of the surface and body force fields. The \mathbb{R}^n -vector $\mathbf{f}^{\text{NL}}(\mathbf{u}(t))$ describes the

nonlinear internal forces induced by the geometric nonlinearities and issued from the quadratic and cubic stiffness terms. The corresponding linear high-fidelity model (L-HFM) is defined similarly to Eq.(2.40) by removing the nonlinear term $\mathbf{f}^{\text{NL}}(\mathbf{u}(t))$ and is written as

$$[M] \ddot{\mathbf{u}}(t) + ([D] + [C(\Omega)]) \dot{\mathbf{u}}(t) + [K_1(\Omega)] \mathbf{u}(t) = \mathbf{f}(t). \quad (2.42)$$

2.4.2 Block writing of the matrices related to a given sector type

The detuned bladed-disk structure is constituted of M sectors, which are assumed to be geometrically identical (their material properties can differ). In the rotating frame, let us consider a reference sector number j , that is composed of a blade and a disk part and let $\mathcal{R}_j = (O, \mathbf{e}_1^j, \mathbf{e}_2^j, \mathbf{e}_3)$ be the local frame defined in Figure 2.2. Note this local frame rotates at a constant speed Ω around its rotational axis (O, \mathbf{e}_3) . We denote by n_m , n_p , and n_i , the dofs respectively located at the right

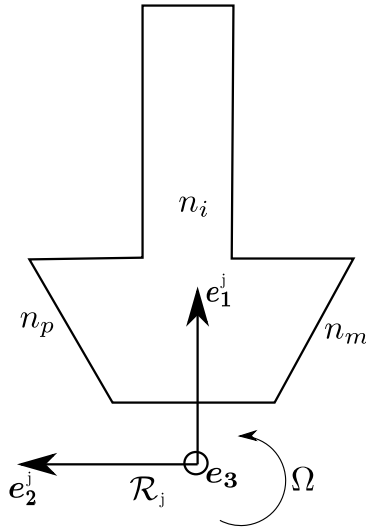


Figure 2.2 – Blade sector

boundary, left boundary (meaning the interface of two consecutive sectors) and internal domain. We then have $n_p = n_i$. It should be noted that the total number of dofs is $n = M(n_m + n_i)$. Furthermore, for a better readability, Ω will be omitted in the following.

Let $[E]$ be the matrix representing either $[M]$, $[D]$, $[K_e]$, $[K_g]$, or $[K_c]$. Let $[E^\alpha]$ be the matrix $[E]$ related to one sector α . The bloc writing of matrix $[E^\alpha]$ with

respect to the dofs (n_m, n_i, n_p) is

$$[E^\alpha] = \begin{bmatrix} [E_{mm}^\alpha] & [E_{mi}^\alpha] & [0] \\ [E_{mi}^\alpha]^T & [E_{ii}^\alpha] & [E_{ip}^\alpha] \\ [0] & [E_{ip}^\alpha]^T & [E_{pp}^\alpha] \end{bmatrix}. \quad (2.43)$$

Similarly, the bloc writing of the skew-symmetric finite element matrix $[C(\Omega)]$ is written as

$$[C^\alpha] = \begin{bmatrix} [C_{mm}^\alpha] & [C_{mi}^\alpha] & [0] \\ -[C_{mi}^\alpha]^T & [C_{ii}^\alpha] & [C_{ip}^\alpha] \\ [0] & -[C_{ip}^\alpha]^T & [C_{pp}^\alpha] \end{bmatrix}. \quad (2.44)$$

Note that the diagonal of matrix $[C^\alpha]$ is equal to zero since $[C^\alpha]$ is skew-symmetric. It is assumed that the detuned bladed-disk structure is constructed using only two sector types, denoted by A and B . Let $j \in \{0, \dots, M-1\}$ be a given sector of the detuned bladed-disk structure and let $\alpha_j \in \{1, 2\}$ be the its type. For instance, $\alpha_3 = 1$ means that sector number $j = 3$ is related to sector type A .

Let $\mathcal{P} = \{\alpha_0, \dots, \alpha_{M-1}\}$ be a given pattern defining a configuration of the detuned bladed-disk structure. For instance, pattern $\mathcal{P} = 12B6A3B3A$, is constituted of 12 consecutive blades of type B , 6 of type A , 3 of type B , and 3 of type A . The finite element matrix $[E]$ of the detuned bladed-disk is written as

$$[E] = \begin{bmatrix} [E_1^0] & [E_2^0] & [0] & \dots & [0] & [E_3^0] \\ [E_3^1] & [E_1^1] & [E_2^1] & \ddots & & [0] \\ [0] & \ddots & \ddots & \ddots & \ddots & \vdots \\ \vdots & \ddots & \ddots & \ddots & \ddots & [0] \\ [0] & \ddots & \ddots & \ddots & \ddots & [E_2^{M-2}] \\ [E_2^{M-1}] & [0] & \dots & [0] & [E_3^{M-1}] & [E_1^{M-1}] \end{bmatrix}. \quad (2.45)$$

where the block matrices $[E_1^j]$, $[E_2^j]$, $[E_3^j]$ of matrix $[E]$ are defined by

$$[E_1^j] = \begin{bmatrix} [E_{mm}^{\alpha_j}] + [P]^T [E_{pp}^{\alpha_j}] [P] & [E_{mi}^{\alpha_j}] \\ [E_{mi}^{\alpha_j}]^T & [E_{ii}^{\alpha_j}] \end{bmatrix}, [E_2^j] = \begin{bmatrix} [0] & [0] \\ [E_{ip}^{\alpha_j}] [P] & [0] \end{bmatrix}, [E_3^j] = [E_2^j]^T, \quad (2.46)$$

and where the $(n_m \times n_m)$ matrix $[P]$ is defined by:

$$[P] = \begin{bmatrix} [P_0] & [0] & \dots & [0] \\ [0] & \ddots & \ddots & \vdots \\ \vdots & \ddots & \ddots & [0] \\ [0] & \dots & [0] & [P_0] \end{bmatrix}. \quad (2.47)$$

with $[P_0]$ the (3×3) rotation matrix of angle $\theta_0 = \frac{2\pi}{M}$ such that

$$[P_0] = \begin{bmatrix} \cos(\theta_0) & -\sin(\theta_0) & 0 \\ \sin(\theta_0) & \cos(\theta_0) & 0 \\ 0 & 0 & 1 \end{bmatrix}. \quad (2.48)$$

Considering the gyroscopic coupling term, we similarly define from Equation (2.44) the block matrices $[C_1^j]$, $[C_2^j]$, and $[C_3^j]$ are written as

$$[C_1^{\alpha_j}] = \begin{bmatrix} [C_{mm}^{\alpha_j}] + [P]^T [C_{pp}^{\alpha_j}] [P] & [C_{mi}^{\alpha_j}] \\ -[C_{mi}^{\alpha_j}]^T & [C_{ii}^{\alpha_j}] \end{bmatrix}, \quad [C_2^{\alpha_j}] = \begin{bmatrix} [0] & [0] \\ [C_{ip}^{\alpha_j}] [P] & [0] \end{bmatrix}, \quad [C_3^{\alpha_j}] = -[C_2^{\alpha_j}]^T. \quad (2.49)$$

2.4.3 Particular case of the tuned bladed-disk structure

In this Section, we consider the particular case for which the pattern is such that $\mathcal{P} = 24A$ or $\mathcal{P} = 24B$ which correspond to tuned cases, that is to say, two bladed-disk structures that have cyclic symmetry. In this case, we have the following properties

$$[E_1^0] = [E_1^1] = \dots = [E_1^{M-1}] \quad \text{denoted by} \quad [E_1] \quad (2.50)$$

$$[E_2^0] = [E_2^1] = \dots = [E_2^{M-1}] \quad \text{denoted by} \quad [E_2] \quad (2.51)$$

$$[E_3^0] = [E_3^1] = \dots = [E_3^{M-1}] \quad \text{denoted by} \quad [E_3]. \quad (2.52)$$

Consequently, the finite element matrix $[E]$ is a block-circulant matrix, that is written as

$$[E] = \begin{bmatrix} [E_1] & [E_2] & [0] & \dots & [0] & [E_3] \\ [E_3] & [E_1] & [E_2] & \ddots & & [0] \\ [0] & \ddots & \ddots & \ddots & \ddots & \vdots \\ \vdots & \ddots & \ddots & \ddots & \ddots & [0] \\ [0] & \ddots & \ddots & \ddots & \ddots & [E_2] \\ [E_2] & [0] & \dots & [0] & [E_3] & [E_1] \end{bmatrix}. \quad (2.53)$$

where the block matrices $[E_1^j]$, $[E_2^j]$, and $[E_3^j]$ of the matrix $[E]$ are similarly expressed as those in Equation (2.46). It should be noted that the gyroscopic coupling matrix $[C]$ has also the same block circulant property.

Chapter 3

Construction of the nominal (or mean) nonlinear reduced-order model

Contents

3.1	Introduction	25
3.2	First NonLinear Reduced-Order Model (NL-ROMF) for a detuned bladed-disk	27
3.3	Second nonlinear reduced-order model (NL-ROM) for a detuned bladed-disk	28

3.1 Introduction

As explained in Chapter 2, the computational model is constructed by using the finite element method is referred as the NonLinear High-Fidelity computational Model (NL-HFM), which cannot be solved because the number of degrees-of-freedom is too large for analyzing such nonlinear dynamic system. Consequently, it is necessary to introduce an appropriate **NonLinear Reduced-Order Model (NL-ROM)** that allows for reducing the number of unknowns.

The objective of this Section is to construct the NL-ROM for a rotating detuned bladed-disk structure. Such a construction requires the use of a vector basis for projecting the nonlinear computational model. As explained in Chapter 1, many methods can be used for constructing such a vector basis. In this work, the methodology proposed is the one summarized in Section 1.3 and detailed below.

The first step consists in computing the eigenmodes of the generalized eigenvalue problem defined by mass matrix $[M]$ and matrix $[K_1(\Omega)]$ for rotation speed Ω fixed, associated with the linear high fidelity model (L-HFM). Note that damping matrix $[D]$ and gyroscopic coupling matrix $[C(\Omega)]$ are not included in the generalized eigenvalue problem in order to obtain real eigenvalues and real eigenvectors and not complex eigenvalues and complex eigenvectors, which would induce great difficulties for very large computational models (case for the considered rotating bladed-disk structure). Removing the damping matrix in such formulation is usual for small damping, which is the case. The gyroscopic coupling matrix plays a important role. This matrix will obviously be kept for constructing the nonlinear reduced-order model NL-ROMF, using this vector basis. It should also be noted that this constructed vector basis is not an optimal one with respect to the convergence speed of the NL-ROM, since this vector basis ignores the nonlinear geometrical effects and the gyroscopic coupling terms (the damping matrix $[D]$ does not influence the convergence speed because damping is very small). The projection of the NL-HFM on this basis yields an intermediate nonlinear reduced-order model, denoted as NL-ROMF, which takes into account all the physical phenomena modeled in the NL-HFM. The convergence of the dynamical response of this NL-ROMF towards the nonlinear dynamical response of the NL-HFM (rotating detuned bladed-disk structure) will carefully be studied. Indeed, the nonlinear dynamic response generated by this NL-ROMF must be equivalent to the one generated by the NL-HFM. The converged nonlinear solution of the NL-ROMF, which is computed in the time domain, is then used to calculate a second vector basis using the Proper Orthogonal Decomposition method (POD-method). By combining these two vector bases, the NL-ROM is constructed and has a dimension that is lower than the dimension of the NL-ROMF .

Consequently, with this NL-ROM, (1) the damping effects and all the rotating effects are taken into account, (2) for the rotating detuned bladed-disk structure, the NL-ROM is of lower order, which is more efficient than the NL-ROMF in terms of computational costs in the framework of implementing uncertainties, (3) the probabilistic model describing the mistuning can then be implemented in the NL-ROM, in order to obtain the nonlinear stochastic reduced-order model (NL-SROM) with a decreasing of the computational costs involved by the use of the Monte Carlo numerical method.

3.2 First NonLinear Reduced-Order Model (NL-ROMF) for a detuned bladed-disk structure

As explained in Section 3.1, the first nonlinear reduced-order model (NL-ROMF) requires the computation of the vector basis obtained by solving the following generalized eigenvalue problem,

$$[K_1(\Omega)] \bar{\varphi}_\alpha = \bar{\lambda}_\alpha [M] \bar{\varphi}_\alpha, \quad (3.1)$$

in which, for $\alpha = \{1, \dots, m\}$ with $m \ll n$, the eigenvalues $\bar{\lambda}_\alpha = (2\pi\bar{\nu}_\alpha)^2$ are sorted such that $0 < \bar{\lambda}_1 \leq \bar{\lambda}_2 \leq \dots \leq \bar{\lambda}_m$, and where the corresponding elastic modes $\bar{\varphi}_1, \dots, \bar{\varphi}_m$ are stored in the $(n \times m)$ real modal matrix $[\bar{\Phi}^m]$, with the following orthogonality properties

$$[\bar{\Phi}^m]^T [M] [\bar{\Phi}^m] = [I_m] \quad (3.2)$$

$$[\bar{\Phi}^m]^T [K_1(\Omega)] [\bar{\Phi}^m] = [\Lambda_m], \quad (3.3)$$

in which $[I_m]$ is the identity matrix of dimension m and where $[\Lambda_m]$ is the diagonal matrix containing the eigenvalues λ_α . The NL-ROMF is thus obtained by projecting Eq. (2.40) on the subspace spanned by $[\bar{\Phi}^m]$,

$$\mathbf{u}(t) = [\bar{\Phi}^m] \bar{\mathbf{q}}(t), \quad (3.4)$$

$$[\bar{\mathcal{M}}] \ddot{\bar{\mathbf{q}}}(t) + ([\bar{\mathcal{D}}] + [\bar{\mathcal{C}}(\Omega)]) \dot{\bar{\mathbf{q}}}(t) + [\bar{\mathcal{K}}_1(\Omega)] \bar{\mathbf{q}}(t) + \bar{\mathcal{F}}^{\text{NL}}(\bar{\mathbf{q}}(t)) = \bar{\mathcal{F}}(t), \quad (3.5)$$

in which $\bar{\mathbf{q}}(t)$ is the \mathbb{R}^m -vector of the generalized coordinates, and where $[\bar{\mathcal{M}}]$, $[\bar{\mathcal{D}}]$, $[\bar{\mathcal{C}}(\Omega)]$, and $[\bar{\mathcal{K}}_1(\Omega)]$ are the $(m \times m)$ reduced mass, damping, gyroscopic, and stiffness matrices. Note that matrices $[\bar{\mathcal{M}}]$ and $[\bar{\mathcal{K}}_1(\Omega)]$ are diagonal positive-definite matrices, matrix $[\bar{\mathcal{D}}]$ is a full positive-definite matrix in the general case (and will presently be a diagonal positive-definite matrix due to the use of a damping Rayleigh model), and $[\bar{\mathcal{C}}(\Omega)]$ is a full skew-symmetric matrix. In Eq. (3.5), the \mathbb{R}^m -vectors $\bar{\mathcal{F}}(t)$ and $\bar{\mathcal{F}}^{\text{NL}}(\bar{\mathbf{q}}(t))$ are the vectors of the reduced external forces and of the nonlinear reduced internal forces defined by

$$\bar{\mathcal{F}}(t) = [\bar{\Phi}^m]^T \mathbf{f}(t), \quad (3.6)$$

$$\bar{\mathcal{F}}^{\text{NL}}(\bar{\mathbf{q}}(t)) = [\bar{\Phi}^m]^T \mathbf{f}^{\text{NL}}([\bar{\Phi}^m] \bar{\mathbf{q}}(t)). \quad (3.7)$$

Remark about the nonlinear reduced internal forces

In Eq. (3.5), $\bar{\mathcal{F}}^{\text{NL}}(\bar{\mathbf{q}}(t))$ are the reduced nonlinear internal forces written [91, 89] as,

$$\bar{\mathcal{F}}^{\text{NL}}(\bar{\mathbf{q}}(t)) = \bar{\mathcal{K}}_{\alpha\beta\gamma}^{(2)} \bar{q}_\beta \bar{q}_\gamma + \bar{\mathcal{K}}_{\alpha\beta\gamma\delta}^{(3)} \bar{q}_\beta \bar{q}_\gamma \bar{q}_\delta, \quad (3.8)$$

where the quadratic and cubic reduced stiffnesses $\overline{\mathcal{K}}_{\alpha\beta\gamma}^{(2)}$ and $\overline{\mathcal{K}}_{\alpha\beta\gamma\delta}^{(3)}$ are such that

$$\overline{\mathcal{K}}_{\alpha\beta\gamma}^{(2)} = \frac{1}{2} \left(\overline{\mathcal{K}}_{\alpha\beta\gamma}^{(2)} + \overline{\mathcal{K}}_{\gamma\alpha\beta}^{(2)} + \overline{\mathcal{K}}_{\beta\gamma\alpha}^{(2)} \right) , \quad (3.9)$$

$$\overline{\mathcal{K}}_{\alpha\beta\gamma}^{(2)} = \int_{\mathcal{D}} \mathfrak{a}_{ijkl} \frac{\partial \overline{\varphi}_i^\alpha}{\partial x_j} \frac{\partial \overline{\varphi}_m^\beta}{\partial x_k} \frac{\partial \overline{\varphi}_m^\gamma}{\partial x_\ell} d\mathbf{x} , \quad (3.10)$$

$$\overline{\mathcal{K}}_{\alpha\beta\gamma\delta}^{(3)} = \frac{1}{2} \int_{\mathcal{D}} \mathfrak{a}_{ijkl} \frac{\partial \overline{\varphi}_s^\alpha}{\partial x_i} \frac{\partial \overline{\varphi}_s^\beta}{\partial x_j} \frac{\partial \overline{\varphi}_m^\gamma}{\partial x_k} \frac{\partial \overline{\varphi}_m^\delta}{\partial x_\ell} d\mathbf{x} . \quad (3.11)$$

Due to the properties of the elasticity tensor \mathfrak{a} , we have the following properties,

$$\overline{\mathcal{K}}_{\alpha\beta\gamma}^{(2)} = \overline{\mathcal{K}}_{\gamma\alpha\beta}^{(2)} = \overline{\mathcal{K}}_{\beta\gamma\alpha}^{(2)} , \quad (3.12)$$

$$\overline{\mathcal{K}}_{\alpha\beta\gamma}^{(2)} = \overline{\mathcal{K}}_{\alpha\gamma\beta}^{(2)} , \quad (3.13)$$

$$\overline{\mathcal{K}}_{\alpha\beta\gamma\delta}^{(3)} = \overline{\mathcal{K}}_{\beta\alpha\gamma\delta}^{(3)} = \overline{\mathcal{K}}_{\alpha\beta\delta\gamma}^{(3)} = \overline{\mathcal{K}}_{\gamma\delta\alpha\beta}^{(3)} . \quad (3.14)$$

It should be noted that the vector of the nonlinear reduced internal forces is constructed according to Eq. (3.7), by using an algebraic explicit calculation of the integrals (3.10) and (3.11), which are discretized by the finite element method. When the intensity of the external load is small, yielding negligible nonlinear geometric effects, the nonlinear reduced internal forces $\overline{\mathcal{F}}^{\text{NL}}(\overline{\mathbf{q}}(t))$ can be removed from Eq. (3.5), yielding the **Linear Reduced-Order Model (L-ROM)** that is written as

$$[\overline{\mathcal{M}}] \ddot{\overline{\mathbf{q}}}(t) + ([\overline{\mathcal{D}}] + [\overline{\mathcal{C}}(\Omega)]) \dot{\overline{\mathbf{q}}}(t) + [\overline{\mathcal{K}}_1(\Omega)] \overline{\mathbf{q}}(t) = \overline{\mathcal{F}}(t) . \quad (3.15)$$

3.3 Second nonlinear reduced-order model (NL--ROM) for a detuned bladed-disk structure

As explained in Section 3.1, the second step consists in using the POD-method applied to the NL-ROMF that includes all the effects (in particular, damping, gyroscopic coupling, and geometric nonlinearity). Eq. (3.5) is solved using the scheme proposed in [35]. The Newmark scheme [114] is used for which the time step Δt is constant. At each time step, the nonlinear algebraic equation is solved using the fixed point method. When the fixed point does not converge, it is replaced by the Crisfield arc-length method [115], depending on the local nonlinearity rate. Integration time step Δt is also used as the distance between two consecutive snapshots for the POD method, which is not penalizing because the dimension m

of the NL-ROMF is small ($m \ll n$). Let n_t be the number of time steps. Let $[A]$ be the $(m \times n_t)$ real matrix with $n_t > m$ defined by

$$[A]_{ij} = \bar{q}_i(t_j) \sqrt{\Delta t}. \quad (3.16)$$

Let $[C_A]$ be the $(m \times m)$ real matrix defined by

$$[C_A] = [A][A]^T, \quad (3.17)$$

whose rank is \bar{m} that is less than or equal to m (if $\bar{m} < m$, then $[C_A]$ is not positive definite but only positive). The vector basis is obtained by solving the eigenvalue problem

$$[C_A] \boldsymbol{\psi}_\alpha = \mu_\alpha \boldsymbol{\psi}_\alpha, \quad (3.18)$$

in which the vector basis is made up of the eigenvectors $\boldsymbol{\psi}_\alpha$ corresponding to the \bar{m} largest eigenvalues μ_α . In practice, matrix $[C_A]$ is not computed. Its eigenvalues and its eigenvectors are obtained by computing the singular value decomposition of matrix $[A]$ using an economy size algorithm [116]. Removing the zero singular values, this decomposition can be written as,

$$[A] = [W][S][V]^T, \quad (3.19)$$

in which $[W]$ is a unitary $(m \times \bar{m})$ real matrix ($[W]^T [W] = [I_{\bar{m}}]$), where $[V]$ is another unitary $(n_t \times \bar{m})$ real matrix ($[V]^T [V] = [I_{\bar{m}}]$), and where the diagonal $(\bar{m} \times \bar{m})$ real matrix $[S]$ contains all the \bar{m} non-zeros singular values sorted by decreasing order $s_1 \geq s_2 \geq \dots \geq s_{\bar{m}} > 0$. It can be shown that the singular values are the square-roots of the positive eigenvalues of matrix $[C_A]$, that is to say,

$$s_\alpha = \sqrt{\mu_\alpha}. \quad (3.20)$$

It can also be shown that the \bar{m} columns of matrix $[W]$ are the corresponding eigenvectors $\boldsymbol{\psi}_\alpha$ of matrix $[C_A]$.

Let $[\mathcal{W}^{(m,N)}]$ be the $(m \times N)$ matrix with $N \leq \bar{m} < m$ that contains the eigenvectors related to the N greatest singular values s_α , $\alpha = \{1, \dots, N\}$, which is such that $[\mathcal{W}^{(m,N)}]^T [\mathcal{W}^{(m,N)}] = [I_N]$. Finally, the projection basis, represented by the $(m \times N)$ real matrix $[\Phi^{(m,N)}]$ and that will be used for obtaining the NL-ROM, is such that

$$[\Phi^{(m,N)}] = [\bar{\Phi}^m] [\mathcal{W}^{(m,N)}], \quad (3.21)$$

in which the column number α of matrix $[\Phi^{(m,N)}]$ is denoted by $\boldsymbol{\varphi}_\alpha$. It should be noted that we have

$$[\Phi^{(m,N)}]^T [\Phi^{(m,N)}] = [I_N]. \quad (3.22)$$

The NL-ROM is then obtained by projecting the NL-HFM on the reduced-order basis $[\Phi^{(m,N)}]$ and is written as

$$\mathbf{u}(t) = [\Phi^{(m,N)}] \mathbf{q}(t), \quad (3.23)$$

$$[\mathcal{M}] \ddot{\mathbf{q}}(t) + ([\mathcal{D}] + [\mathcal{C}(\Omega)]) \dot{\mathbf{q}}(t) + [\mathcal{K}_1(\Omega)] \mathbf{q}(t) + \mathcal{F}^{\text{NL}}(\mathbf{q}(t)) = \mathcal{F}(t), \quad (3.24)$$

in which $\mathbf{q}(t)$ is the \mathbb{R}^N -vector of the generalized coordinates, and where $[\mathcal{M}]$, $[\mathcal{D}]$, $[\mathcal{C}(\Omega)]$, and $[\mathcal{K}_1(\Omega)]$ are the $(N \times N)$ mass, damping, gyroscopic coupling, and stiffness reduced matrices. Note that matrix $[\mathcal{M}] = [I_N]$, matrices $[\mathcal{D}]$, $[\mathcal{K}_1(\Omega)]$ are full positive definite matrices, and $[\mathcal{C}(\Omega)]$ is a full skew-symmetric matrix. It should be noted that matrix $[\mathcal{K}_1(\Omega)]$ can be decomposed according to its elastic, centrifugal, and geometric stiffness parts such that

$$[\mathcal{K}_1(\Omega)] = [\mathcal{K}_e] + [\mathcal{K}_c(\Omega)] + [\mathcal{K}_g(\Omega)]. \quad (3.25)$$

In Eq. (3.24), the \mathbb{R}^N -vectors $\mathcal{F}(t)$ and $\mathcal{F}^{\text{NL}}(\mathbf{q}(t))$ are the vectors defined by

$$\mathcal{F}(t) = [\Phi^{m,N}]^T \mathbf{f}(t) \quad (3.26)$$

$$\mathcal{F}^{\text{NL}}(\mathbf{q}(t)) = [\Phi^{m,N}]^T \mathbf{f}^{\text{NL}}([\Phi^{m,N}] \mathbf{q}(t)). \quad (3.27)$$

Similarly to Eqs. (3.8) to (3.14), vector $\mathcal{F}^{\text{NL}}(\mathbf{q}(t))$ can be written as,

$$\mathcal{F}^{\text{NL}}(\mathbf{q}(t)) = \mathcal{K}_{\alpha\beta\gamma}^{(2)} q_\beta q_\gamma + \mathcal{K}_{\alpha\beta\gamma\delta}^{(3)} q_\beta q_\gamma q_\delta, \quad (3.28)$$

where the quadratic and cubic reduced stiffnesses $\mathcal{K}_{\alpha\beta\gamma}^{(2)}$ and $\mathcal{K}_{\alpha\beta\gamma\delta}^{(3)}$ are such that

$$\mathcal{K}_{\alpha\beta\gamma}^{(2)} = \frac{1}{2} \left(\widehat{\mathcal{K}}_{\alpha\beta\gamma}^{(2)} + \widehat{\mathcal{K}}_{\gamma\alpha\beta}^{(2)} + \widehat{\mathcal{K}}_{\beta\gamma\alpha}^{(2)} \right), \quad (3.29)$$

$$\widehat{\mathcal{K}}_{\alpha\beta\gamma}^{(2)} = \int_{\mathcal{D}} \mathfrak{O}_{ijkl} \frac{\partial \varphi_i^\alpha}{\partial x_j} \frac{\partial \varphi_m^\beta}{\partial x_k} \frac{\partial \varphi_m^\gamma}{\partial x_\ell} d\mathbf{x}, \quad (3.30)$$

$$\mathcal{K}_{\alpha\beta\gamma\delta}^{(3)} = \frac{1}{2} \int_{\mathcal{D}} \mathfrak{O}_{ijkl} \frac{\partial \varphi_s^\alpha}{\partial x_i} \frac{\partial \varphi_s^\beta}{\partial x_j} \frac{\partial \varphi_m^\gamma}{\partial x_k} \frac{\partial \varphi_m^\delta}{\partial x_\ell} d\mathbf{x}. \quad (3.31)$$

Due to the properties of the elasticity tensor \mathfrak{O} , we have the following properties:

$$\mathcal{K}_{\alpha\beta\gamma}^{(2)} = \mathcal{K}_{\gamma\alpha\beta}^{(2)} = \mathcal{K}_{\beta\gamma\alpha}^{(2)}, \quad (3.32)$$

$$\widehat{\mathcal{K}}_{\alpha\beta\gamma}^{(2)} = \widehat{\mathcal{K}}_{\alpha\gamma\beta}^{(2)}, \quad (3.33)$$

$$\mathcal{K}_{\alpha\beta\gamma\delta}^{(3)} = \mathcal{K}_{\beta\alpha\gamma\delta}^{(3)} = \mathcal{K}_{\alpha\beta\delta\gamma}^{(3)} = \mathcal{K}_{\gamma\delta\alpha\beta}^{(3)}. \quad (3.34)$$

Note that the separation of the quadratic and cubic stiffness contributions $\widehat{\mathcal{K}}_{\alpha\beta\gamma}^{(2)}$ and $\mathcal{K}_{\alpha\beta\gamma\delta}^{(3)}$ defined by Eqs. (3.30) and (3.31) is voluntarily kept in order to implement the nonparametric probabilistic approach for modeling mistuning (see Chapter 5).

Chapter 4

Nonlinear computational dynamics of a detuned bladed-disk structure

Contents

4.1	Introduction	32
4.2	Computational model for the tuned and for the detuned bladed-disk structure	32
4.2.1	Computational model of the tuned bladed-disk structure	32
4.2.2	Computational model of the detuned bladed-disk structure	35
4.3	Modal analysis of the rotating tuned bladed-disk structure and numerical validation	35
4.3.1	Modal analysis	35
4.3.2	Numerical validation	36
4.4	Nonlinear deterministic analysis	37
4.4.1	Definition of the external load (excitation)	37
4.4.2	Definition of the observations	41
4.4.3	Numerical aspects	44
4.4.4	Convergence analysis with respect to the dimension of the NL-ROM	44
4.4.5	Sensitivity analysis of the deterministic responses for the nonlinear tuned rotating bladed-disk with respect to amplitude s_0 of the excitation	46
4.4.6	Linear and nonlinear dynamic analyses in the time domain using the L-ROM and NL-ROM	48

4.4.7 Analysis of the nonlinear dynamic time responses in the
 frequency domain 49

4.1 Introduction

In this chapter we define the computational model of a tuned and of a detuned bladed-disk structure constituted of $M = 24$ blades, which are used for performing the numerical simulations. This chapter is mainly devoted to the analysis of the effects of geometric nonlinearities on the nonlinear dynamic behavior of these two structures (tuned and detuned) without mistuning. In this framework, an ensemble of novel results is presented.

4.2 Computational model for the tuned and for the detuned bladed-disk structure

In this section we first present the computational model of the tuned bladed-disk structure, and then the computational model for the detuned one.

4.2.1 Computational model of the tuned bladed-disk structure

The finite element meshes of the 24-blades tuned bladed-disk structure and of its corresponding reference sector are shown in Figure 4.1. The bladed-disk rotates around its cyclic axis with a constant rotation speed $\Omega = 2\pi \times 74 \text{ rad/s}$ (4440 RPM (Rotation Per Minute)). The material is steel, which is considered as a homogeneous and isotropic elastic material with Young modulus $2 \times 10^{11} \text{ N} \times \text{m}^{-2}$, Poisson's ratio 0.3, and mass density $7650 \text{ Kg} \times \text{m}^{-3}$. In the rotating frame, the disk is clamped at the inner radius of the disk (as previously shown in Figure 2.1). The main geometric characteristics of the bladed-disk are summarized in Table 4.1.

The finite element model of the reference sector has been carried out using tridimensional isoparametric solid finite elements with quadratic interpolation functions, in order to obtain a sufficient precision. The finite element mesh of the full bladed-disk is made of 37 488 HEXahedral finite elements with 20 nodes (HEX20), 1 848 PYRamidal finite elements with 13 (PYR13) nodes, and 45 864 TETrahedral finite elements with 10 nodes (TET10). The numerical description of the finite element model is given in Table 4.2. For the linear tuned rotating bladed-

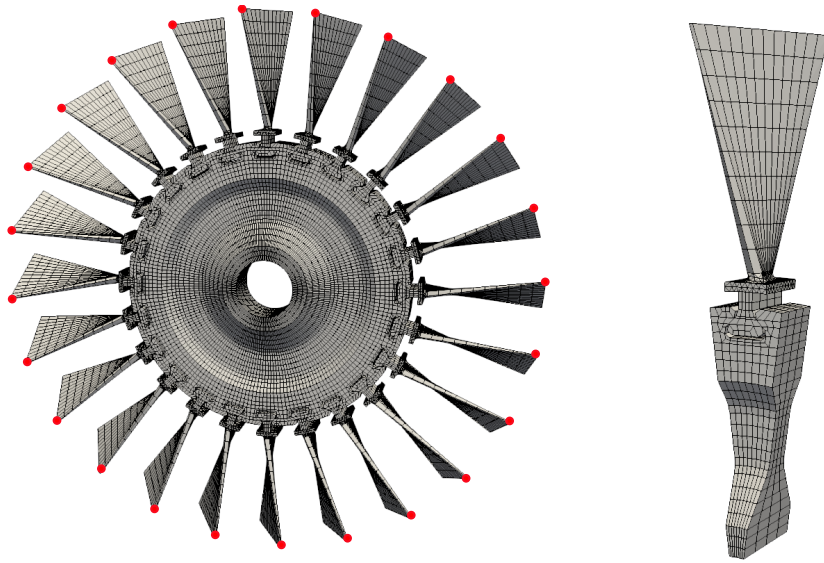


Figure 4.1 – Finite element model of the bladed-disk with 24 blades in which the dot symbols (red color) correspond to the excitation points (left figure). Zoom of the finite element model of a sector (right figure).

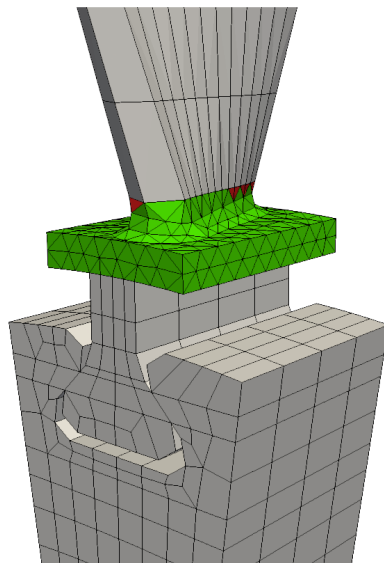


Figure 4.2 – Zoom of the finite element sector: grey, red and green finite elements are respectively related to hexahedral, pyramidal, and tetrahedral finite elements

disk structure, the eigenfrequency of the elastic mode that corresponds to the first bending mode of the blade with a circumferential wave number $h = 4$ is $\nu_1 = 435 Hz$ (see Figure 4.5). Following the Rayleigh damping model defined

Inner disk radius	19.8×10^{-3} m
Outer disk radius	100×10^{-3} m
Disk thickness	20×10^{-3} m
Blade thickness at root section	4.8×10^{-3} m
Blade thickness at tip section	2×10^{-3} m
Blade length from the root section	79×10^{-3} m

Table 4.1 – Geometric characteristics of the bladed-disk structure

Structure	Elements	Nodes	DOFs
Blade alone	2 714	6 896	20 688
Disk sector	836	4 554	13 662
Full structure	85 200	265 080	787 176

Table 4.2 – Element, nodes, and dofs of the finite element model

by Eq. (2.29), the coefficients α and β are chosen to obtain a critical damping rate that is equal to 10^{-2} for the frequency ν_1 . A general house-code written in MATLAB has been developed. This house-code has been validated in comparing its results with the commercial ANSYS code concerning the computation of the eigenfrequencies and the eigenmodes. Concerning the hexahedral finite elements, for which hourglass phenomenon can occur [40], ANSYS software uses a proper integration scheme for constructing the stiffness matrix. Table 4.3 summarizes the number of integration points used by ANSYS. The details concerning the choice of the interpolation functions and the position of the integration points are given in Appendix C, that are taken from ANSYS manual [117] and ASTER manual [118]. These values have been used in the house-code, developed in MATLAB. In the following we will precise the element types and their integration point that will be used in the presented calculations.

Matrices	Element type	Integration points
Elastic and geometric stiffness matrices	HEX20	14
	PYR13	2x2x2
	TET10	4
Mass matrix	HEX20	3x3x3
	PYR13	2x2x2
	TET10	4

Table 4.3 – Numerical integration points used by ANSYS commercial finite element software

4.2.2 Computational model of the detuned bladed-disk structure

The computational model of the detuned bladed-disk structure is constructed from the knowledge of two compatible meshes corresponding to the two different sector types that we have denoted as A and B . The reference sector B is obtained from sector A by decreasing the Young modulus of the blade by 10 %, the Young modulus of the disk remaining unchanged. Figure 4.3 shows a representation of the tuned structure $\mathcal{P}_0 = 24A$ and of one configuration of a detuned bladed-disk structure $\mathcal{P}_{31} = (6A6B)_2$. In the present research we consider 45 detuned bladed-

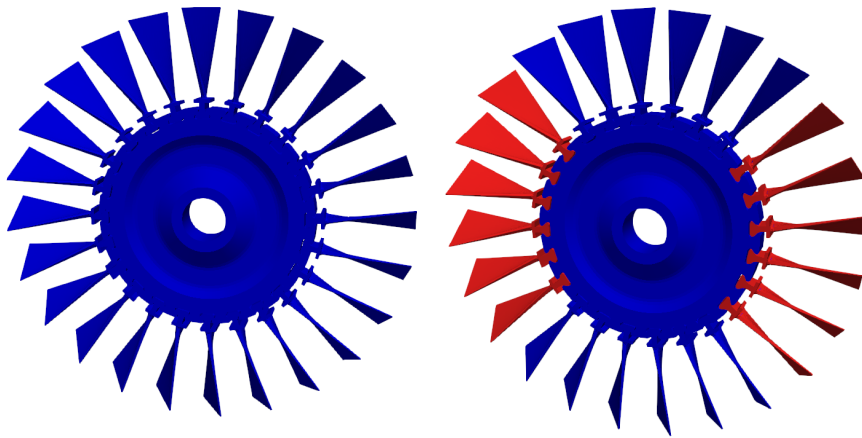


Figure 4.3 – Tuned bladed-disk structure $\mathcal{P}_0 = 24A$ (left figure) and detuned bladed-disk configuration $\mathcal{P}_{31} = (6A6B)_2$ with red blade for B and blue blade for A (right figure).

disk patterns, whose definition are given in Appendix B.

4.3 Modal analysis of the rotating tuned bladed-disk structure and numerical validation

4.3.1 Modal analysis

We consider the tuned rotating bladed-disk corresponding to pattern \mathcal{P}_0 , for which the generalized eigenvalue problem defined by Eq. (3.1) is solved. It should be noted that the cyclic symmetry properties of the structure is not used. Figure 4.4

displays the Campbell diagram representing the evolution of the eigenfrequencies ν_α of the linear tuned rotating bladed-disk \mathcal{P}_0 according to rotation speed Ω . The dashed lines represent the *EO*-engine order characterized by function $\Omega \mapsto EO \times \frac{\Omega}{60}$. A required condition for that an Engine Order (EO) excite a bladed-disk is that the EO frequency coincides with an eigenfrequency of the bladed-disk. The intersection of the eigenfrequencies with the dashed lines gives then an indication of the rotating speed yielding resonant situations of interest. The EO that allows to excite a circumferential wave number h corresponding to the number of nodal diameters of the considered mode is given by

$$j M \pm h = k \times EO, \quad (4.1)$$

in which j and k are integers. Figure 4.5 displays the graph of $\nu_\alpha(h)$ as a function of h for which rotation speed is 4 440 RPM. For this rotation speed, we are interested in the first 3 modes related to $h = 4$, which correspond to the first bending mode of the blades (mode 1 at 484 Hz), the second bending mode of the blades (mode 2 at 1 170 Hz), and the first torsional mode of the blades (mode 3 at 1 490 Hz). Figures 4.6 and 4.7 display a representation of the first four eigenmodes of the rotating structure. This modal analysis allows for validating the house-code with respect to the results obtained with the engineering software ANSYS (see Section 4.3.2) and useful for defining the external applied load that will be used in the numerical simulations presented in Section 4.4.

4.3.2 Numerical validation

In this Section, we present the numerical validation of the modal analysis. Let $\nu_\alpha^{\text{Ansys}}$ and ν_α be the eigenfrequencies computed with ANSYS and with the house-code. Let $\alpha \mapsto Err(\alpha)$ be the function that quantifies the relative error, defined by

$$Err(\alpha) = 100 \left| \left(1 - \frac{\nu_\alpha}{\nu_\alpha^{\text{Ansys}}} \right) \right| \quad \text{in } \% . \quad (4.2)$$

Figure 4.8 shows the graph $\alpha \mapsto Err(\alpha)$ for $\Omega = 0 \text{ rad.s}^{-1}$ (red line) and $\Omega = 1\,000 \text{ rad.s}^{-1}$ (blue line). A good agreement is obtained that validates the computational developments with the house-code. It can be observed that there is a small peak around the 30th eigenfrequency for a rotational speed of 1 000 rad/s with a maximum relative error level below 0.25%. This small error can be explained by the fact that we do not have all information about integration points used by ANSYS concerning the PYR13 finite element. Indeed, ANSYS uses 8

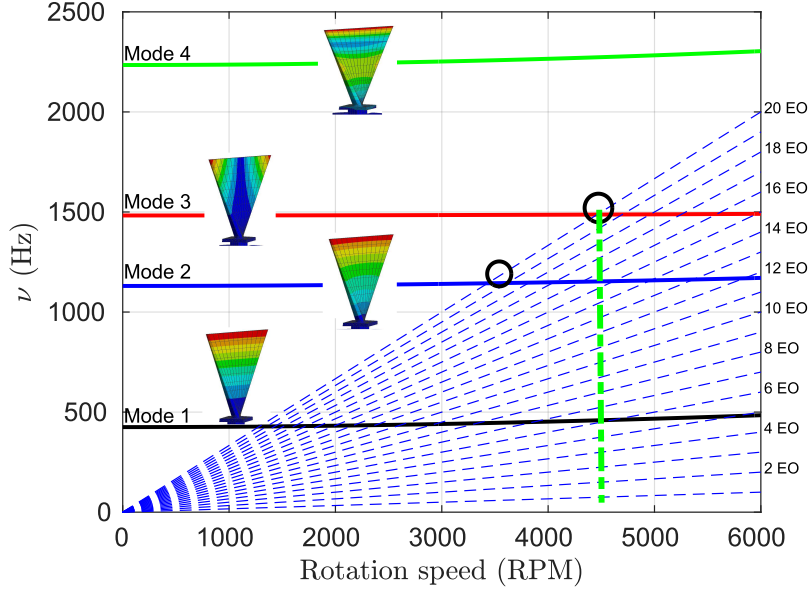


Figure 4.4 – Graph of $\Omega \mapsto \nu_\alpha(\Omega)$ defining the Campbell diagram of the eigenfrequencies (in Hz) of the linear tuned rotating bladed-disk structure (pattern \mathcal{P}_0) as a function of the rotation speed (in RPM), where EO denotes the engine order, and where the vertical dashed line identifies the speed of rotation that is considered.

integration points, which are not defined in the user guide. In the house code, we have chosen the 6 integration points defined in the ASTER user guide [118].

4.4 Nonlinear deterministic analysis of the tuned and the detuned rotating bladed-disk without mistuning

In this section, a nonlinear deterministic analysis of the tuned structure and of several configurations of detuned structures is considered using the NL-ROMF and the NL-ROM. The numerical results are compared with the corresponding linear responses obtained with the L-ROM.

4.4.1 Definition of the external load (excitation)

The objective of the presented analysis is not to compute the nonlinear dynamical response for a general physical excitation, but is to present a sensitivity study for

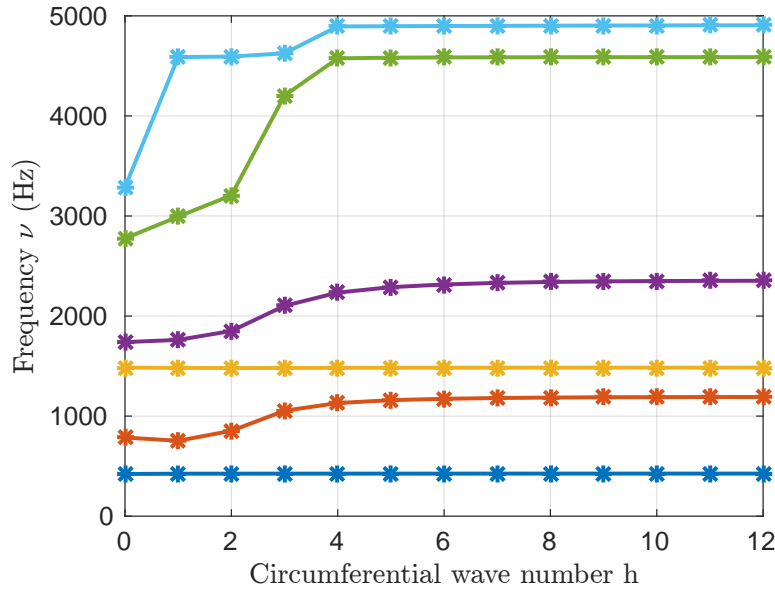


Figure 4.5 – Graph of $h \mapsto \nu_\alpha(h)$ of the eigenfrequencies ν_α of the linear tuned rotating bladed-disk structure (pattern \mathcal{P}_0) for rotation speed $\Omega = 4440$ RPM as a function of the circumferential wave number h .

understanding the role played by the geometrical nonlinear effects with respect to the linear counterpart. In this framework, the chosen spatial excitation will not correspond to a travelling wave in the rotating frame but to a standing wave. It should be noted that such a choice is coherent with the fact that no aerodynamic coupling is taken into account. Inspired by the type of analyses performed for the linear mistuned cases, the external forces have been chosen in order to control the circumferential wave number and also the frequency band of excitation, which has to be sufficiently narrow around the specified frequency of interest. This type of excitation allows for clearly analyzing the transfer of energy outside the excitation frequency band (which is the objective of the work). According to the Campbell diagram displayed in Figure 4.4, it can be seen that the third mode intersect the EO line corresponding to $EO = 20$ for the considered rotating speed $\Omega = 4440$ RPM. As a consequence, the excitation is chosen with a circumferential wave number $h = 4$ (nodal diameter), for which Eq. (4.1) is satisfied with $j = k = 1$. According to the Campbell diagram displayed in Figure 4.4, a 20-engine order is chosen corresponding to circumferential wave number $h = 4$ (nodal diameter). The excitation frequency band is chosen as $\mathbb{B}_e = [1\,000, 1\,600] \text{ Hz}$, in which $\nu_{\min} = 1\,000 \text{ Hz}$ and $\nu_{\max} = 1\,600 \text{ Hz}$. It contains the eigenfrequencies of the rotating

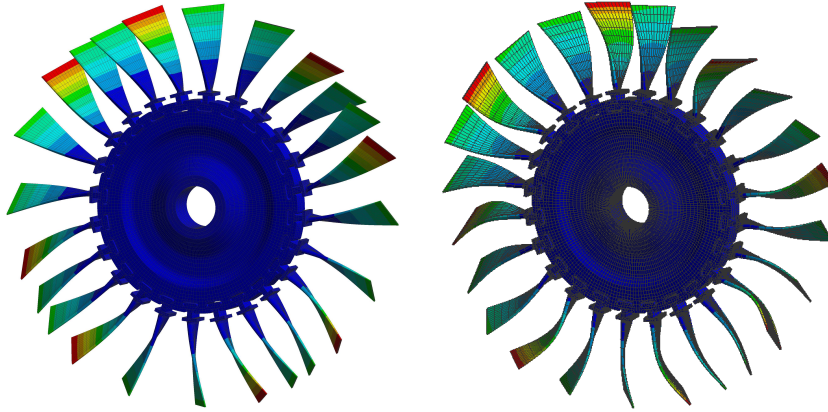


Figure 4.6 – Representation of the mode shapes of the tuned rotating bladed-disk structure for circumferential wave number $h = 4$. First bending mode related to eigenfrequency $\nu_1 = 484 Hz$ (left figure) and second bending mode related to eigenfrequency $\nu_2 = 1170 Hz$ (right figure)

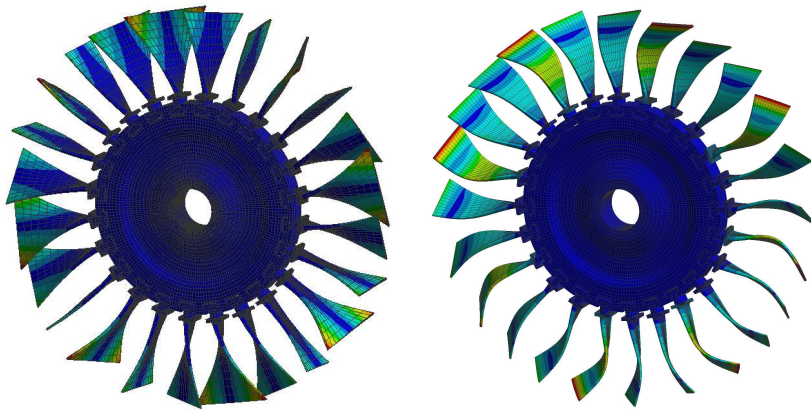


Figure 4.7 – Representation of the mode shapes of the tuned rotating bladed-disk structure for circumferential wave number $h = 4$. First torsional mode related to eigenfrequency $\nu_3 = 1490 Hz$ (left figure) and third bending mode related to eigenfrequency $\nu_4 = 2234 Hz$ (right figure)

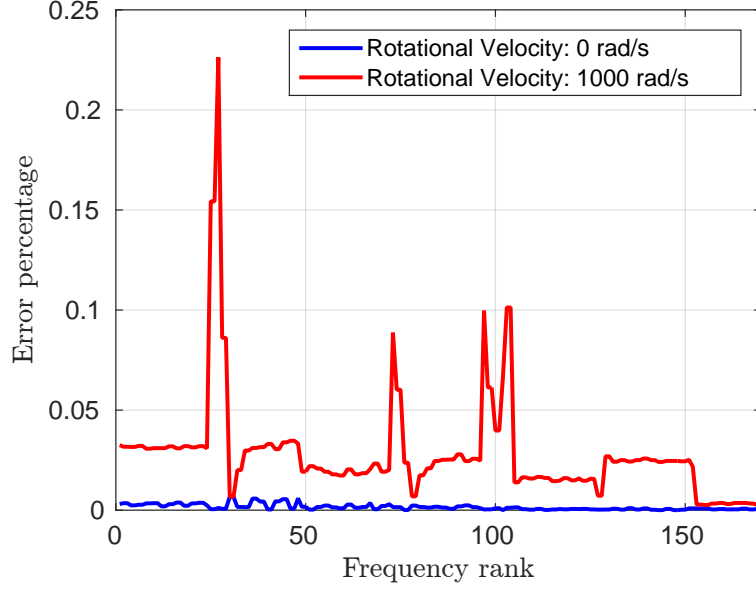


Figure 4.8 – Graph of function $\alpha \mapsto Err(\alpha)$ corresponding to the case $\Omega = 0 \text{ rad.s}^{-1}$ (blue line) and to the case $\Omega = 1000 \text{ rad.s}^{-1}$ (red line)

tuned bladed-disk structure related to the second bending mode (displayed in Figure 4.6) and the first torsional mode (displayed in Figure 4.7). In the time domain, the external force vector $\mathbf{f}(t)$ is defined by,

$$\mathbf{f}(t) = s_0 g(t) \mathbf{f}^s, \quad (4.3)$$

in which \mathbf{f}^s is the \mathbb{R}^n -vector representing the normalized spatial distribution of the external forces. In the present case, the excitation is located at the tip of each blade (see the red dot symbols in Figures 4.1) according to all the possible direction and with a constant phase-angle $\frac{2\pi h}{M} = \frac{\pi}{3}$, corresponding to a circumferential $h = 4$. In Eq. (4.3), the dimensionless time-function $t \mapsto g(t)$ is defined on \mathbb{R} and is such that the modulus $|\widehat{g}(2\pi\nu)|$ of its Fourier transform $\widehat{g}(2\pi\nu)$ is equal to 1 in frequency band \mathbb{B}_e and equal to zero outside \mathbb{B}_e . In this case, the time-dependant function $g(t)$ is written as

$$g(t) = 2 \frac{\sin(\pi \Delta\nu t)}{\pi t} \cos(2\pi s \Delta\nu t), \quad (4.4)$$

in which parameters $\Delta\nu$ and s are such that

$$\Delta\nu = \nu_{max} - \nu_{min}, \quad s = \frac{\nu_{max} + \nu_{min}}{2\Delta\nu}. \quad (4.5)$$

The load intensity of the force is controlled by scalar parameter s_0 . From a numerical point of view, function $g(t)$ is truncated by choosing $t_{ini} = -0.065 \text{ s}$ such

that $g(t_{ini}) = 0$ with a time duration $T = 0.18$ s. The calculations are carried out with $n_t = 4096$ time steps, using a sampling frequency $\nu_e = 16000$ Hz. These numerical parameters allow for considering the frequency band of analysis $\mathbb{B}_a = [0, 4000]$ Hz. With such parameters corresponding to a constant sample frequency step $\delta\nu = 3.9$ Hz and a constant time step $\delta t = 6.25 \times 10^{-5}$ s, it can be seen that, for $h = 4$, the first eigenfrequency of the rotating tuned bladed-disk structure could possibly be excited and in such case would correctly be represented with these parameters. Furthermore, such choice also ensures the dynamic system to return to its equilibrium state within a good relative tolerance. Figures 4.9 and 4.10 show the graphs of function $t \mapsto g(t)$ and the modulus of its Fourier transform $\nu \mapsto |\widehat{g}(2\pi\nu)|$. It should be noted that, from a computational point of view, the numerical values of $|\widehat{g}(2\pi\nu)|$ for ν in $\mathbb{B}_a \setminus \mathbb{B}_e$ are not exactly zero but differ with three orders of magnitude lower, which means that the linear dynamic response will have negligible magnitude in the band $\mathbb{B}_a \setminus \mathbb{B}_e$ (that will not be the case for the nonlinear dynamic response). The nonlinear dynamic analysis is then performed in the time domain according to Eqs. (3.23) and (3.24). A Fourier transform of the forced response obtained in the time domain is carried out and allows for analyzing, *a posteriori*, the nonlinear dynamic responses in the frequency domain. The numerical parameters have been carefully using the tuned configuration \mathcal{P}_0 and are used for any detuned configuration of the bladed-disk structure.

4.4.2 Definition of the observations

In this Chapter, we are interested in analyzing the nonlinear dynamic behavior of rotating tuned and detuned bladed-disk structures. Such analysis is performed by following the procedure described in Chapter 3 for constructing the NL-ROM. The nonlinear dynamic response $\mathbf{u}(t)$ is computed in the time domain according to Eqs. (3.23) and (3.24). The Fourier Transform of the nonlinear solution $\mathbf{u}(t)$ allows for computing the nonlinear dynamic response $\widehat{\mathbf{u}}(2\pi\nu)$ in the frequency domain. The nonlinear observation of interest are defined from $\widehat{\mathbf{u}}(2\pi\nu)$ as described hereinafter.

The observations of the nonlinear dynamic system have to be defined for performing the robust analysis of the rotating tuned and the detuned bladed-disk with or without mistuning. It is recalled that, in presence of mistuning, the responses are random. There are several possibilities for defining the observations. We have chosen one, which is coherent with all the analyses that are performed in the frequency domain. First, we define only one observation point in each blade that is located at its tip shown as red dot symbol in Figure 4.1. This means that, the

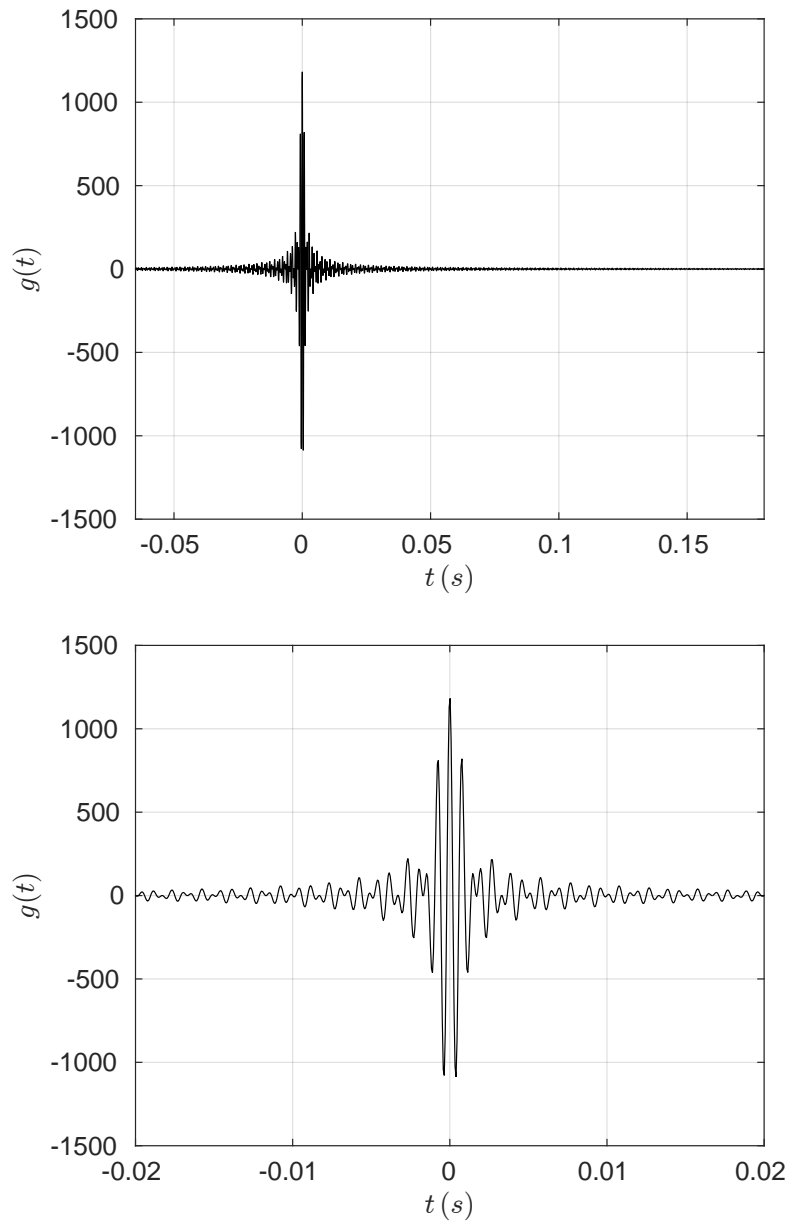


Figure 4.9 – Definition of the excitation: graph of the time-function excitation, $t \mapsto g(t)$, defines on interval $[-0.065, 0.18]$ s (top figure) and zoom on $[-0.02, 0.02]$ s interval (down figure).

number of observation points is equal to the number M of blades. For the rotating detuned bladed-disk structure without mistuning, we will look for the blade number j_0 where the maximum related to the amplitude of the displacement occurs,

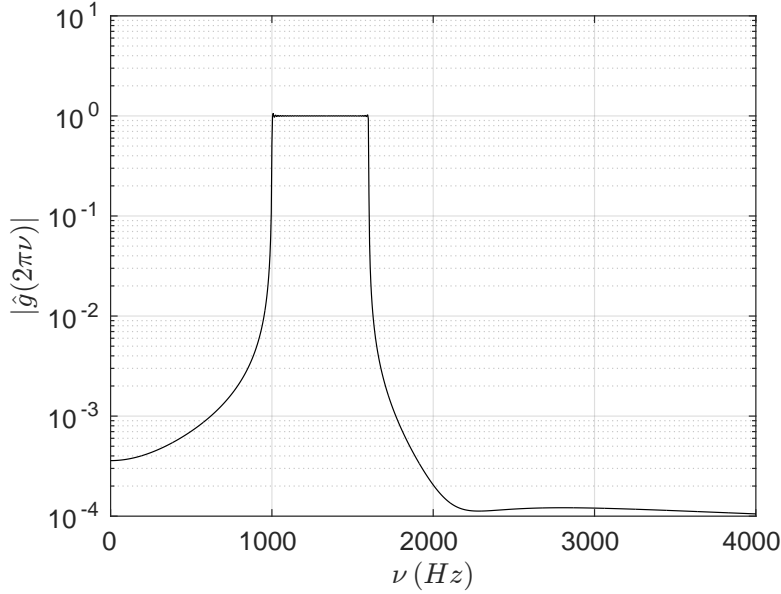


Figure 4.10 – Graph of function $\nu \mapsto |\hat{g}(2\pi\nu)|$ in log scale.

over all the blades and for the entire frequency band of analysis. It should be noted that, in presence of mistuning, j_0 becomes a random variable. Nevertheless, we want to characterize the random responses — of the rotating tuned and detuned bladed-disk structures in presence of mistuning — with respect to the deterministic response of its counterpart without mistuning. Consequently, we have chosen to keep j_0 as the deterministic blade number for the case for which mistuning is taken into account. The nonlinear analysis is carried out for the rotating tuned and detuned bladed-disk structures without mistuning. For each time t and for the observation in blade j , let $\mathbf{u}^j(t) = (u_1^j(t), u_2^j(t), u_3^j(t))$ be the vector whose coordinates are given in the local basis $(\mathbf{e}_1^j, \mathbf{e}_2^j, \mathbf{e}_3^j)$. For frequency ν in Hz, the Fourier Transform of function $t \mapsto \mathbf{u}^j(t)$ is written as $\hat{\mathbf{u}}^j(2\pi\nu) = (\hat{u}_1^j(2\pi\nu), \hat{u}_2^j(2\pi\nu), \hat{u}_3^j(2\pi\nu))$. We have to find the blade number j_0 such that

$$j_0 = \arg \max_{j=1, \dots, M} \|\hat{\mathbf{u}}^j\|, \quad (4.6)$$

in which $\|\hat{\mathbf{u}}^j\|$ is such that

$$\|\hat{\mathbf{u}}^j\| = \max_{\nu} \|\hat{\mathbf{u}}^j(2\pi\nu)\|, \quad (4.7)$$

with $\|\hat{\mathbf{u}}^j(2\pi\nu)\|^2 = \sum_{k=1}^3 |\hat{u}_k^j(2\pi\nu)|^2$. For the rotating tuned bladed-disk (therefore, it is not detuned and there is no mistuning), the quantity $\|\hat{\mathbf{u}}^j\|$ will be rewritten as

$|||\widehat{\mathbf{u}}^{j,\text{tuned}}|||$. It should be noted that, the blade number j_0 depends on the considered pattern and on the type of analysis, which is performed for the rotating detuned bladed-disk. There are two types of analysis, the linear one denoted by subscript L and the nonlinear one denoted by subscript NL. These subscripts will be omitted when no confusion will be possible.

We are thus interested in characterizing the amplification levels for the nonlinear deterministic case. We then define the quantity $b(2\pi\nu)$ as the deterministic amplification factor such that

$$b(2\pi\nu) = \frac{||\widehat{\mathbf{u}}^{j_0}(2\pi\nu)||}{|||\widehat{\mathbf{u}}^{j_0,\text{tuned}}|||} . \quad (4.8)$$

4.4.3 Numerical aspects

The dynamic response of the L-ROM defined by Eq. (3.15) is solved using the Newmark method [119] with the averaging acceleration scheme, which is an implicit and unconditionally stable integration scheme. The NL-ROMF and the NL-ROM defined by Eqs. (3.4)-(3.5) and (3.23)-(3.24) are also solved using the Newmark method. As explained in Chapter 3, for each time step, the nonlinear algebraic equation is solved using the fixed point method. In case of a non-convergence, the Crisfield arc-length algorithm [43, 120] is used.

4.4.4 Convergence analysis with respect to the dimension of the NL-ROM

In this section, the convergence analysis of the deterministic response of the NL-ROM, with respect to its dimension m , is considered for a given pattern of the rotating detuned bladed-disk (without mistuning). We estimate the optimal values of parameters m and N related to the truncation of the vector bases used for constructing the NL-ROM (according to Sections 3.2 and 3.3). Let $\widehat{w}(2\pi\nu)$ be the scalar value such that

$$\widehat{w}(2\pi\nu) = \sqrt{\sum_{j=1}^M ||\widehat{\mathbf{u}}^j(2\pi\nu)||^2} . \quad (4.9)$$

When dealing with the first projection basis represented by matrix $[\bar{\Phi}^m]$, the quantity $\widehat{w}(2\pi\nu)$ is rewritten as $\widehat{w}^m(2\pi\nu)$. When dealing with the second reduction, involving the modal matrix $[\Phi^{m,N}]$, the quantity $\widehat{w}(2\pi\nu)$ is rewritten as $\widehat{w}^{m,N}(2\pi\nu)$.

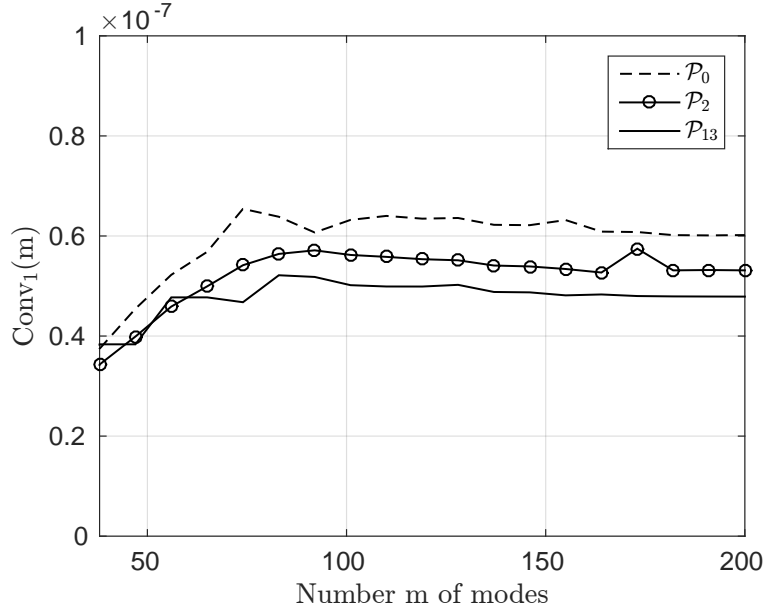


Figure 4.11 – Convergence analysis with respect to the reduced order m of the NL-ROMF: graphs of function $m \mapsto Conv_1(m)$ for patterns $\mathcal{P}_0 = 24A$, $\mathcal{P}_2 = (AB)_{12}$, and $\mathcal{P}_{13} = 6B12A3B3A$.

A first convergence analysis is performed with respect to the number m of modes that are kept for constructing the NL-ROMF. Let $Conv_1(m)$ be the function defined by

$$Conv_1(m) = \sqrt{\int_{\mathbb{B}_a} (\hat{w}^m(2\pi\nu))^2 d\nu}. \quad (4.10)$$

Figure 4.11 displays the graph of function $m \mapsto Conv_1(m)$ for three different patterns. The considered configurations are the tuned pattern $\mathcal{P}_0 = 24A$ and two detuned patterns ($\mathcal{P}_2 = (AB)_{12}$ and $\mathcal{P}_{13} = 6B12A3B3A$). A good convergence is obtained for $m = 145$ that will be the retained value. A second convergence analysis is then carried out with respect to $N < m = 145$ according to Eq. (3.21). Let $Conv_2(m, N)$ be the function defined by

$$Conv_2(m, N) = \sqrt{\int_{\mathbb{B}_a} (\hat{w}^{m,N}(2\pi\nu))^2 d\nu}. \quad (4.11)$$

Figure 4.12 displays the graph of function $N \mapsto Conv_2(m = 145, N)$. It can be seen that a good approximation is obtained for $N = 55$, which shows the efficiency of the reduction strategy that is proposed.

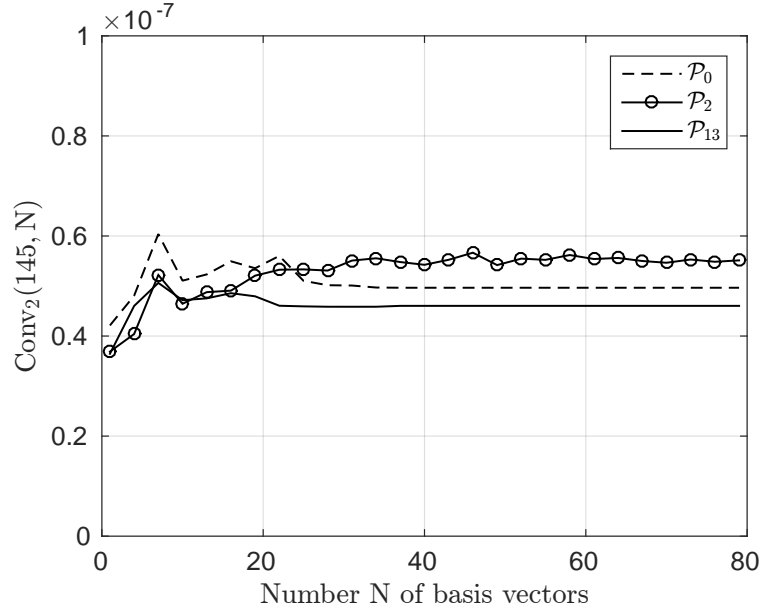


Figure 4.12 – Convergence analysis with respect to the reduced order N of the NL-ROM for $m = 145$: graphs of function $N \mapsto \text{Conv}_2(m, N)$ for patterns $\mathcal{P}_0 = 24A$, $\mathcal{P}_2 = (AB)_{12}$, and $\mathcal{P}_{13} = 6B12A3B3A$.

4.4.5 Sensitivity analysis of the deterministic responses for the nonlinear tuned rotating bladed-disk with respect to amplitude s_0 of the excitation

The sensitivity analysis of the intensity s_0 of the external load is performed using the NL-ROMF with $m = 145$ for the nonlinear tuned rotating bladed-disk (pattern $\mathcal{P}_0 = 24A$). The objective is to determine the value of parameter s_0 for which the geometric nonlinear effects occur in the dynamic response. This analysis is performed by quantifying the energy i_{NL} outside the excitation frequency band \mathbb{B}_e (that is to say, in the band $\mathbb{B}_a \setminus \mathbb{B}_e$) such that

$$i_{\text{NL}}(s_0) = \frac{\sqrt{\int_{\mathbb{B}_a \setminus \mathbb{B}_e} (\hat{w}(2\pi\nu; s_0))^2 d\nu}}{\sqrt{\int_{\mathbb{B}_e} (\hat{w}(2\pi\nu; s_0))^2 d\nu}} . \quad (4.12)$$

Figure 4.13 displays the graph of function $s_0 \mapsto i_{\text{NL}}(s_0)$. It can be seen that geometric nonlinear effects appear for $s_0 > 0.10$. Strictly speaking, the NL-ROM that was built for $m = 145$ is only valid for $s_0 \leq 1$. However, Figure 4.13 shows the value of $i_{\text{NL}}(s_0)$ for $s_0 > 1$, and for which the convergence for $m = 145$ is not

assured. However, the objective of Figure 4.13 is to find from what value of s_0 the nonlinear regime is reached. This one is clearly identified with $s_0 = 0.1 < 1$.

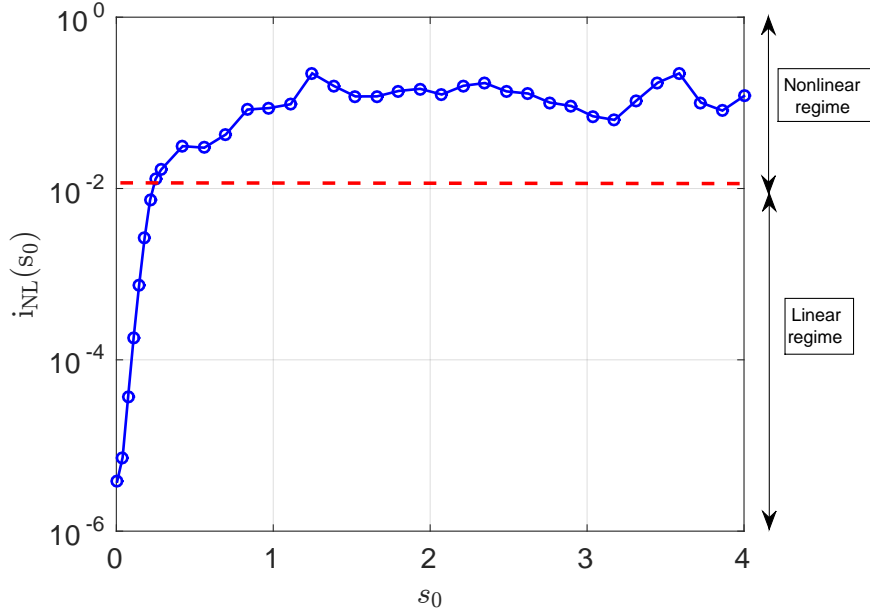


Figure 4.13 – Sensitivity analysis with respect to parameter s_0 using the NL-ROMF for the nonlinear tuned rotating bladed-disk structure (pattern $\mathcal{P}_0 = 24A$): graph of function $s_0 \mapsto i_{\text{NL}}(s_0)$. The red dashed line represents the boundary between the linear and nonlinear regimes

Figure 4.14 displays the graph of function $\nu \mapsto \|\widehat{\mathbf{u}}^{j_0}(2\pi\nu)\|$ constructed with the NL-ROMF for s_0 equal to 0.04 (response belonging to the quasi-linear regime of the nonlinear response), and equal to 0.25, 1, and 4.0 (response belonging to the nonlinear regime of the nonlinear response). The left top figure clearly shows a dynamic response that remains in the linear regime (there is no response outside \mathbb{B}_e). On the other hand, subsequent contributions with unexpected resonances appear outside \mathbb{B}_e in the frequency band $\mathbb{B}_a \setminus \mathbb{B}_e$ as soon as s_0 increases. For $s_0 = 0.04$, the nonlinear geometric effects are negligible, for $s_0 = 0.25$, the nonlinear geometric effects are moderate, and for $s_0 = 1$ the effects are strong. Note that the value $s_0 = 4$ has also been used for the sensitivity analysis but the convergence with respect to m is not ensured.

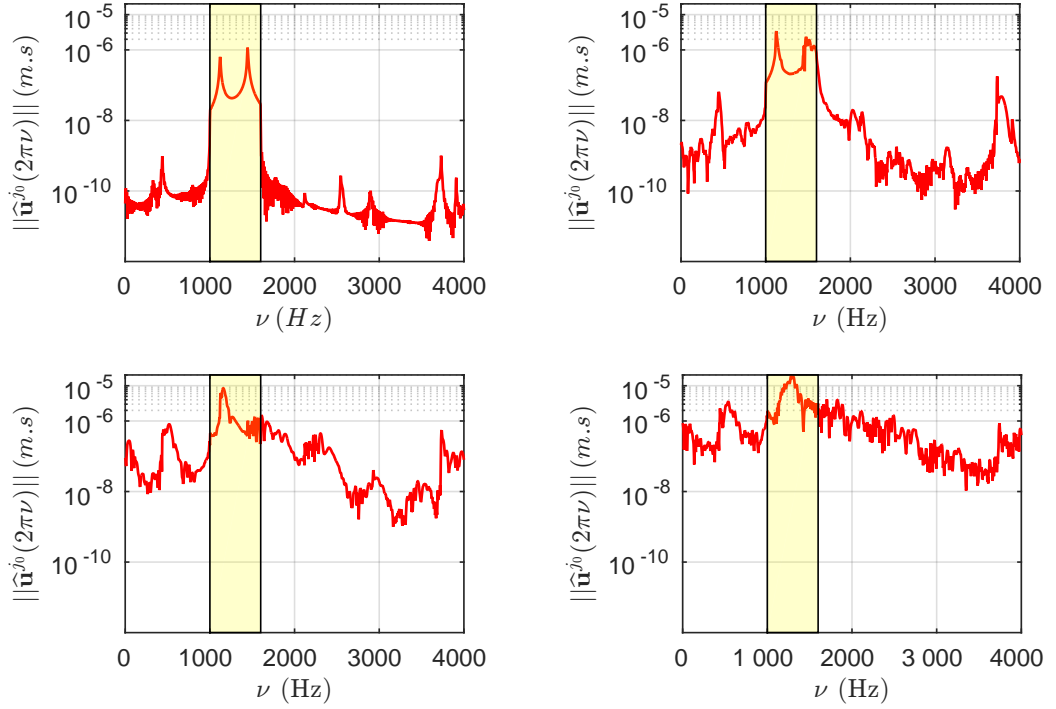


Figure 4.14 – Sensitivity analysis with respect to parameter s_0 of the responses computed with the NL-ROMF and analyzed in the frequency domain: graphs of function $\nu \mapsto \|\hat{\mathbf{u}}^{j_0}(2\pi\nu)\|$ for $s_0 = 0.04$ (left top figure), $s_0 = 0.25$ (right top figure), $s_0 = 1$ (left down figure), and $s_0 = 4.0$ (right down figure). The light yellow zone corresponds to the excitation frequency band \mathbb{B}_e

4.4.6 Linear and nonlinear dynamic analyses in the time domain using the L-ROM and NL-ROM

In this section, the linear and nonlinear dynamic responses of the tuned configuration (pattern $\mathcal{P}_0 = 24A$) and three detuned configurations (patterns $\mathcal{P}_6 = (4A2B)_4$, $\mathcal{P}_{11} = B4AB18A$, $\mathcal{P}_{25} = 3A3B3A15B$) are analyzed for $s_0 = 1$. Figure 4.15 displays the graph of function $t \mapsto u_{2,L}^{j_0}(t)$ for patterns $(\mathcal{P}_0, \mathcal{P}_6, \mathcal{P}_{11}, \mathcal{P}_{25})$ corresponding to a linear computation performed with the L-ROM defined by Eq (3.15). Figure 4.16 displays the graph of $t \mapsto u_{2,NL}^{j_0}(t)$ for patterns $(\mathcal{P}_0, \mathcal{P}_6, \mathcal{P}_{11}, \mathcal{P}_{25})$ corresponding to the nonlinear computation performed with the NL-ROM. By comparing the nonlinear results with the linear ones, it can be seen that strong nonlinear geometric effects that mitigate the amplitude of the responses and show "irregular" responses, suggesting numerous resonances contributing outside band

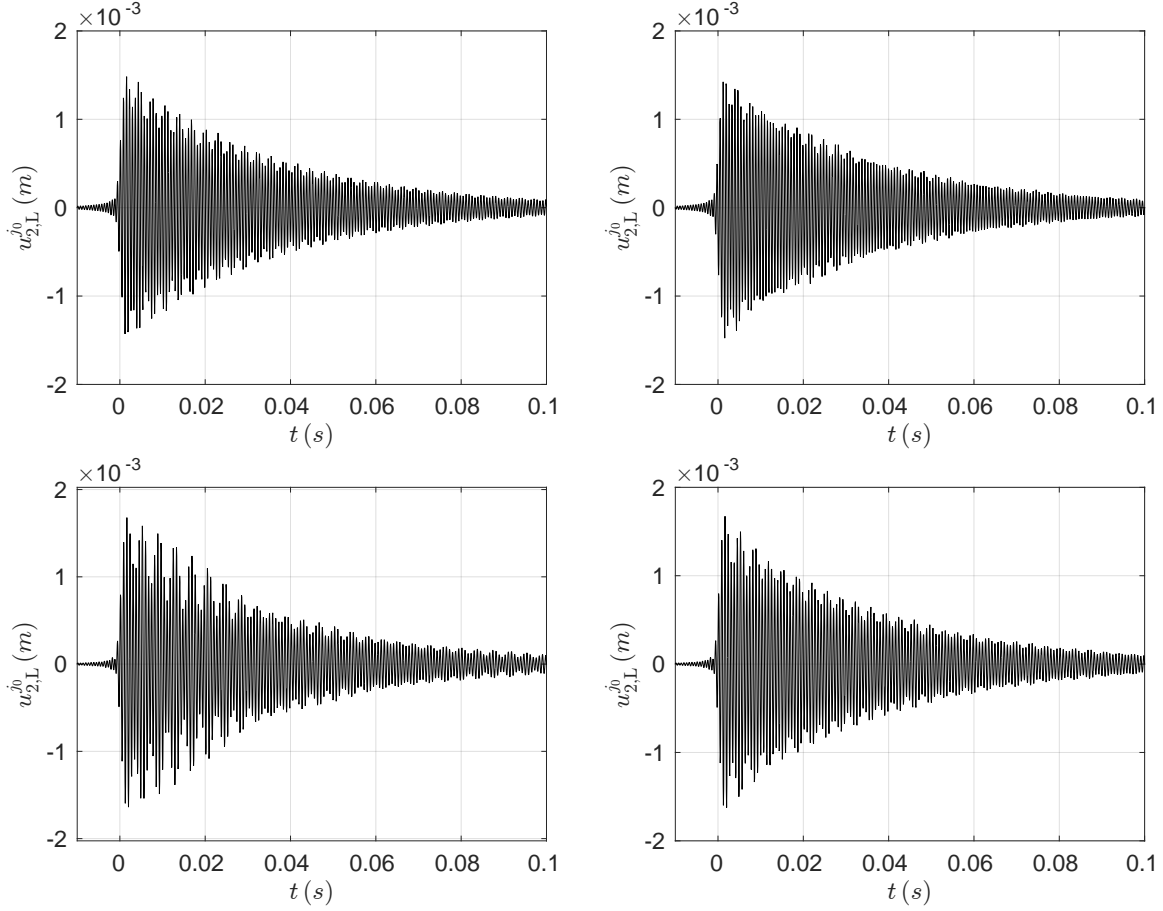
\mathbb{B}_e .


Figure 4.15 – Zoom on the time interval $[-0.01, 0.1]$ s of the linear dynamic analysis in the time domain performed with the L-ROM: graph of function $t \mapsto u_{2,L}^{j_0}(t)$ defined on the time interval $[-0.05, 1.5]$ s for the patterns \mathcal{P}_0 (left top figure), \mathcal{P}_6 (right top), \mathcal{P}_{11} (left down), and \mathcal{P}_{25} (right down).

4.4.7 Analysis of the nonlinear dynamic time responses in the frequency domain

As previously explained, a Fourier transform of the time responses constructed with the L-ROM (linear) and the NL-ROM (nonlinear) is performed, allowing the spectrum of the responses to be analyzed in the frequency band of analysis $\mathbb{B}_a = [0, 4000]$ Hz. We are interested in the dynamic amplification factor $b(2\pi\nu)$ (defined by Eq. (4.8)) with respect to the tuned configuration. Figure 4.17 displays

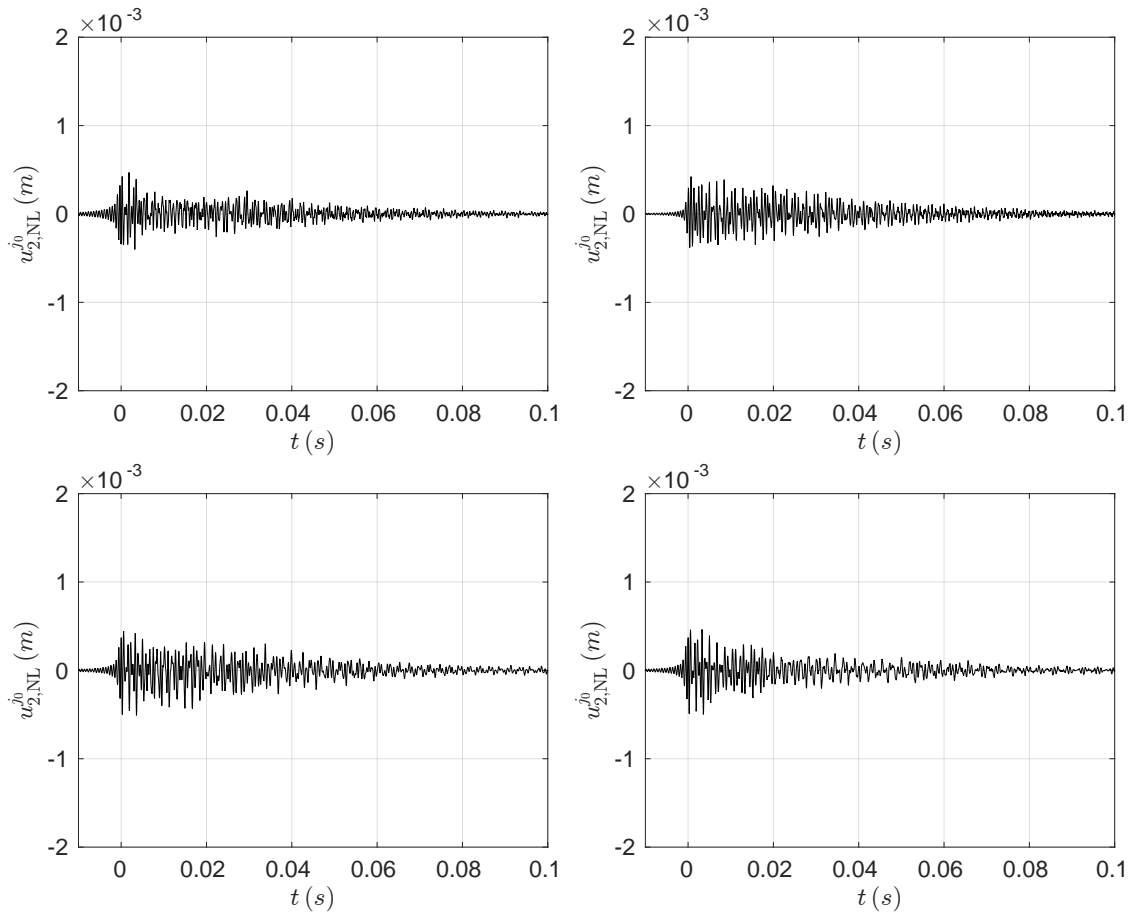


Figure 4.16 – Zoom on the time interval $[-0.01, 0.1]$ s of the nonlinear dynamic analysis in the time domain performed with the NL-ROM: graph of function $t \mapsto u_{2,NL}^{j_0}(t)$ defined on the time interval $[-0.05, 1.5]$ s for the patterns \mathcal{P}_0 (left top figure), \mathcal{P}_6 (right top), \mathcal{P}_{11} (left down), and \mathcal{P}_{25} (right down).

the graphs of functions $\nu \mapsto b_L(2\pi\nu)$ (linear) and $\nu \mapsto b_{NL}(2\pi\nu)$ (nonlinear) for the rotating tuned bladed-disk (pattern \mathcal{P}_0) and for the rotating detuned bladed-disk structures (patterns \mathcal{P}_6 , \mathcal{P}_{11} , \mathcal{P}_{25}). By comparing the linear responses with the nonlinear ones, it can be seen the strong effects of the nonlinearities outside the frequency band of excitation \mathbb{B}_e and that new resonances occur below and above this frequency band \mathbb{B}_e . Such phenomena has previously been observed [35, 45] in the turbomachinery context.

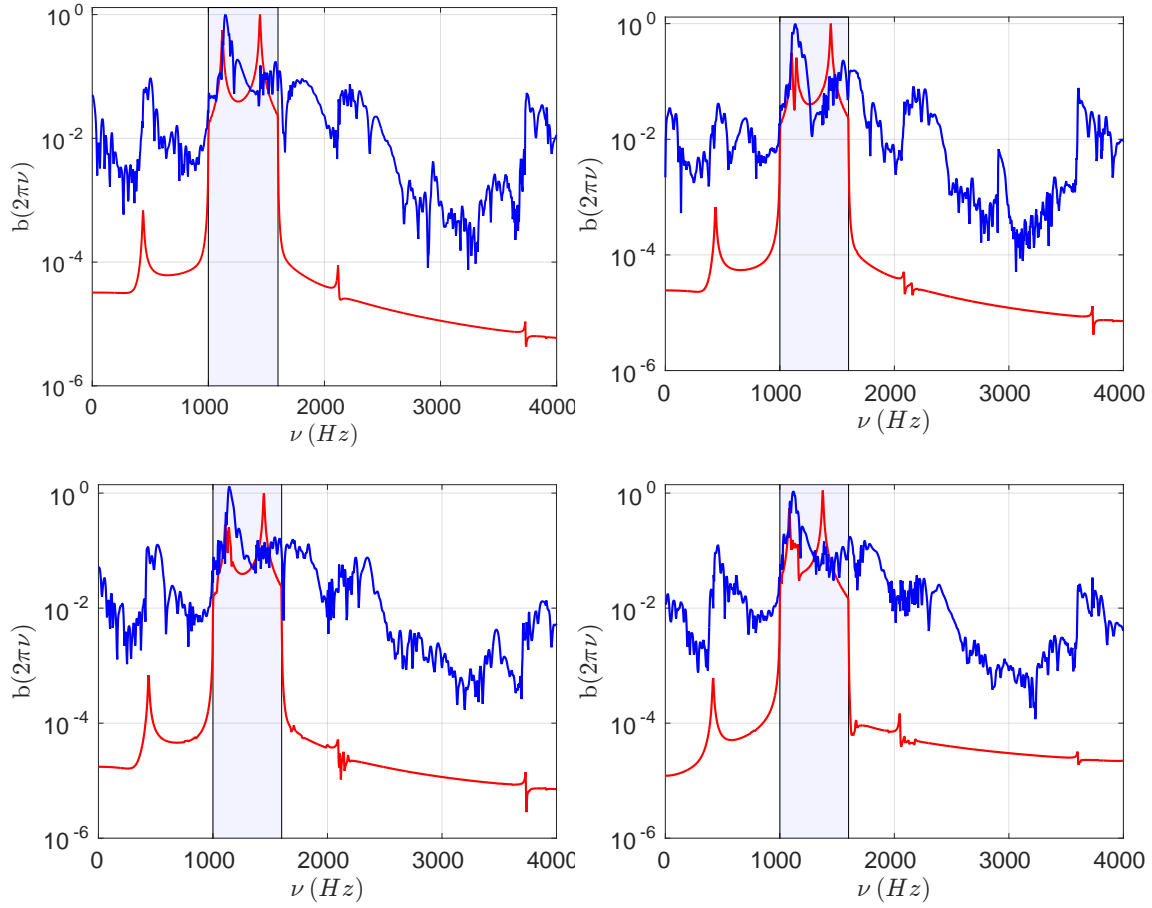


Figure 4.17 – Frequency analysis of the time responses computed with the NL-ROM: graphs of functions $\nu \mapsto b_L(2\pi\nu)$ (red smooth thin lines) and $\nu \mapsto b_{NL}(2\pi\nu)$ (blue irregular thick lines) for patterns \mathcal{P}_0 (left top figure), \mathcal{P}_6 (right top figure), \mathcal{P}_{11} (left down figure), and \mathcal{P}_{25} (right down figure). The excitation frequency band \mathbb{B}_e is in light grey area.

Chapter 5

Probabilistic model of mistuning for the mistuned-detuned bladed-disk structures

Contents

5.1	Introduction	54
5.2	Ensemble SG_0^+ of positive-definite random matrices	54
5.2.1	Available information	54
5.2.2	Probability distribution of random matrix $[\mathbf{G}]$	55
5.2.3	Dispersion parameter	55
5.2.4	Algebraic representation of random matrix $[\mathbf{G}]$	56
5.3	Ensemble SE_0^+ of positive-definite random matrices	56
5.4	Construction of linear and nonlinear stochastic reduced-order models	57
5.4.1	Global stiffness matrix	57
5.4.2	Stochastic nonlinear reduced-order model NL-SROM1 of a rotating detuned bladed-disk structure with mistuning	57
5.4.3	Stochastic nonlinear reduced-order model NL-SROM2 of a rotating detuned bladed-disk structure with mistuning	59
5.4.4	Stochastic linear reduced-order model L-SROM of a rotating detuned bladed-disk with mistuning	59

5.1 Introduction

As explained in Chapter 1, the mistuning phenomenon is modeled using a probabilistic approach of uncertainties. We recall that there exist two types of probabilistic approaches.

- The first one is called the parametric probabilistic approach: in such an approach, the parameters of the computational model are modeled by random variables.
- The second one is called the nonparametric probabilistic approach: it allows for taking into account both parameter uncertainties and model uncertainties [99]. The nonparametric probabilistic approach consists in replacing the matrices issued from a reduced-order model by random matrices. This means that the probability distribution is directly constructed from the reduced operators. It is constructed using the maximum entropy principle [121] with the available information [122]. It should be noted that only a scalar hyperparameter controls the uncertainty level for each reduced operator.

In the present work the mistuning phenomenon is modeled with the nonparametric probabilistic approach. Below we recall the main theoretical steps for constructing the probability model. Sections 5.2 and 5.2.2 are taken from [99].

5.2 Ensemble SG_0^+ of positive-definite random matrices

5.2.1 Available information

A random matrix $[\mathbf{G}]$ in SG_0^+ is a random matrix, defined on the probability space $(\Theta, \mathcal{T}, \mathcal{P})$, with values in $\mathbb{M}_n^+(\mathbb{R})$, which is constructed by using the Maximum Entropy principle with the following available information

- Positive-definite matrix: Full random matrix $[\mathbf{G}]$ is almost surely in $\mathbb{M}_n^+(\mathbb{R})$.
- Statistical mean: Statistical mean of random matrix $[\mathbf{G}]$ is equal to the identity matrix, that is to say

$$E\{[\mathbf{G}]\} = [I_n] \quad (5.1)$$

in which $E\{.\}$ is the mathematical expectation.

- Integrability of the inverse: A random matrix $[\mathbf{G}]$, which belongs to SG_0^+ , is a second-order random variable, must verify the following integrability property for its inverse

$$E\{\log(\det[\mathbf{G}])\} = \nu_G \quad , \quad |\nu_G| < +\infty \quad (5.2)$$

5.2.2 Probability distribution of random matrix $[\mathbf{G}]$

The probability distribution of random matrix $[\mathbf{G}]$ is defined by a probability density function $p_{[\mathbf{G}]}([G])$, with respect to $\tilde{d}G$ such that

$$\tilde{d}G = 2^{n(n-1)/4} \times \prod_{1 \leq j \leq k \leq n} d[G]_{jk} \quad , \quad (5.3)$$

which is written as

$$p_{[\mathbf{G}]}([\mathbf{G}]) = \mathbb{1}_{\mathbb{M}_n^+(\mathbb{R})}([\mathbf{G}]) \times C_{\mathbf{G}} \times (\det([\mathbf{G}]))^{(n+1)\frac{1-\delta^2}{2\delta^2}} \times e^{-\frac{n+1}{2\delta^2} \text{tr}([\mathbf{G}])} \quad , \quad (5.4)$$

where $\mathbb{1}_{\mathbb{M}_n^+(\mathbb{R})}([G])$ is the indicator function of the set $\mathbb{M}_n^+(\mathbb{R})$ defined by $\mathbb{1}_{\mathbb{M}_n^+(\mathbb{R})}([G]) = 1$ if $[G] \in \mathbb{M}_n^+(\mathbb{R})$ and $\mathbb{1}_{\mathbb{M}_n^+(\mathbb{R})}([G]) = 0$ if $[G] \notin \mathbb{M}_n^+(\mathbb{R})$. The normalization positive constant $C_{\mathbf{G}}$ is such that

$$C_{\mathbf{G}} = (2\pi)^{-n(n-1)/4} \left(\frac{n+1}{2\delta^2} \right)^{\frac{n(n+1)}{2\delta^2}} \left\{ \prod_{j=1}^n \Gamma \left(\frac{n+1}{2\delta^2} + \frac{1-j}{2} \right) \right\}^{-1} \quad (5.5)$$

in which

$$\Gamma(z) = \int_0^{+\infty} t^{z-1} e^{-t} dt \quad , \quad \forall z > 0 \quad (5.6)$$

5.2.3 Dispersion parameter

The dispersion parameter δ , allowing for controlling the level of the statistical fluctuations of $[\mathbf{G}]$, is defined by

$$\delta = \left\{ \frac{E \{ \|[[\mathbf{G}] - [I_n]]\|_F^2 \}}{\|[[I_n]]\|_F^2} \right\}^{\frac{1}{2}} \quad . \quad (5.7)$$

Parameter δ must be chosen such that

$$0 < \delta < (n+1)^{1/2} (n+5)^{-1/2} \quad . \quad (5.8)$$

5.2.4 Algebraic representation of random matrix $[\mathbf{G}]$

The following algebraic representation of $[\mathbf{G}] \in SG_0^+$ gives an explicit generator of realizations of random matrix $[\mathbf{G}]$,

$$[\mathbf{G}] = [\mathbf{L}]^T[\mathbf{L}], \quad (5.9)$$

in which $[\mathbf{L}]$ is an upper triangular random matrix with values in $\mathbb{M}_n(\mathbb{R})$ such that

- (1) the random variables $\{[\mathbf{L}]_{jj'}, j \leq j'\}$ are mutually independent.
- (2) for $j < j'$, we have $[\mathbf{L}]_{jj'} = \sigma U_{jj'}$, in which $\sigma = \delta(n+1)^{-1/2}$ and where $U_{jj'}$ is a real-valued Gaussian random variable with zero mean and with a variance that is equal to 1.
- (3) for $j = j'$, we have $[\mathbf{L}]_{jj} = \sigma\sqrt{2V_j}$, where V_j is a positive-valued Gamma random variable whose probability density function with respect to $d\nu$ is written as

$$p_{V_j}(\nu) = \mathbb{1}_{\mathbb{R}^+}(\nu) \frac{1}{\Gamma\left(\frac{n+1}{2\delta^2} + \frac{1-j}{2}\right)} \nu^{\frac{n+1}{2\delta^2} - \frac{1+j}{2}} e^{-\nu}. \quad (5.10)$$

5.3 Ensemble SE_0^+ of positive-definite random matrices

Let $[A]$ be a deterministic matrix given in $\mathbb{M}_n^+(\mathbb{R})$ and representing a given mean value that is different from the identity matrix. Any random matrix $[\mathbf{A}]$ in SE_0^+ is with values in $\mathbb{M}_n^+(\mathbb{R})$, and is such that

$$E\{[\mathbf{A}]\} = [A] \in \mathbb{M}_n^+(\mathbb{R}) \quad (5.11)$$

$$E\{\log(\det[\mathbf{A}])\} = \nu_A, \quad |\nu_A| < +\infty. \quad (5.12)$$

Random matrix $[\mathbf{A}]$ is written as

$$[\mathbf{A}] = [L_A]^T[\mathbf{G}][L_A], \quad [\mathbf{G}] \in SG_0^+, \quad (5.13)$$

in which $[A] = [L_A]^T[L_A]$.

5.4 Construction of linear and nonlinear stochastic reduced-order models

In this section, the construction principle of the stochastic nonlinear reduced-order model of the rotating detuned-mistuned bladed-disk structure is presented. The tuned-mistuned case is also presented. We recall that the dimension of the computational NL-HFM is n , the dimension of the reduced NL-ROMF is m , and the dimension of the NL-ROM is N . Here, we introduce two probabilistic models from the NL-ROM, yielding two nonlinear stochastic reduced-order models, NL-SROM1 and NL-SROM2. The implementation of uncertainties is performed only on the nonlinear stiffness forces (including the linear and the nonlinear operators) and is based on the methodology presented in [91].

5.4.1 Global stiffness matrix

Let $[\mathcal{K}^{\text{NL}}]$ be the $(N_K \times N_K)$ real matrix, with $N_K = N(N + 1)$, such that

$$[\mathcal{K}^{\text{NL}}] = \begin{bmatrix} [\mathcal{K}_e] & [\widehat{\mathcal{K}}^{(2)}] \\ [\widehat{\mathcal{K}}^{(2)T}] & 2[\mathcal{K}^{(3)}] \end{bmatrix}, \quad (5.14)$$

in which $[\mathcal{K}_e]$ is the reduced elastic matrix defined in Eq. (3.25) and where $[\widehat{\mathcal{K}}^{(2)}]$ and $[\mathcal{K}^{(3)}]$ are respectively the $(N \times N^2)$ and $(N^2 \times N^2)$ real matrices resulting from the following reshaping operation,

$$[\widehat{\mathcal{K}}^{(2)}]_{\alpha J} = \widehat{\mathcal{K}}_{\alpha\gamma\delta}^{(2)} \quad , \quad [\mathcal{K}^{(3)}]_{IJ} = \mathcal{K}_{\alpha\beta\gamma\delta}^{(3)}, \quad (5.15)$$

with $I = (\alpha - 1)N + \beta$ and $J = (\gamma - 1)N + \delta$. It is proven in [91] that matrix $[\mathcal{K}^{\text{NL}}]$ is positive definite, allowing for applying the nonparametric probabilistic approach for this matrix.

5.4.2 Stochastic nonlinear reduced-order model NL-SROM1 of a rotating detuned bladed-disk structure with mistuning

For this stochastic nonlinear computational model NL-SROM1, it is assumed that the random uncertainties affect all the contributions of the global stiffness matrix $[\mathcal{K}^{\text{NL}}]$. Since the dimension of matrix $[\mathcal{K}^{\text{NL}}]$ is huge, applying the usual nonparametric probabilistic approach would yield to a very large number of random

variables. Instead of performing a Cholesky factorization of matrix $[\mathcal{K}^{\text{NL}}]$, it is proposed in [101] another factorization that allows for reducing the number of random variables by introducing a matrix of size $\tilde{N}_K \times \tilde{N}_K$ with $\tilde{N}_K \ll N_K$. Let us then consider the eigenvalue problem

$$[\mathcal{K}^{\text{NL}}]\Psi_\alpha = \lambda_\alpha\Psi_\alpha \quad (5.16)$$

Matrix $[\mathcal{K}^{\text{NL}}]$ can then be approximated by the $(N_K \times N_K)$ matrix $[\tilde{K}^{\text{NL}}]$ such that

$$[\tilde{K}^{\text{NL}}] = [\tilde{L}_K]^T[\tilde{L}_K], \quad (5.17)$$

in which $[\tilde{L}_K]$ is the full $(\tilde{N}_K \times N_K)$ matrix defined by

$$[\tilde{L}_K] = [\Lambda^{\tilde{N}_K}]^{\frac{1}{2}}[\Psi^{\tilde{N}_K}]^T \quad (5.18)$$

where $[\Lambda^{\tilde{N}_K}]$ is the $(\tilde{N}_K \times \tilde{N}_K)$ diagonal matrix such that $[\Lambda^{\tilde{N}_K}]_{\alpha\alpha} = \lambda_\alpha$, where $\lambda_1 \geq \lambda_2 \geq \dots \geq \lambda_{\tilde{N}_K}$ and where the columns of the $(N_K \times \tilde{N}_K)$ matrix $[\Psi^{\tilde{N}_K}]$ is the matrix containing the \tilde{N}_K eigenvectors ψ_α , $\alpha \in \{1, \dots, \tilde{N}_K\}$, related to eigenvalues λ_α such that

$$[\Psi^{\tilde{N}_K}]^T[\Psi^{\tilde{N}_K}] = [I_{\tilde{N}_K}] \quad (5.19)$$

Random matrix $[\mathcal{K}^{\text{NL}}]$ is then replaced by the random matrix $[\tilde{\mathcal{K}}^{\text{NL}}]$ such that

$$[\tilde{\mathcal{K}}^{\text{NL}}] = [\tilde{L}_K]^T[\tilde{\mathbf{G}}_K(\delta_K)][\tilde{L}_K] + [\Delta\tilde{\mathcal{K}}], \quad (5.20)$$

in which $[\tilde{\mathbf{G}}_K(\delta_K)]$ is a $(\tilde{N}_K \times \tilde{N}_K)$ random matrix belonging to set G_0^+ and where $[\Delta\tilde{\mathcal{K}}]$ is the $(\tilde{N}_K \times \tilde{N}_K)$ real matrix written as

$$[\Delta\tilde{\mathcal{K}}] = [\mathcal{K}^{\text{NL}}] - [\tilde{L}_K]^T[\tilde{L}_K]. \quad (5.21)$$

We have $E\{[\tilde{\mathcal{K}}^{\text{NL}}]\} = [\tilde{\mathcal{K}}^{\text{NL}}]$ because $E\{[\tilde{\mathbf{G}}_K(\delta_K)]\} = [I_{\tilde{N}_K}]$. The hyperparameter δ_K allows for controlling the level of uncertainties in random matrix $[\tilde{\mathcal{K}}^{\text{NL}}]$. The random linear, quadratic, and cubic coefficients, $[\mathcal{K}_e]_{\alpha\beta}$, $\mathcal{K}_{\alpha\beta\gamma}^{(2)}$, and $\mathcal{K}_{\alpha\beta\gamma\delta_K}^{(3)}$, are extracted from random matrix $[\tilde{\mathcal{K}}^{\text{NL}}]$ that have the same bloc structure as its deterministic counterpart defined in Eq. (5.14).

The first stochastic nonlinear reduced-order model, NL-SROM1, is then written as,

$$\mathbf{U}(t) = [\Phi^{(m,N)}] \mathbf{Q}(t), \quad (5.22)$$

$$[\mathcal{M}] \ddot{\mathbf{Q}}(t) + ([\mathcal{D}] + [\mathcal{C}(\Omega)]) \dot{\mathbf{Q}}(t) + ([\mathcal{K}_e] + [\mathcal{K}_c(\Omega)] + [\mathcal{K}_g(\Omega)]) \mathbf{Q}(t) + \mathcal{F}^{\text{NLS}}(\mathbf{Q}(t)) = \mathcal{F}(t), \quad (5.23)$$

in which $\mathbf{Q}(t)$ is the \mathbb{R}^N -valued random vector of the generalized coordinates. In Eq. (5.23), the vector of the stochastic nonlinear internal forces $\mathcal{F}^{\text{NLS}}(\mathbf{Q}(t))$ is written, for all $\mathbf{q} = (q_1, \dots, q_N)$ as

$$\mathcal{F}_\alpha^{\text{NLS}}(\mathbf{q}) = \mathcal{K}_{\alpha\beta\gamma}^{(2)} q_\beta q_\gamma + \mathcal{K}_{\alpha\beta\gamma\delta}^{(3)} q_\beta q_\gamma q_\delta. \quad (5.24)$$

5.4.3 Stochastic nonlinear reduced-order model NL-SROM2 of a rotating detuned bladed-disk structure with mistuning

The second nonlinear stochastic reduced-order model NL-SROM2 only takes into account uncertainties on the linear elastic part of the rotating detuned-mistuned bladed-disk structure. Consequently, random matrix $[\mathcal{K}_e]$ is written as

$$[\mathcal{K}_e] = [L_{\mathcal{K}_e}]^T [\mathbf{G}_K(\delta_K)] [L_{\mathcal{K}_e}], \quad (5.25)$$

in which $[L_{\mathcal{K}_e}]$ is the upper triangular ($N \times N$) real matrix, which results from the Cholesky factorization of ($N \times N$) real matrix $[\mathcal{K}_e]$, and where $[\mathbf{G}_K(\delta_K)]$ is the ($N \times N$) random matrix belonging to SG_0^+ .

The second stochastic nonlinear reduced-order model, NL-SROM2, is then written as,

$$\mathbf{U}(t) = [\Phi^{(m,N)}] \mathbf{Q}(t), \quad (5.26)$$

$$[\mathcal{M}] \ddot{\mathbf{Q}}(t) + ([\mathcal{D}] + [\mathcal{C}(\Omega)]) \dot{\mathbf{Q}}(t) + ([\mathcal{K}_e] + [\mathcal{K}_c(\Omega)] + [\mathcal{K}_g(\Omega)]) \mathbf{Q}(t) + \mathcal{F}^{\text{NL}}(\mathbf{Q}(t)) = \mathcal{F}(t), \quad (5.27)$$

in which $\mathbf{Q}(t)$ is the \mathbb{R}^N -valued random vector of the generalized coordinates. In Eq. (5.27), the vector of the stochastic nonlinear internal forces $\mathcal{F}^{\text{NL}}(\mathbf{q}(t))$ is written, for all $\mathbf{q} = (q_1, \dots, q_N)$ as

$$\mathcal{F}_\alpha^{\text{NL}}(\mathbf{q}) = \mathcal{K}_{\alpha\beta\gamma}^{(2)} q_\beta q_\gamma + \mathcal{K}_{\alpha\beta\gamma\delta}^{(3)} q_\beta q_\gamma q_\delta. \quad (5.28)$$

5.4.4 Stochastic linear reduced-order model L-SROM of a rotating detuned bladed-disk with mistuning

We also introduce a stochastic linear reduced-order model L-SROM, which is the NL-SROM2, in which the nonlinear term \mathcal{F}^{NL} is removed. The stochastic linear reduced-order model, L-SROM, is then written as,

$$\mathbf{U}(t) = [\Phi^{(m,N)}] \mathbf{Q}(t), \quad (5.29)$$

$$[\mathcal{M}] \ddot{\mathbf{Q}}(t) + ([\mathcal{D}] + [\mathcal{C}(\Omega)]) \dot{\mathbf{Q}}(t) + ([\mathcal{K}_e] + [\mathcal{K}_c(\Omega)] + [\mathcal{K}_g(\Omega)]) \mathbf{Q}(t) = \mathcal{F}(t), \quad (5.30)$$

in which $\mathbf{Q}(t)$ is the \mathbb{R}^N -valued random vector of the generalized coordinates.

Chapter 6

Nonlinear stochastic computational dynamics of the mistuned-detuned bladed disk structure

Contents

6.1	Introduction	61
6.2	Convergence analyses	62
6.2.1	Convergence analysis with respect to \tilde{N}_K	62
6.2.2	Stochastic convergence analysis with respect to n_s	63
6.3	Linear and nonlinear stochastic analyses	65
6.3.1	Random dynamic amplification	65
6.3.2	Sensitivity analysis with respect to parameter s_0 for the rotating tuned and detuned bladed-disk structure in presence of mistuning	65
6.3.3	Stochastic analysis of nonlinear rotating tuned and detuned bladed-disk structure in presence of mistuning for different patterns	72
6.4	Discussion	72

6.1 Introduction

This section is devoted to the stochastic nonlinear dynamic analyses of the rotating detuned bladed-disk presented in Chapter 4 in presence of mistuning. More

particularly, four configurations are investigated: the tuned bladed-disk structure (pattern \mathcal{P}_0), and three arbitrary detuned configurations (patterns \mathcal{P}_6 , \mathcal{P}_{11} , and \mathcal{P}_{25}). The computation NL-ROM of these configurations is constructed with numerical parameters $m = 145$ and $N = 55$ (see Chapter 4). The first section deals with the convergence analysis of NL-SROM1 with respect (1) to parameter \tilde{N}_K controlling the dimension of the random matrix $[\tilde{\mathbf{G}}_K]$ (see Section 5.4.2) and (2) to parameter n_s controlling the number of realizations used in the Monte-Carlo numerical simulation. The second section concerns the numerical results that consist in the confidence region of the nonlinear stochastic responses related to the investigated tuned and detuned configurations obtained with L-SROM, NL-SROM1, and NL-SROM2.

6.2 Convergence analyses with respect to \tilde{N}_K and n_s

The convergence analyses with respect to \tilde{N}_K and n_s are presented, and allows for reducing the size of the germ matrix $[\tilde{\mathbf{G}}_K]$ and for defining an optimal number n_s of Monte-Carlo numerical simulations.

6.2.1 Convergence analysis with respect to \tilde{N}_K

From Section 4.4.4, dimension N of the NL-ROM is fixed to 55. Consequently, dimension N_K of the global stiffness matrix $[\mathcal{K}^{\text{NL}}]$ defined by Eq. (5.14) is $55 \times 56 = 3080$. We are then interested in quantifying the numerical error resulting from the factorization of matrix $[\mathcal{K}^{\text{NL}}]$ which depends on the number of \tilde{N}_K related to the dimension of matrix $[\Psi^{\tilde{N}_K}]$.

Following [101], we introduce the relative error function $\tilde{N}_K \mapsto \text{err}(\tilde{N}_K)$ such that

$$\text{err}(\tilde{N}_K) = \sqrt{\frac{\|[\Delta\tilde{\mathcal{K}}]\|_{\text{F}}^2}{\|[\mathcal{K}^{\text{NL}}]\|_{\text{F}}^2}}. \quad (6.1)$$

Figure 6.1 displays the graph of $\tilde{N}_K \mapsto \text{err}(\tilde{N}_K)$. A good convergence is obtained for $\tilde{N}_K = 500$ corresponding to a relative error $\text{err}(\tilde{N}_K) = 10^{-6}$. This means that the dimension of random matrix $[\mathbf{G}_K]$ is reduced from 3080 to 500, which allows for reducing the computational cost.

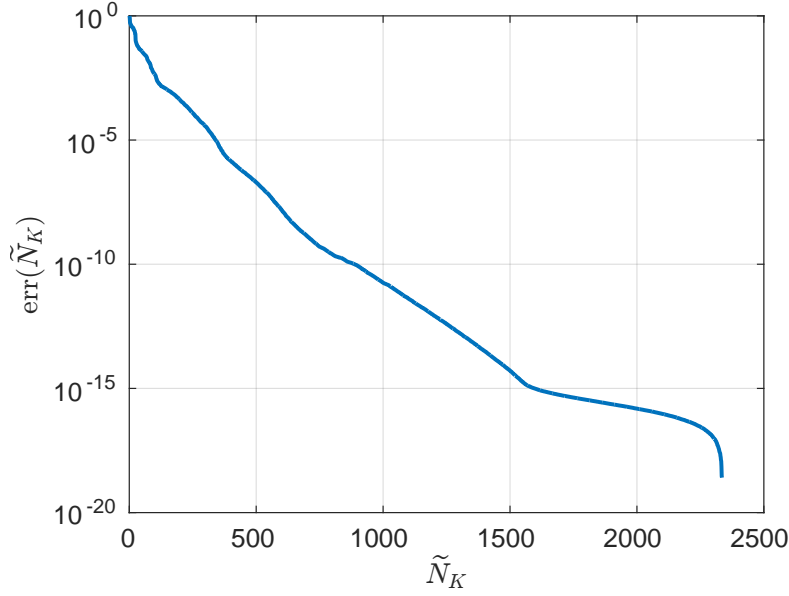


Figure 6.1 – Convergence analysis with respect to parameter \tilde{N}_K : graph of function $\tilde{N}_K \mapsto \text{err}(\tilde{N}_K)$ in log-scale.

6.2.2 Stochastic convergence analysis with respect to n_s

Parameters m , N , and \tilde{N}_K are fixed such that $m = 145$, $N = 55$, and $\tilde{N}_K = 500$. The range of values of hyperparameter δ_K that will be used for performing the sensitivity analysis of the nonlinear dynamical response with respect to the level of uncertainties, will be $0 < \delta_K < 0.1$. The convergence analysis is thus performed for the larger value 0.1 of δ_K ensuring the convergence for all values of δ_K less than 0.1. Let

$$\hat{\mathcal{W}}(2\pi\nu) = \sqrt{\sum_{j=1}^M \|\hat{\mathbf{U}}^j(2\pi\nu)\|^2} \quad (6.2)$$

be the random observation defined similarly to Eq. (4.9). The stochastic Eq. (5.23) is solved by using the Monte-Carlo numerical simulation with n_s realizations denoted by $\theta_1, \dots, \theta_{n_s}$. Let $\hat{\mathcal{W}}(2\pi\nu, \theta_\ell)$ be the realization θ_ℓ of the random variable $\hat{\mathcal{W}}(2\pi\nu)$. The convergence analysis with respect to n_s is then carried out studying the function $n_s \mapsto \text{Conv}(n_s)$ defined by

$$\text{Conv}(n_s) = \sqrt{\frac{1}{n_s} \sum_{\ell=1}^{n_s} \int_{\mathbb{B}_a} (\hat{\mathcal{W}}(2\pi\nu, \theta_\ell))^2 d\nu} \quad (6.3)$$

Figure 6.2 displays the graph of function $n_s \mapsto Conv(n_s)$. It can be seen that a reasonable approximation is obtained for $n_s \geq 500$. In order to limit the CPU-time for performing the robust analysis of the detuned systems in presence of mistuning, the chosen value 500 of parameter n_s is retained.

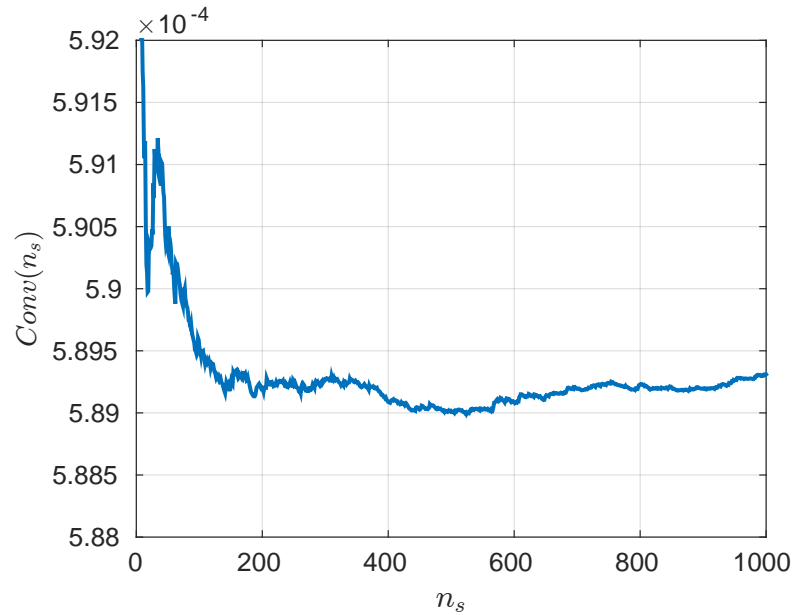


Figure 6.2 – Convergence analysis with respect to the number n_s of realizations for the Monte-Carlo numerical simulation of the NL-SROM1: graph of function $n_s \mapsto Conv(n_s)$.

6.3 Linear and nonlinear stochastic analyses

In this section, we consider the following cases: the nonlinear rotating tuned bladed-disk structure in presence of mistuning and also three configurations of the rotating detuned bladed-disk structure in presence of mistuning. The nonlinear computational analyses are carried out using the NL-SROM1, the NL-SROM2, and the L-SROM defined in Chapter 5.

6.3.1 Random dynamic amplification

As explained in Section 4.4.2, we are interested in characterizing the amplification levels for the stochastic nonlinear responses. We thus introduce the quantity $B(2\pi\nu)$ as the random dynamic amplification factor such that

$$B(2\pi\nu) = \frac{\|\widehat{\mathbf{U}}^{j_0}(2\pi\nu)\|}{\|\widehat{\mathbf{u}}^{j_0, \text{tuned}}\|}, \quad (6.4)$$

in which

$$\|\widehat{\mathbf{U}}^{j_0}(2\pi\nu)\|^2 = \sum_{k=1}^3 |\widehat{U}_k^{j_0}(2\pi\nu)|^2 \quad (6.5)$$

is a random observation of blade j_0 , expressed in the frequency domain .

6.3.2 Sensitivity analysis with respect to parameter s_0 for the rotating tuned and detuned bladed-disk structure in presence of mistuning

The objective is to quantify and to give explanations concerning the effects of the level of uncertainties related to the level of mistuning. In that sense, a parametric analysis is carried out with respect to (i) the dispersion parameter δ_K that controls the level of uncertainties in the computational model and (ii) parameter s_0 that controls the amplitude of the external excitation, that is to say that allows the geometric nonlinear effects to be controlled. A comparison is performed between the linear stochastic responses computed with L-SROM and the nonlinear stochastic responses computed with NL-SROM2 for hyperparameter δ_K fixed to 0.1. Let $\widehat{U}_{\max}(s_0)$ be the real-valued random variable defined by

$$\widehat{U}_{\max}(s_0) = \max_{\nu \in \mathbb{B}_e} \|\mathbf{U}^{j_0}(2\pi\nu; s_0)\|, \quad (6.6)$$

depending on s_0 .

Let $\widehat{u}_{\max}(s_0)$ be the real number depending on s_0 such that $\text{Proba}\{\widehat{U}_{\max}(s_0) \leq \widehat{u}_{\max}(s_0)\} \leq 0.95$. Figure 6.3 displays function $s_0 \mapsto \widehat{u}_{\max}(s_0)$ computed with the stochastic models L-SROM and NL-SROM2 for $\delta_K = 0.1$ and for patterns \mathcal{P}_0 (tuned) and \mathcal{P}_6 (detuned). It can be seen that the propagation of uncertainties for the nonlinear geometric effects (NL-SROM2) is smaller than for the linear one (L-SROM). This attenuation is more important while s_0 is increasing, that is to say when the nonlinear effects increase.

Figures 6.4 to 6.9 display the graphs of the confidence region of $\nu \mapsto \|\widehat{U}^{j_0}(2\pi\nu)\|$ corresponding to a probability level 0.95 for both patterns \mathcal{P}_0 (tuned) and \mathcal{P}_6 (detuned) computed using NL-SROM2 for three external-forces intensities $s_0 = 0.01$, $s_0 = 0.15$, and $s_0 = 1$ corresponding to negligible, moderate, and strong geometric nonlinear effects. It can be seen that for $s_0 = 0.01$, the response in the frequency domain is clearly located in excitation frequency band \mathbb{B}_e , similarly to the linear case. For the medium and high values of s_0 , geometric nonlinear effects yield unexpected resonances that occur outside \mathbb{B}_e , especially, around 484 Hz (mode 1 defined in Section 4.5), which corresponds to the first bending mode of the blade and around 3700 Hz , which corresponds to a combination of elastic modes. In addition, the general level of responses outside band \mathbb{B}_e increases with s_0 . Concerning frequency band of excitation \mathbb{B}_e , it can be seen that the second bending mode of blade (mode 2 around 1170 Hz defined in Section 4.3) is relatively stable in amplitude with respect to s_0 while the first torsion mode of blade (mode 3 at around 1490 Hz defined in Section 4.3) tends to vanish when the nonlinear geometric effects increase. Furthermore, it can be noticed that the width of the confidence region is not constant with respect to the frequency.

We consider now that s_0 is fixed to the value 1. Let $B_L(2\pi\nu; \delta_K)$ be the random variable depending on δ_K , defined by Eq. (6.4), and constructed using the L-SROM. Let $B_L^\infty(\delta_K)$ be the random variable defined by

$$B_L^\infty(\delta_K) = \max_{\nu \in \mathbb{B}_e} B_L(2\pi\nu, \delta_K),$$

which corresponds to the maximum dynamic amplification factor over the excitation frequency band. We then denote by $b_L^{+, \infty}(\delta_K)$ the value of $B_L^\infty(\delta_K)$ depending on δ_K and such that

$$\text{Proba}\{B_L^\infty(\delta_K) \leq b_L^{+, \infty}(\delta_K)\} \leq 0.95.$$

Figure 6.10 displays the graph of function $\delta_K \mapsto b_L^{+, \infty}(\delta_K)$ for seven patterns of configurations: tuned pattern \mathcal{P}_0 and detuned ones $\mathcal{P}_2, \mathcal{P}_3, \mathcal{P}_5, \mathcal{P}_6, \mathcal{P}_{12}$, and \mathcal{P}_{31}

defined in Appendix B. The results obtained are coherent with those published in [3], especially, for each pattern, a maximum is obtained for a small mistuning (small value of δ_K).

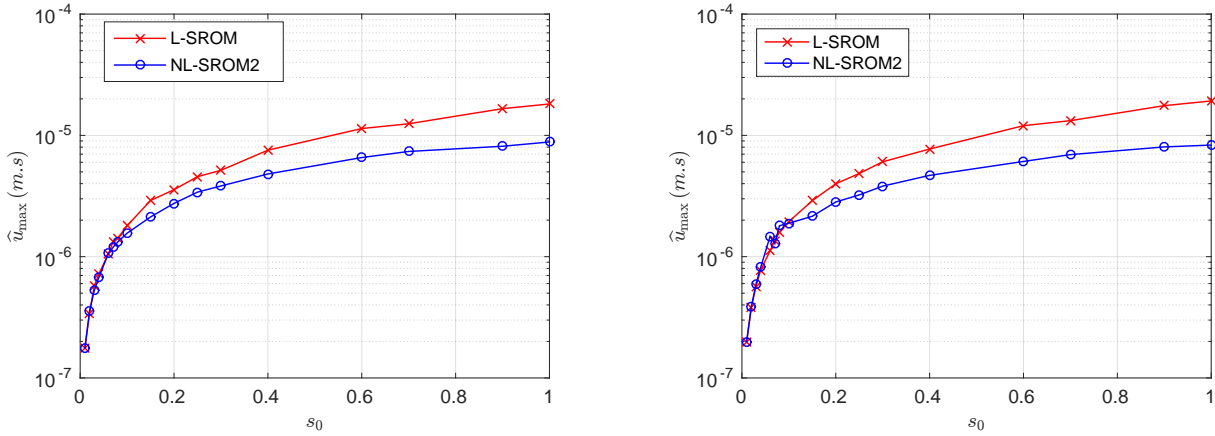


Figure 6.3 – For $\delta_K = 0.1$, graphs of function $s_0 \mapsto \hat{u}_{\max}(s_0)$ such that $\text{Proba}\{\hat{U}_{\max}(s_0) \leq \hat{u}_{\max}(s_0)\} \leq 0.95$ for the tuned rotating bladed-disk structure (pattern \mathcal{P}_0) and for the detuned pattern \mathcal{P}_6 . Calculation with L-SROM (red line with crosses) and with NL-SROM2 (blue line with circles).

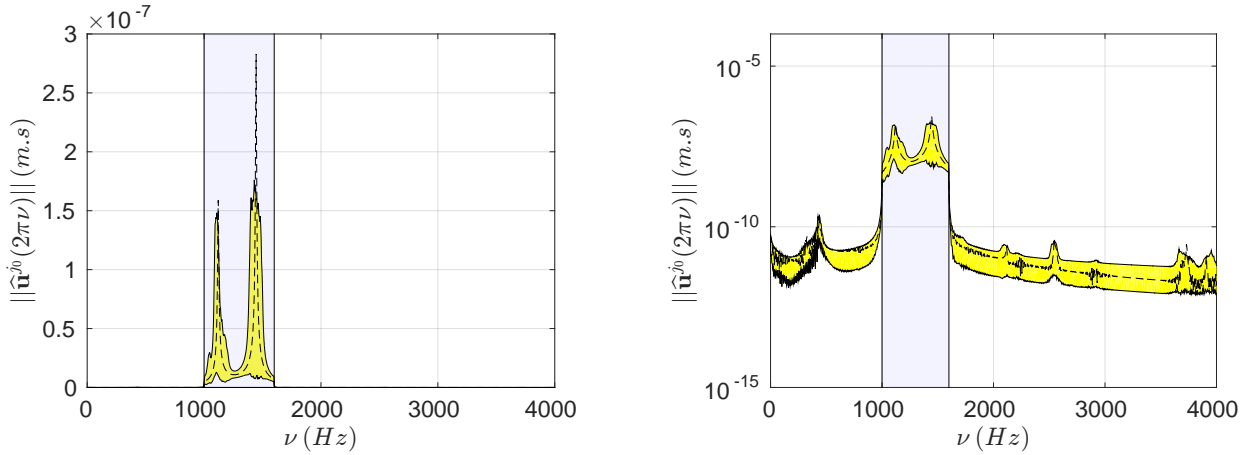


Figure 6.4 – For $\delta_K = 0.1$, confidence region (yellow region) of $\nu \mapsto \|\hat{\mathbf{U}}^{j_0}(2\pi\nu)\|$ corresponding to a probability level 0.95, computed using NL-SROM2 for the tuned rotating bladed-disk structure (pattern \mathcal{P}_0) and for $s_0 = 0.01$. The dashed-line is the response of the deterministic nominal (mean) model. The vertical grey region corresponds to excitation frequency band \mathbb{B}_e . Linear scale (left figure) and log scale (right figure)

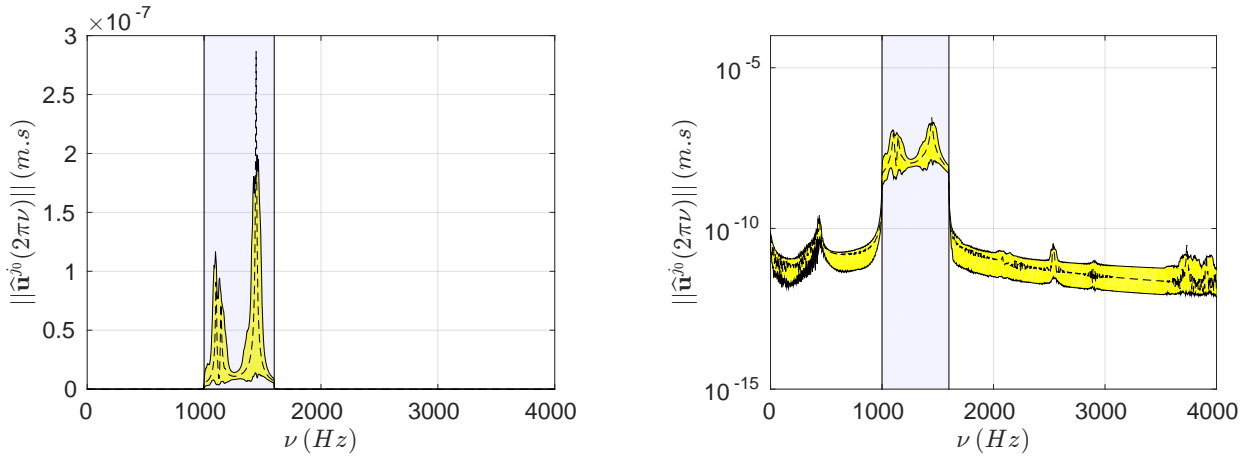


Figure 6.5 – For $\delta_K = 0.1$, confidence region (yellow region) of $\nu \mapsto \|\hat{\mathbf{U}}^{j_0}(2\pi\nu)\|$ corresponding to a probability level 0.95, computed using NL-SROM2 for the detuned pattern \mathcal{P}_6 and for $s_0 = 0.01$. The dashed-line is the response of the deterministic nominal (mean) model. The vertical grey region corresponds to excitation frequency band \mathbb{B}_e . Linear scale (left figure) and log scale (right figure)

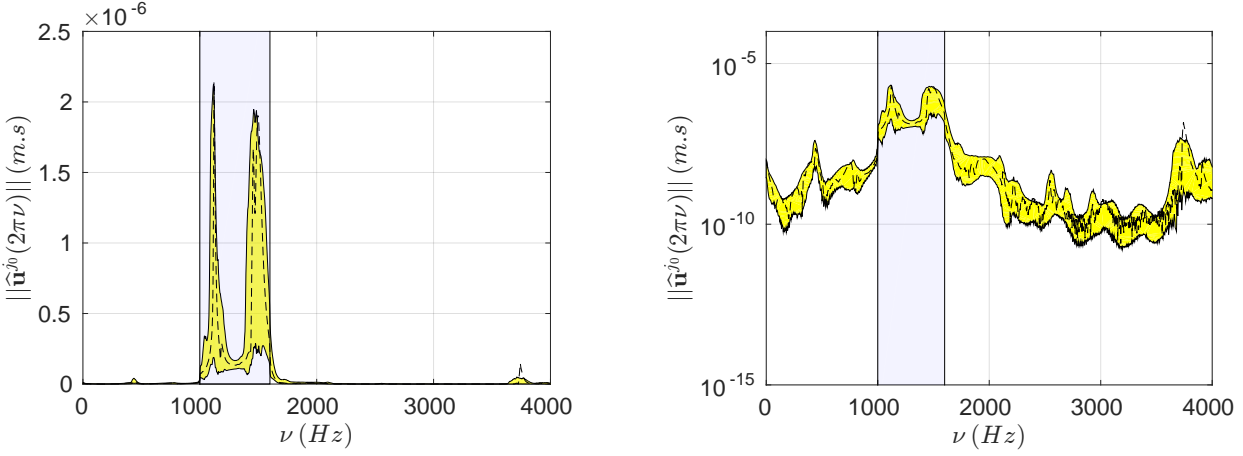


Figure 6.6 – For $s_0 = 0.15$ and for $\delta_K = 0.1$, confidence region (yellow region) of $\nu \mapsto \|\hat{\mathbf{U}}^{j_0}(2\pi\nu)\|$ corresponding to a probability level 0.95, computed using NL-SROM2 for the tuned rotating bladed-disk structure (pattern \mathcal{P}_0). The dashed-line is the response of the deterministic nominal (mean) model. The vertical grey region corresponds to excitation frequency band \mathbb{B}_e . Linear scale (left figure) and log scale (right figure)

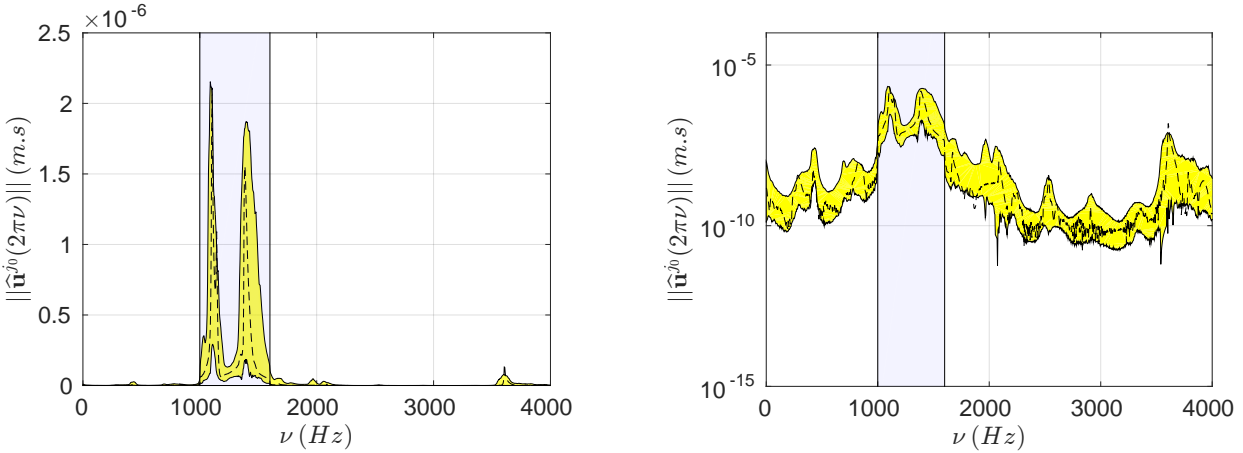


Figure 6.7 – For $s_0 = 0.15$ and for $\delta_K = 0.1$, confidence region (yellow region) of $\nu \mapsto \|\hat{\mathbf{U}}^{j_0}(2\pi\nu)\|$ corresponding to a probability level 0.95, computed using NL-SROM2 for detuned pattern \mathcal{P}_6 and for $s_0 = 0.15$. The dashed-line is the response of the deterministic nominal (mean) model. The vertical grey region corresponds to excitation frequency band \mathbb{B}_e . Linear scale (left figure) and log scale (right figure)

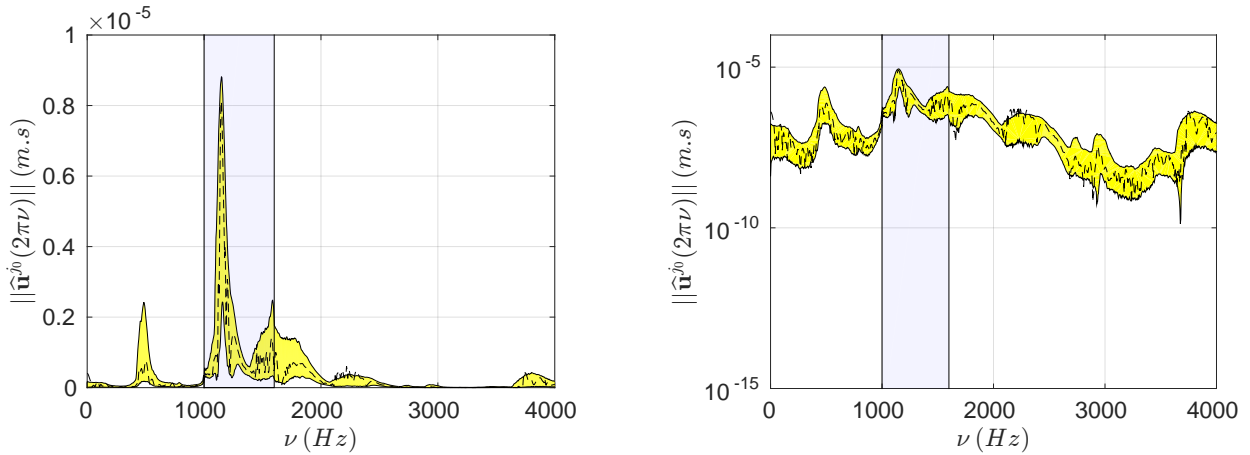


Figure 6.8 – For $s_0 = 1$ and for $\delta_K = 0.1$, confidence region (yellow region) of $\nu \mapsto \|\hat{\mathbf{U}}^{j_0}(2\pi\nu)\|$ corresponding to a probability level 0.95, computed using NL-SROM2 for the tuned rotating bladed-disk structure (pattern \mathcal{P}_0). The dashed-line is the response of the deterministic nominal (mean) model. The vertical grey region corresponds to excitation frequency band \mathbb{B}_e . Linear scale (left figure) and log scale (right figure)

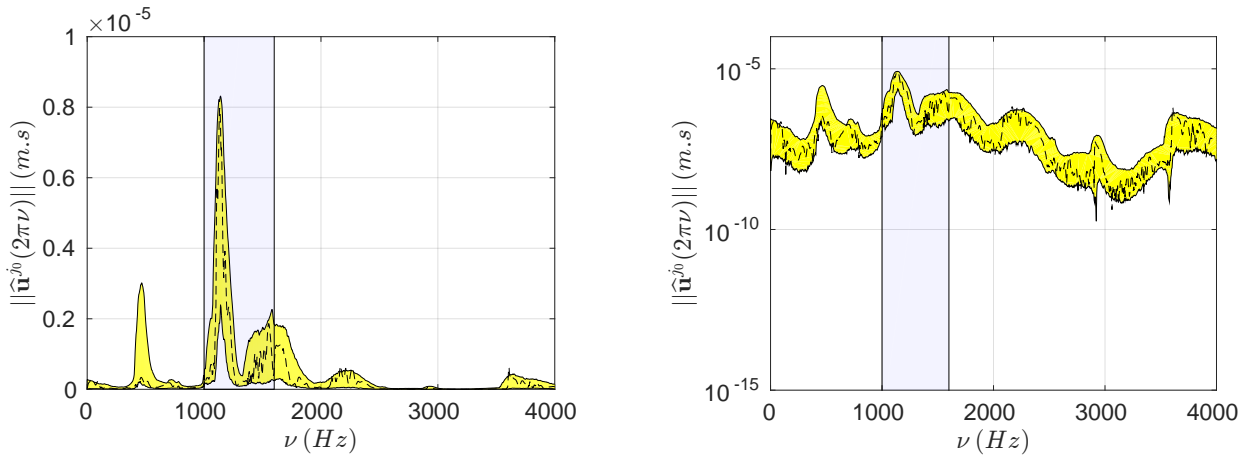


Figure 6.9 – For $s_0 = 1$ and for $\delta_K = 0.1$, confidence region (yellow region) of $\nu \mapsto \|\hat{\mathbf{U}}^{j_0}(2\pi\nu)\|$ corresponding to a probability level 0.95, computed using NL-SROM2 for detuned pattern \mathcal{P}_6 . The dashed-line is the response of the deterministic nominal (mean) model. The vertical grey region corresponds to excitation frequency band \mathbb{B}_e . Linear scale (left figure) and log scale (right figure)

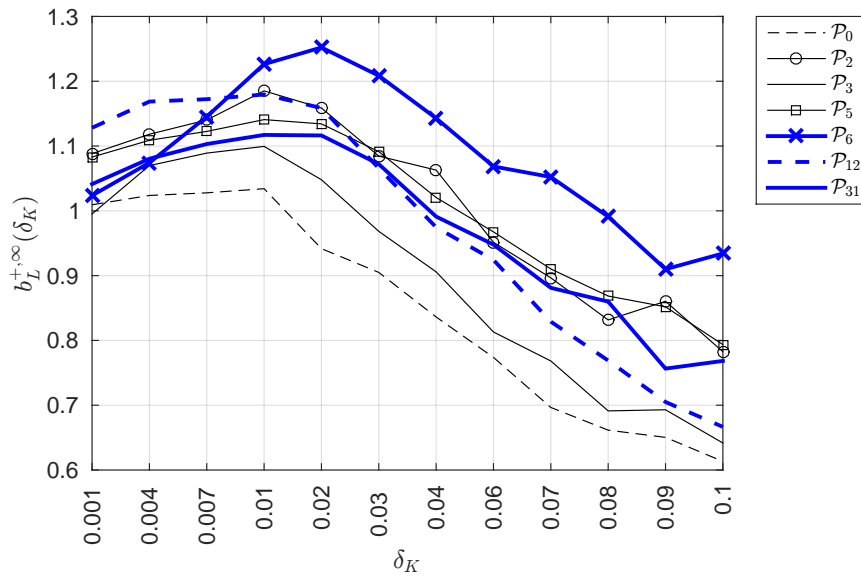


Figure 6.10 – For $s_0 = 1$, graphs of function $\delta_K \mapsto b_L^{+, \infty}(\delta_K)$ for tuned pattern \mathcal{P}_0 and detuned ones, \mathcal{P}_2 , \mathcal{P}_3 , \mathcal{P}_5 , \mathcal{P}_6 , \mathcal{P}_{12} , and \mathcal{P}_{31} defined in Appendix B.

6.3.3 Stochastic analysis of nonlinear rotating tuned and detuned bladed-disk structure in presence of mistuning for different patterns

In this section, we present the results obtained using NL-SROM1 for the nonlinear rotating tuned and detuned bladed-disks in presence of mistuning for which $s_0 = 1$.

Let $B_{\text{NL}}(2\pi\nu; \delta_K)$ be the random variable depending on δ_K , defined by Eq. (6.4), and constructed using the NL-SROM1. For two values of δ_K controlling the mistuning level, Figure 6.11 ($\delta_K = 0.03$) and Figure 6.12 ($\delta_K = 0.1$) display the confidence region of random variable $B_{\text{NL}}(2\pi\nu; \delta_K)$, estimated with a probability level of 0.95, for configurations \mathcal{P}_0 (tuned), and for \mathcal{P}_6 , \mathcal{P}_{11} , and \mathcal{P}_{25} (detuned defined in Appendix B). These figures allow for estimating the robustness of the responses with respect to the level of uncertainties as a function of the considered patterns. Nevertheless, the first torsion mode for $h = 4$ (mode 3 around 1490 Hz defined in Section 4.3) located in \mathbb{B}_e is very sensitive to the mistuning, as already mentioned for the linear case in Section 6.3.2. It can be seen that the nonlinear stochastic response of the mistuned-detuned bladed-disk is particularly complex. It should also be noted, as in Section 6.3.2, that unexpected resonances occur outside the excitation frequency band as soon as the level of nonlinearities is significant.

6.4 Discussion

It is interesting to observe that the results obtain using NL-SROM1 and NL-SROM2 yield different nonlinear dynamic behaviors. We recall that the main differences between these two stochastic computational models are that uncertainties do affect all the linear and nonlinear contributions in the NL-SROM1 case and only the linear elastic stiffness contribution in the NL-SROM2 case. One subsequent difference observed through the nonlinear computational analysis is that NL-SROM1 yields a robust behavior in the excitation frequency band that is not the case when considering NL-SROM2. Furthermore, it should be noted that the use of the NL-SROM1 with a Cholesky factorization for the global stiffness matrix yields (as shown in [35]) a similar nonrobust behavior. This is explained by the fact that in [35], uncertainties also did affect the other linear operators (mass, damping, ...), which is not the case here.

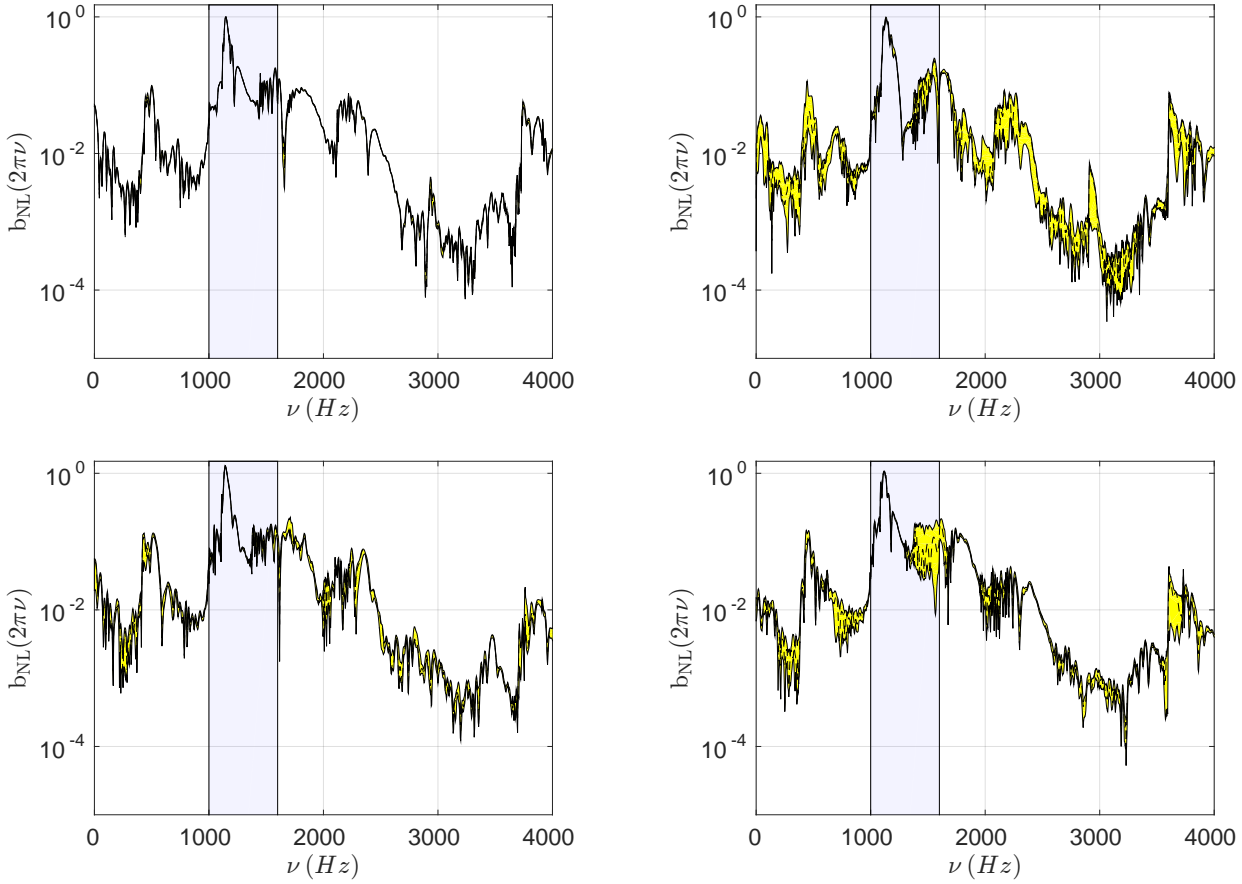


Figure 6.11 – For $s_0 = 1$ and for $\delta_K = 0.03$, confidence region (yellow region) of the random amplification factor, $B_{\text{NL}}(2\pi\nu)$, estimated with a probability level of 0.95 using NL-SROM1, for the tuned rotating bladed-disk structure (pattern \mathcal{P}_0) (left top figure), and for detuned patterns, \mathcal{P}_6 (right top), \mathcal{P}_{11} (left down), and \mathcal{P}_{25} (right down). The dashed-line is the nominal amplification factor $b_{\text{NL}}(2\pi\nu)$. The vertical grey region corresponds to excitation frequency band \mathbb{B}_e .

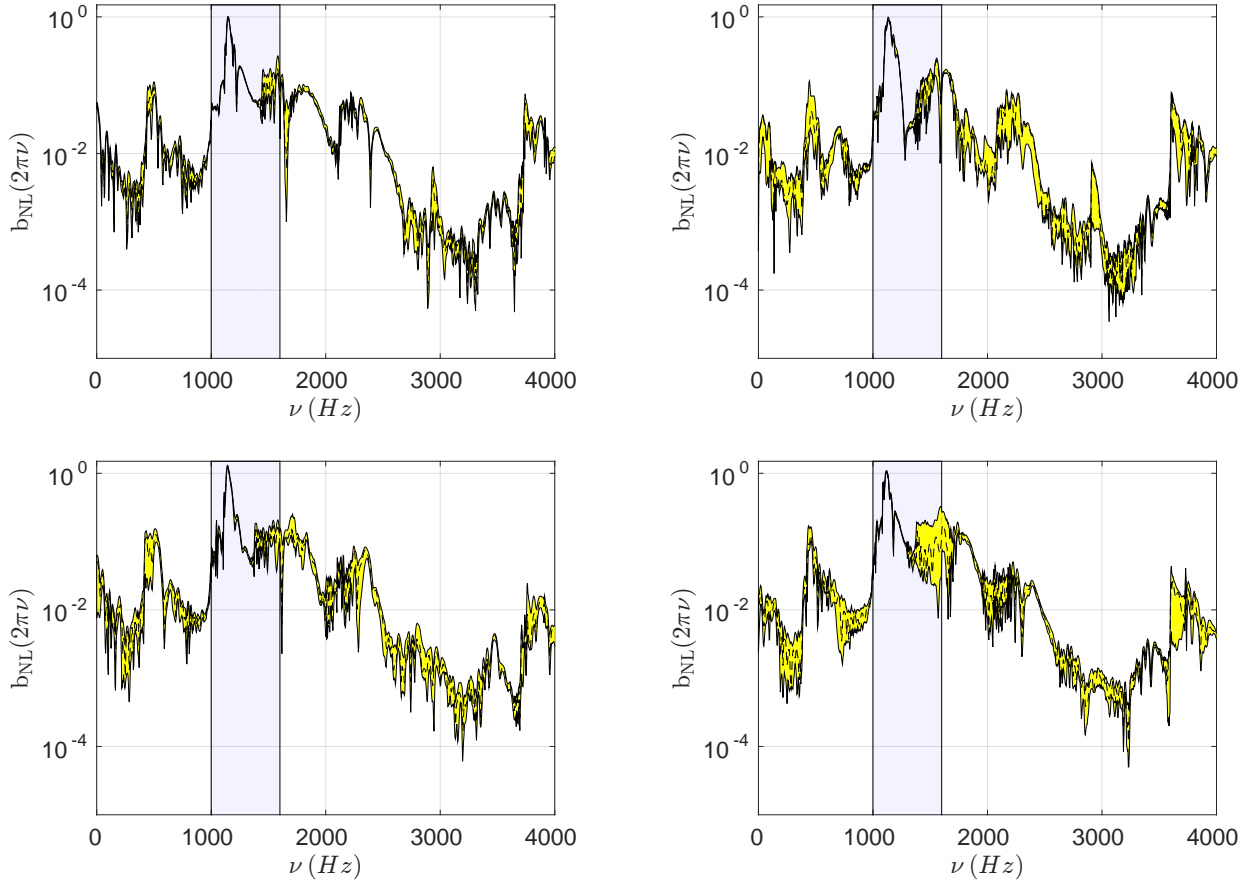


Figure 6.12 – For $s_0 = 1$ and for $\delta_K = 0.1$, confidence region (yellow region) of the random amplification factor, $B_{\text{NL}}(2\pi\nu)$, estimated with a probability level of 0.95 using NL-SROM1, for the tuned rotating bladed-disk structure (pattern \mathcal{P}_0) (left top figure), and for detuned patterns, \mathcal{P}_6 (right top), \mathcal{P}_{11} (left down), and \mathcal{P}_{25} (right down). The dashed-line is the nominal amplification factor $b_{\text{NL}}(2\pi\nu)$. The vertical grey region corresponds to excitation frequency band \mathbb{B}_e .

Chapter 7

Robust nonlinear computational dynamics of the mistuned-detuned bladed-disk structure

Contents

7.1	Introduction	75
7.2	Detuned bladed-disk structure without mistuning . . .	76
7.3	Stochastic analysis of nonlinear structures	76
7.4	Robust analysis with respect to sub-frequency bands .	79

7.1 Introduction

In Chapters 4 and 6, nonlinear dynamic analyses have been performed for three detuned patterns. In this Chapter, we are interested in the robust nonlinear dynamic analysis of rotating detuned bladed-disks in presence of mistuning with respect to a large family of patterns. Due to computation cost, only 46 patterns have been considered and are defined in Appendix B. This means that 46 nonlinear reduced-order models have been constructed. It should be noted that we mainly investigate the patterns involving three identical consecutive blades of type B . Since $M = 24$, it can be shown that there are 34 possible patterns, which are denoted by \mathcal{P}_i , $i = \{12, \dots, 45\}$. For instance, pattern $12B6A3B3A$ exhibits 12 consecutive blades of type B , 6 blades of type A , 3 blades of type B , and 3 blades of type A (note that patterns from \mathcal{P}_1 to \mathcal{P}_{11} are those already used in the previous

chapters).

7.2 Detuned bladed-disk structure without mistuning

In order to better understand the discrepancy of the detuned deterministic nonlinear dynamic responses with respect to the tuned ones, let $b_{\text{NL}}^{\pm}(2\pi\nu)$ be the upper (+) and the lower (−) envelopes of the dynamic amplification factors, defined over the family of patterns. Figure 7.1 displays the graphs of functions $\nu \mapsto b_{\text{NL}}^{\pm}(2\pi\nu)$ and $\nu \mapsto b_{\text{NL}}^{\text{tuned}}(2\pi\nu)$ performed with the NL-ROM for which $s_0 = 1$, that characterize the variability of the nonlinear dynamic behavior with respect to the family of patterns. It can be seen that the nonlinear dynamic response is very sensitive to the detuning, especially outside excitation frequency band \mathbb{B}_e . At a given frequency, the amplification factor can strongly differ from one pattern to another one.

7.3 Stochastic analysis of nonlinear rotating tuned and detuned bladed-disk structure in presence of mistuning

The analysis that we have presented in Section 6.3.3 is revisited considering all the 46 patterns defined in Appendix B. For simplifying the presentation of the results, the 46 patterns (the tuned pattern and the 45 detuned patterns, all in presence of mistuning) are considered as 46 realizations of a random mechanical system. Let $B_{\text{NL}}^{\text{all}}(2\pi\nu)$ be the random amplification factor defined by Eq. (6.4) of this random mechanical system, estimated using the NL-SROM1 with $\delta_K = 0.1$ and $s_0 = 1$. In practice, the confidence region associated with a probability level of 0.95 of random variable $B_{\text{NL}}^{\text{all}}(2\pi\nu)$ is estimated in concatenating all the Monte-Carlo realizations computed for each one of the 46 patterns. Figure 7.2 displays (in linear and log scales) the confidence region of the deterministic amplification factor $b_{\text{NL}}^{\text{tuned}}(2\pi\nu)$ for the rotating tuned bladed-disk without mistuning and the random variable $B_{\text{NL}}^{\text{all}}(2\pi\nu)$ for all the 46 detuned patterns with mistuning, which includes, as previously mentioned, the tuned pattern \mathcal{P}_0 in presence of mistuning. We use the same type of analysis as the one presented in Section 6.3.3. This figure shows that the random amplification factor is high outside excitation frequency band \mathbb{B}_e

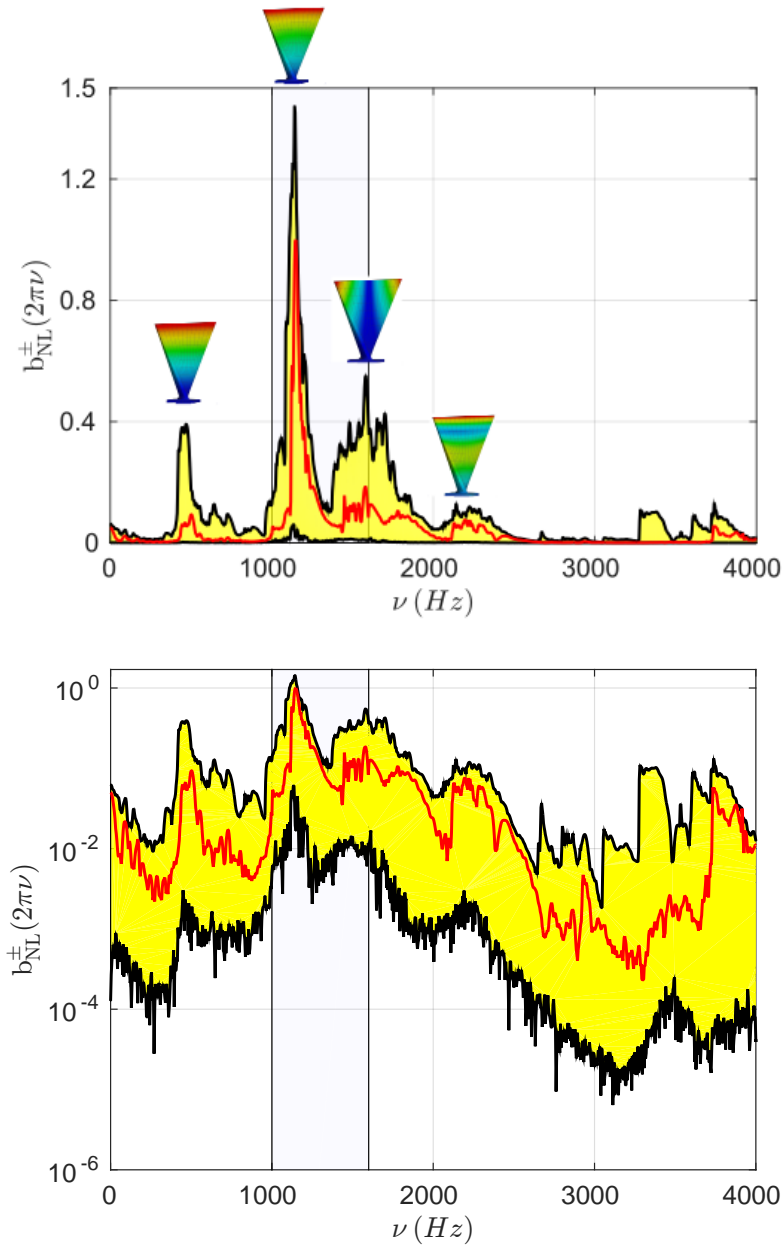


Figure 7.1 – For $s_0 = 1$, graphs of functions $\nu \mapsto b_{\text{NL}}^{\pm}(2\pi\nu)$ (black irregular thick lines) and $\nu \mapsto b_{\text{NL}}^{\text{tuned}}(2\pi\nu)$ (red irregular thin line) corresponding to the upper (+) and the lower (–) envelopes of the dynamic amplification factor among the investigated patterns. Linear scale (top figure) and log scale (down figure)

and is sensitive to uncertainties. It should be noted that $b_{\text{NL}}^{\text{tuned}}(2\pi\nu)$ belongs to the confidence region.

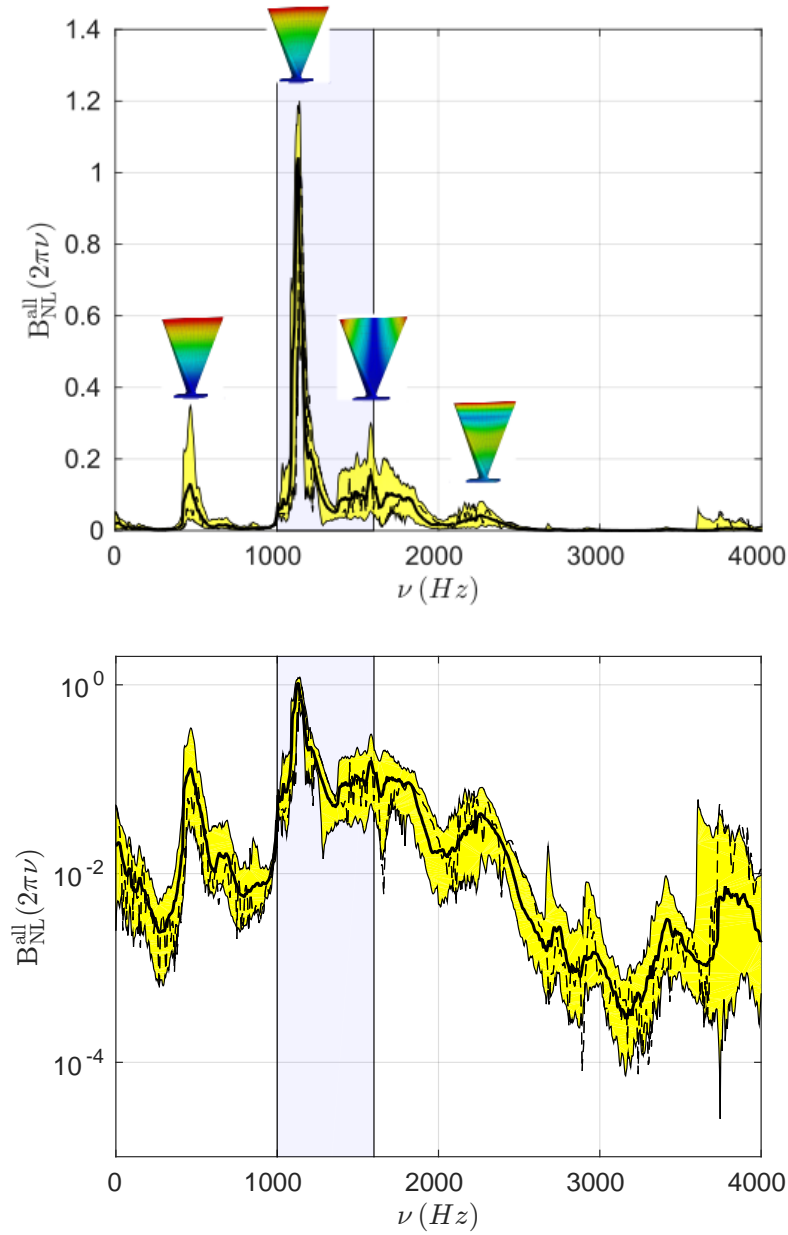


Figure 7.2 – For $\delta_K = 0.1$ and $s_0 = 1$, confidence region (yellow/grey region) of the random amplification factor, $B_{NL}^{all}(2\pi\nu)$, related to the 46 patterns, estimated with a probability level of 0.95 using NL-SROM1. The dashed-line is the amplification factor $b_{NL}^{tuned}(2\pi\nu)$ of the tuned system without mistuning. The thick solid line is the median value of random variable $B_{NL}^{all}(2\pi\nu)$. The vertical grey region corresponds to excitation frequency band \mathbb{B}_e . Linear scale (top figure), log scale (down figure)

Moreover, the analysis of Figure 7.2 shows that the robustness of the stochastic response around the two main resonances, located in band \mathbb{B}_e , is significantly higher than outside \mathbb{B}_e , while there are relatively of high levels outside \mathbb{B}_e (in the linear case, there is no response outside the band \mathbb{B}_e). In the low-frequency band $[0, 1\,000] Hz$ (not excited by the external forces), there are mistuned configurations for which the amplitude level outside \mathbb{B}_e is four times lower than the one in \mathbb{B}_e . Nevertheless, it should be noted that the levels of responses (induced by the nonlinear geometric effects), which occur outside band \mathbb{B}_e , depend on the pattern.

7.4 Robust analysis with respect to sub-frequency bands

The results presented in Section 7.3 lead us to split the frequency band of analysis \mathbb{B}_a in 3 sub-frequency bands to better analyze the amplification factor. We then define the following bands: $\mathbb{B}_{\text{low}} = [0, 1\,000] Hz$, $\mathbb{B}_{\text{med}} = [1\,000, 1\,300] Hz$, and $\mathbb{B}_{\text{high}} = [1\,300, 4\,000] Hz$. Note that band \mathbb{B}_{med} is included in frequency band of excitation \mathbb{B}_e and that band \mathbb{B}_{high} overlaps band \mathbb{B}_e with the common frequency band $[1\,300, 1\,600] Hz$. This partition of the frequency band of analysis has been introduced in order to analyze the amplification of the resonances in each sub-frequency band. Let $\{\text{low}, \text{med}, \text{high}\}$ be the set of the three identifiers such that, for "band" $\in \{\text{low}, \text{med}, \text{high}\}$, the band \mathbb{B}_{band} denotes one of the band \mathbb{B}_{low} , \mathbb{B}_{med} , and \mathbb{B}_{high} .

For $s_0 = 1$, let $B_{\text{NL}}(2\pi\nu; \delta_K)$ be the random amplification factor defined by Eq. (6.4), computed using NL-SROM1 and let

$$B_{\text{NL}}^{\infty, \text{band}}(\delta_K) = \max_{\nu \in \mathbb{B}_{\text{band}}} B_{\text{NL}}(2\pi\nu; \delta_K) \quad (7.1)$$

be the random variable that corresponds to the maximum dynamic amplification factor over frequency band \mathbb{B}_{band} . We then denote by $b_{\text{NL}}^{+, \infty, \text{band}}(\delta_K)$ the value of $B_{\text{NL}}^{\infty, \text{band}}(\delta_K)$ depending on δ_K and such that

$$\text{Proba}\{B_{\text{NL}}^{\infty, \text{band}}(\delta_K) \leq b_{\text{NL}}^{+, \infty, \text{band}}(\delta_K)\} \leq 0.95. \quad (7.2)$$

For anyone of the 46 patterns, we are interested in plotting the graphs of functions $\delta_K \mapsto b_{\text{NL}}^{+, \infty, \text{low}}(\delta_K)$, $\delta_K \mapsto b_{\text{NL}}^{+, \infty, \text{med}}(\delta_K)$, and $\delta_K \mapsto b_{\text{NL}}^{+, \infty, \text{high}}(\delta_K)$, which describe the evolution of the maximum amplification factor for each pattern according to the dispersion parameter δ_K . However, to maintain a sufficient readability of the

figures, we only plot the lower and the upper envelopes of the 46 patterns. These two envelopes define a region in which all the 46 patterns belong.

Figures 7.4 to 7.5 show the graphs for each frequency band, \mathbb{B}_{med} , \mathbb{B}_{low} , and \mathbb{B}_{high} . In the caption of each one of these three figures, the patterns corresponding to the lower and the upper envelopes are indicated. Figure 7.3 shows that there is a weak sensitivity of the envelopes with respect to the mistuning level represented by the value of δ_K . Pattern \mathcal{P}_{34} , which corresponds to the upper envelope, yields the largest dynamic amplification factor in band \mathbb{B}_{med} , whereas pattern \mathcal{P}_1 , which corresponds to the lower envelope, has the lowest dynamic amplification factor. In Figures 7.4 and 7.5, it can be seen that the envelopes are sensitive to the level of mistuning represented by δ_K , and that a very high dynamic amplification factor can be obtained, that is the case for pattern \mathcal{P}_{26} (upper envelope for \mathbb{B}_{low}) and for pattern \mathcal{P}_9 (upper envelope for \mathbb{B}_{high}). Note that these dynamic amplification factor is normalized with respect to the nonlinear tuned response without mistuning and could not be normalized with respect to the linear tuned system, which would yield an infinite value.

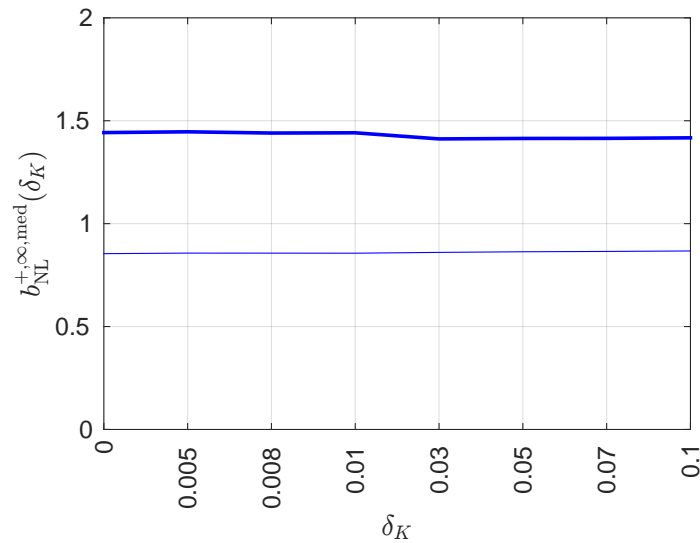


Figure 7.3 – For $s_0 = 1$ and for band \mathbb{B}_{med} , lower (thin solid line) and upper (thick solid line) envelopes of the regions containing the 46 graphs of functions $\delta_K \mapsto b_{\text{NL}}^{+, \infty, \text{med}}(\delta_K)$ for the 46 patterns using NLSROM1. The upper envelope corresponds to detuned pattern \mathcal{P}_{33} and the lower one to detuned pattern \mathcal{P}_1 .

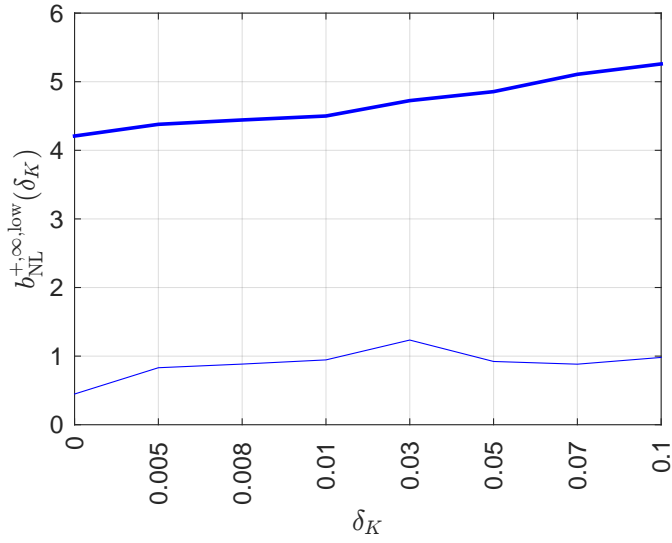


Figure 7.4 – For $s_0 = 1$ and for band \mathbb{B}_{low} , lower (thin solid line) and upper (thick solid line) envelopes of the regions containing the 46 graphs of functions $\delta_K \mapsto b_{\text{NL}}^{+, \infty, \text{low}}(\delta_K)$ for the 46 patterns using NLSROM1. The upper envelope corresponds to detuned pattern \mathcal{P}_{26} and the lower one to detuned pattern \mathcal{P}_{37} .

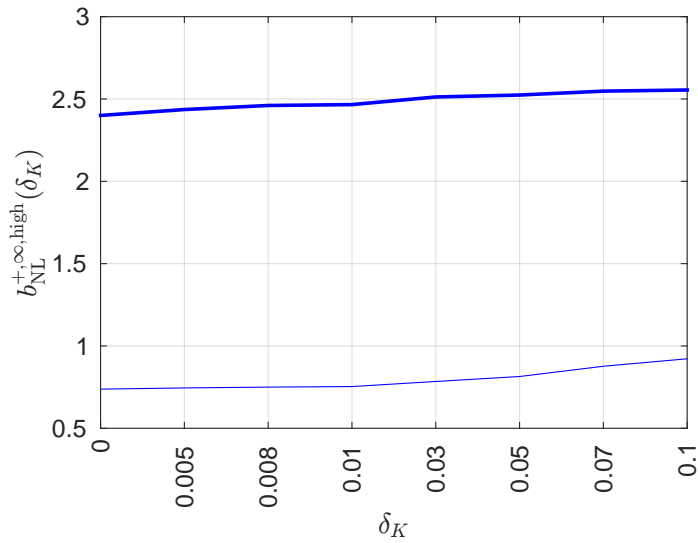


Figure 7.5 – For $s_0 = 1$ and for band \mathbb{B}_{high} , lower (thin solid line) and upper (thick solid line) envelopes of the regions containing the 46 graphs of functions $\delta_K \mapsto b_{\text{NL}}^{+, \infty, \text{high}}(\delta_K)$ for the 46 patterns using NLSROM1. The upper envelope corresponds to detuned pattern \mathcal{P}_9 and the lower one to \mathcal{P}_8 .

Chapter 8

Quantitative nonlinear analysis in terms of modal participation

Contents

8.1	Introduction	83
8.2	Nonlinear deterministic analyses related to modes 2B and 1T	84
8.3	Stochastic nonlinear analyses of modes 2B and 1T	84
8.4	Quantification concerning the energy transfer according to the modal excitation	86

8.1 Introduction

Until now, the external loading has been characterized with a circumferential wave number $h = 4$ (nodal diameter) with an excitation frequency band \mathbb{B}_e chosen as $\mathbb{B}_e = [1\,000, 1\,600]Hz$. Such excitation frequency band \mathbb{B}_e contains the two eigenfrequencies corresponding to the second bending mode of the blade (2B) and the first torsional mode of the blade (1T). Furthermore, the results presented in Chapter 7 for the rotating tuned and detuned bladed-disk structures with and without mistuning, have shown that the mode 1T vanishes and is sensitive to uncertainties, whereas the mode 2B does not vanish remaining robust, as shown in Figure 7.2. Here, we propose a partial analysis limited to a detailed nonlinear analysis for the tuned pattern \mathcal{P}_0 with and without mistuning, in order to better

understand the modal participation of modes 2B and 1T. Certainly, such a limited analysis should be extended to the analysis of detuned patterns.

8.2 Nonlinear deterministic analyses related to modes 2B and 1T

In this Section, the two modes of interest (2B at 1170 Hz and 1T at 1490 Hz belonging to the excitation frequency band as shown in Figure 7.2) are individually excited using the L-ROM and the NL-ROM in order to understand why the first torsion mode vanishes (1T) whereas the second bending (2B) mode does not. We proceed to two distinct analyses that differ from one to another one by the excitation frequency band characterized by function $g(t)$. Let $\mathbb{B}_e^{2B} = [1\,000, 1\,300]Hz$ and $\mathbb{B}_e^{1T} = [1\,300, 1\,600]Hz$ be the excitation frequency bands, which respectively contain the eigenfrequencies $\nu^{(2B)} = 1\,130 Hz$ and $\nu^{(1T)} = 1\,483 Hz$. Since the excitation is chosen with a circumferential wave number $h = 4$, it ensures that only one mode is excited when dealing with a linear operating regime. The intensity of the load is taken as $s_0 = 1$, which means that there are significant geometric nonlinear effects as shown in 4.4.5. Figures 8.1 displays the graphs of function $\nu \mapsto \|\widehat{\mathbf{u}}^{j_0}(2\pi\nu)\|$ for these two linear and nonlinear computations. There are subsequent geometric nonlinear effects. The modal resonances are shifted to the right and its amplitude is reduced. In particular, for the present case, the torsional contribution drastically vanishes (10 times lower) comparing to the bending contribution that vanishes (2 times lower).

8.3 Stochastic nonlinear analyses of modes 2B and 1T

The stochastic nonlinear analyses are carried out with a mistuning level corresponding to $\delta_K = 0.1$ and for $s_0 = 1$. Figure 8.2 displays the graph of confidence region of $\nu \mapsto \|\widehat{\mathbf{U}}^{j_0}(2\pi\nu)\|$ corresponding to a probability level 0.95. It can be clearly seen that the mode 2B is robust with respect to uncertainties, whereas mode 1T is sensitive. In particular, the sensitivity of the response in the higher frequencies above the excitation frequency band is almost entirely due to the excitation of the torsional mode, taking into account the response shown in Figure 7.2.

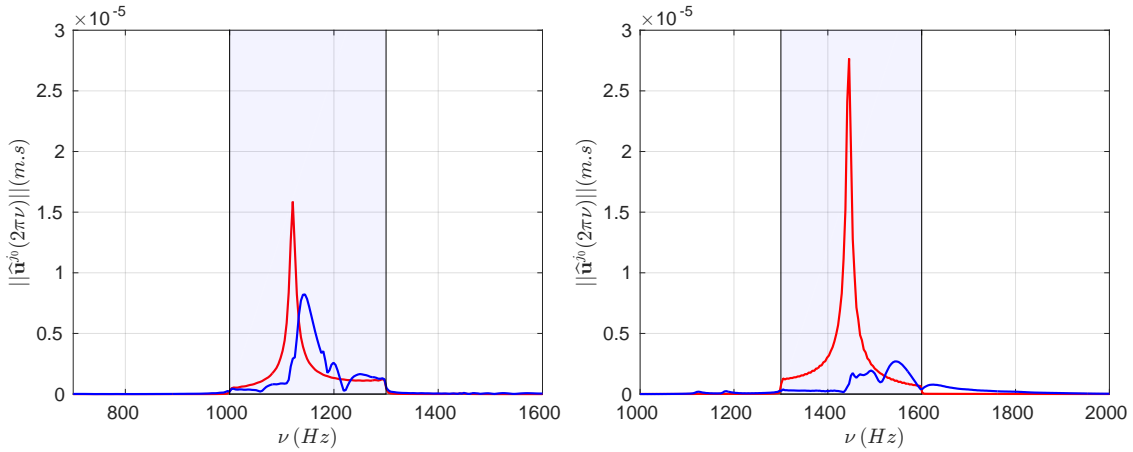


Figure 8.1 – For $s_0 = 1$, frequency analysis of the time responses related to mode 1B (left figure) and mode 1T (right figure). In each figure, the computation with the L-ROM is in red color and with the NL-ROM in blue color: graph of function $\nu \mapsto \|\widehat{\mathbf{u}}^{j_0}(2\pi\nu)\|$ for the tuned rotating bladed-disk structure (pattern \mathcal{P}_0). The excitation frequency band \mathbb{B}_e is in light grey area.

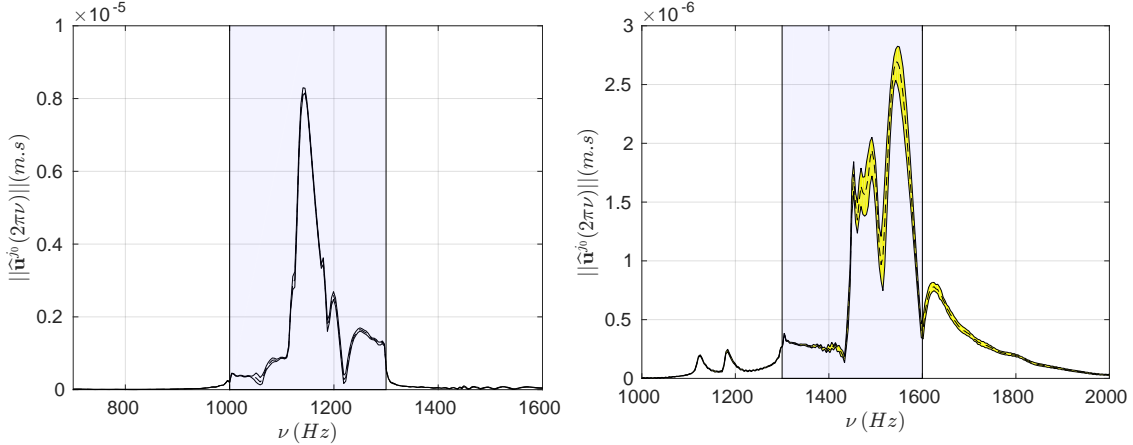


Figure 8.2 – For $s_0 = 1$ and for $\delta_K = 0.1$, confidence region (yellow/grey region) of $\nu \mapsto \|\widehat{\mathbf{U}}^{j_0}(2\pi\nu)\|$ corresponding to a probability level 0.95, computed using NL-SROM1 for the tuned rotating bladed-disk structure (pattern \mathcal{P}_0) related to mode 2B (left figure) and mode 1T (right figure). The dashed-line is the response of the deterministic mean (nominal) model. The vertical grey region corresponds to excitation frequency band \mathbb{B}_e

8.4 Quantification concerning the energy transfer according to the modal excitation

In section 8.2, modes 2B and 1T have been individually excited in order to understand how these modes are modified by the geometric nonlinearity effects. In this section, we investigate the energy transfer between modes. We have limited the investigations to pattern \mathcal{P}_0 with an excitation for which the circumferential wave number is $h = 4$. First we quantify the evolution of the modal contents as a function of rotation speed Ω as follows. Let $\mathcal{R}_{\nu_\alpha}(\Omega)$ be the quantity defined by

$$\mathcal{R}_{\nu_\alpha}(\Omega) = \frac{\nu_\alpha(\Omega)}{\nu^{(1B)}(\Omega)}, \quad (8.1)$$

in which $\nu_\alpha(\Omega)$ is any eigenfrequency of the rotating tuned bladed-disk for $h = 4$ and $\nu^{(1B)}(\Omega)$ is its counterpart for mode 1B. Figure 8.3 displays the graph $\Omega \mapsto \mathcal{R}_{\nu_\alpha}(\Omega)$ for α corresponding to the modes 1B, 2B, 1T, and 3B. A parametric non-

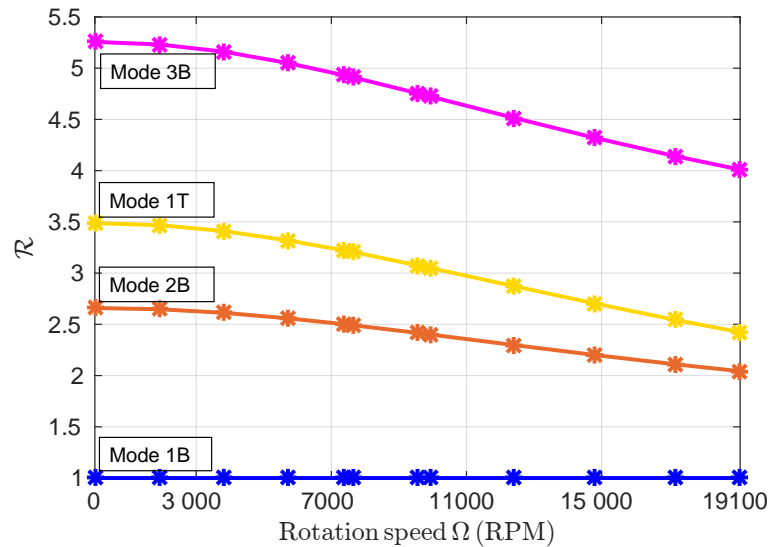


Figure 8.3 – Graph of the evolution of the ratio $\mathcal{R}(\nu_\alpha)$ with respect to the rotation speed Ω .

linear analysis is then carried out with respect to the rotation speed Ω . We want to quantify the energy transfer with respect to the value of $\mathcal{R}_{\nu_\alpha}(\Omega)$.

8.4. Quantification concerning the energy transfer according to the modal excitation

A first nonlinear dynamic analysis without mistuning is conducted as follows. The excitation frequency band is defined as $\mathbb{B}_e^{1B} = [350, 550] Hz$, which contains $\nu^{(1B)} = 425.1 Hz$ for a rotation speed $\Omega = 4440$ RPM. We consider several rotation speeds $\Omega = 19098, 17188,$ and 7352 RPM yielding $\mathcal{R}_{\nu_\alpha}(\Omega) = 2.0, 2.1,$ and 2.5 for ν_α corresponding to mode 2B. Four values of s_0 are considered, $s_0 = 0.05, s_0 = 0.3, s_0 = 0.7,$ and $s_0 = 1$. Figures 8.4 and 8.5 display function $\nu \mapsto \|\widehat{\mathbf{u}}^{j_0}(2\pi\nu)\|$ for all these cases. It is clearly seen that the mode 2B corresponding to eigenfrequency $\nu^{(2B)} = 1130 Hz$ ($\Omega = 4440$ RPM) does not seem excited through geometric nonlinearities, which is not the case when observing resonances around $1500 Hz$ to mode 1T. It is interesting to observe that, the third bending mode (3B) related to eigenfrequency $\nu^{(3B)} = 2234 Hz$ ($\Omega = 4440$ RPM) yields a maximal contribution for a ratio $\mathcal{R}_{\nu_\alpha}(\Omega) = 2.5$. Again, we observe that all the modes located in the excitation frequency bands are excited as expected through the geometric nonlinearities.

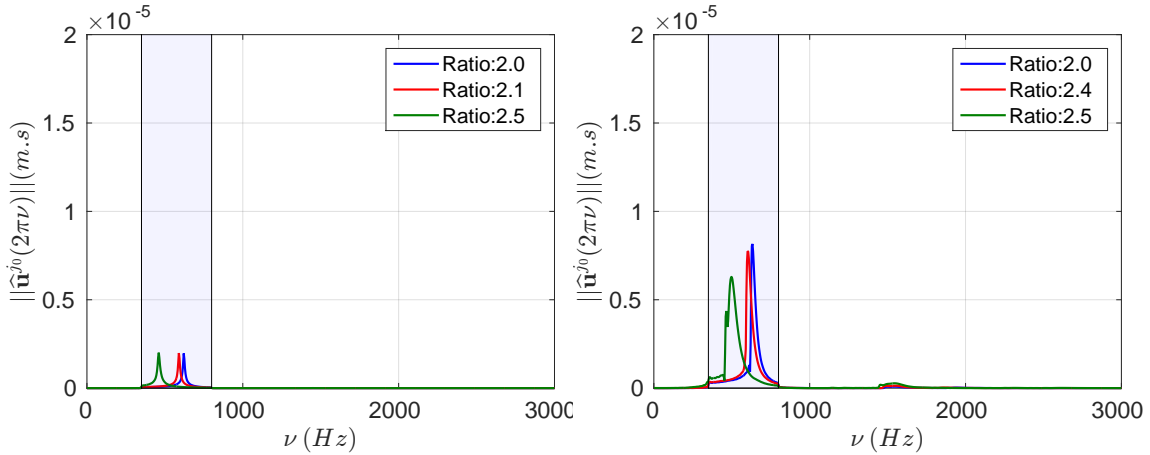


Figure 8.4 – Graphs of function $\nu \mapsto \|\widehat{\mathbf{u}}^{j_0}(2\pi\nu)\|$ for $s_0 = 0.05$ (left figure) and $s_0 = 0.3$ (right figure). The light blue zone corresponds to the excitation frequency band \mathbb{B}_e

A second nonlinear dynamic analysis is conducted as the first one but for another excitation frequency band that is $\mathbb{B}_e = [1000, 1400] Hz$, which contains the mode 2B corresponding to eigenfrequency $\nu^{(2B)} = 1130 Hz$ ($\Omega = 4440$ RPM). Figures 8.6 and 8.7 display function $\nu \mapsto \|\widehat{\mathbf{u}}^{j_0}(2\pi\nu)\|$ for four load intensities and three values of $\mathcal{R}_{\nu_\alpha}(\Omega)$. It can be seen that a small quantity of vibrational energy is transferred to mode 1B (around $500 Hz$) whereas the energy transfer from mode 2B to mode 1T is more important.

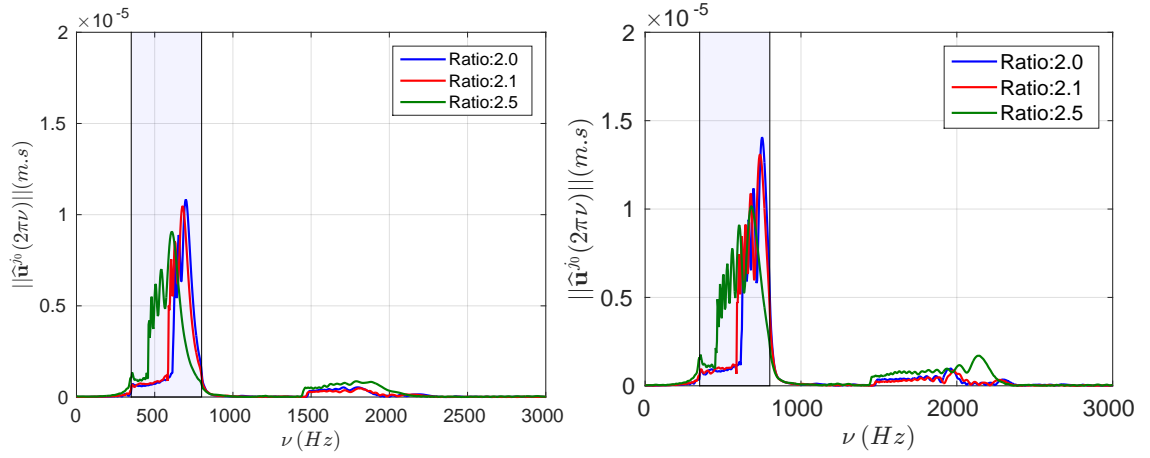


Figure 8.5 – Graphs of function $\nu \mapsto \|\hat{\mathbf{u}}^{j_0}(2\pi\nu)\|$ for $s_0 = 0.7$ (left figure) and $s_0 = 1$ (right figure). The light blue zone corresponds to the excitation frequency band \mathbb{B}_e

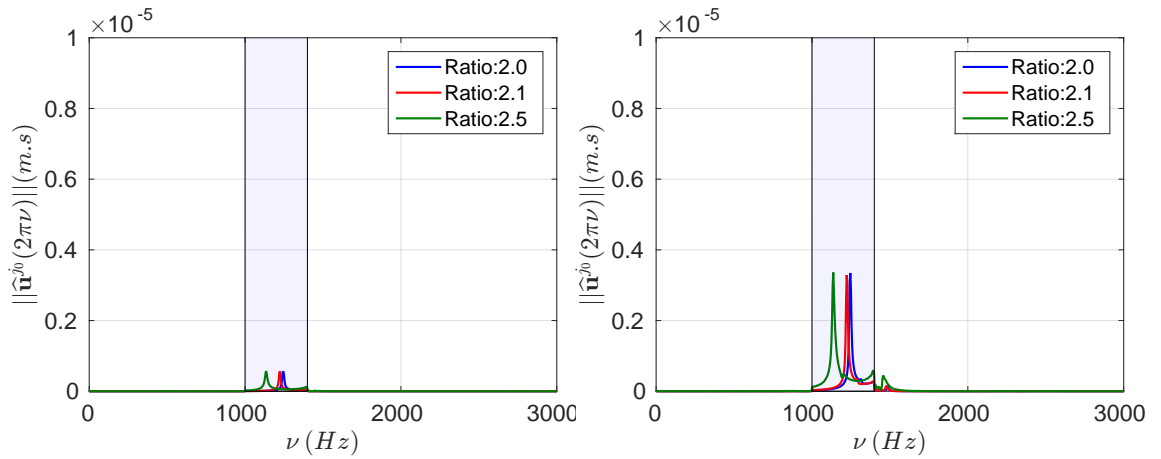


Figure 8.6 – Graphs of function $\nu \mapsto \|\hat{\mathbf{u}}^{j_0}(2\pi\nu)\|$ for $s_0 = 0.05$ (left figure) and $s_0 = 0.3$ (right figure). The light blue zone corresponds to the excitation frequency band \mathbb{B}_e

8.4. Quantification concerning the energy transfer according to the modal excitation

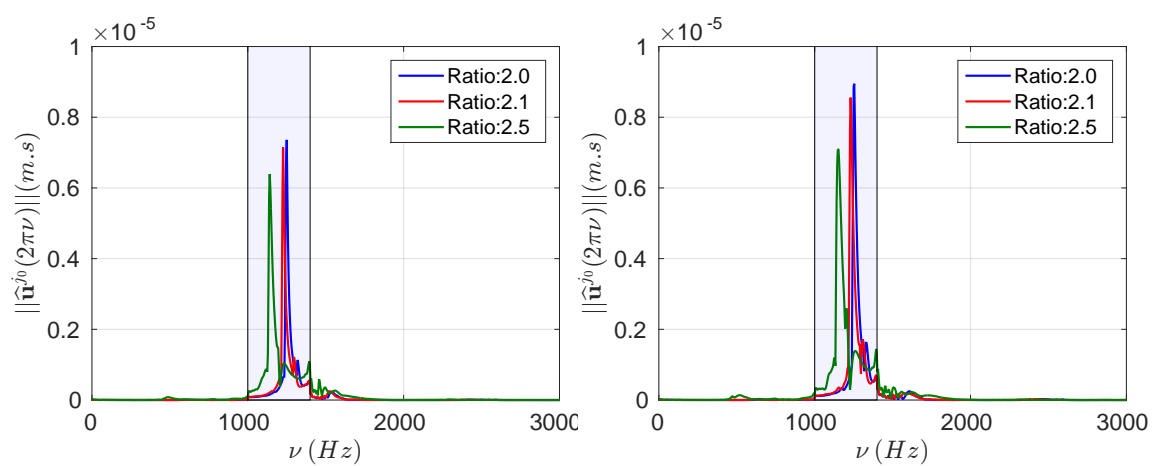


Figure 8.7 – Graphs of function $\nu \mapsto \|\hat{\mathbf{u}}^{j_0}(2\pi\nu)\|$ for $s_0 = 0.7$ (left figure) and $s_0 = 1$ (right figure). The light blue zone corresponds to the excitation frequency band \mathbb{B}_e

Conclusion and Perspectives

Summary

This thesis has proposed a robust analysis of rotating mistuned-detuned bladed disk structures in order to understand the amplification effects induced by the mistuning phenomenon in presence of nonlinear geometric effects. A complete methodology has been proposed for constructing a nonlinear stochastic reduced-order model (NL-SROM). A main contribution concerns the methodology proposed for constructing a *reduced-order basis* used for obtaining the NL-ROM and then the NL-SROM. More precisely, a *modal basis* has been computed by solving the generalized eigenvalue problem associated with the nonlinear high-fidelity model (NL-HFM), without nonlinear geometrical effects, without damping, and without mistuning. A first nonlinear reduced-order model has been obtained by projecting the nonlinear NL-HFM on the subspace spanned by this modal basis for which the convergence has carefully been studied. Then, another *vector basis* has been calculated using the Proper-Orthogonal Decomposition (POD) method applied to the nonlinear solution of the first nonlinear reduce-order model, which has been solved in the time domain. Finally, a *projection basis* for the NL-HFM has been obtained by composing the modal basis with the vector basis constructed with the POD method. The final nonlinear reduced-order model has then been obtained by projecting the NL-HFM on the subspace spanned by the projection basis introduced above. A careful attention has been done to take into account the random character of the mistuning phenomena that we have modeled with the nonparametric probabilistic approach of uncertainties. The nonlinear dynamic analyses have been carried out in the time domain and its Fourier Transform has allowed *a posteriori* frequency analysis to be conducted. A comparison has led us to conclude that the geometrical nonlinearities propagate the energy of the excitation outside the frequency band of excitation, yielding unexpected resonances that could be potentially dangerous. It is well known that the interest of the detuning

is to reduce for the best all the dynamic amplification induced by the mistuning. The corresponding nonlinear analysis is more complex because different dynamic behaviours occur according to different sub-frequency bands of analysis. Finally, a robust analysis of the effects of geometric nonlinearities on the nonlinear dynamic behavior of rotating bladed-disks structures that are detuned in presence of mistuning, has been presented. To this end, 46 patterns have been investigated, which have shown the variability of the amplification factor over a family of patterns. In the low-frequency band, which is not excited by the external forces, there are detuned configurations whose local amplification level can vary with a factor 4. In the excitation frequency band, the local variability of the dynamic amplification factor has been found to be lower compared to those obtained outside the excitation frequency band. Nevertheless, although a nonexhaustive study optimization could not be made, it has been shown that there were detuned configurations that minimize the dynamic amplification factor in presence of mistuning.

Perspectives

The results obtained allow for increasing the knowledge in the area of the nonlinear stochastic dynamics of the rotating detuned bladed disk structures in presence of mistuning. The envelopes of the dynamic amplifications factors among the investigated patterns show that the nonlinear dynamic response is sensitive to the detuning in presence of mistuning. A first additional work would consist in taking into account the aerodynamic couplings. A second perspective could be related to the optimization of the patterns. Indeed, the optimization with respect to all the possible configurations defined by the patterns, with the objective to find the pattern that minimizes the random dynamic amplification factor, remains a problem that demands large computer resources in term of CPU time. The complexity of the results obtained for the 46 configurations studied, seems to show that such a discrete nonconvex optimization problem on a set of configurations having a huge number of patterns, is difficult. Certainly, new algorithms based on machine learning should help to solve this difficult optimization problem.

Appendix A

Construction of the geometric stiffness matrix

We reuse the notations introduced in Chapter 2. The objective of this Appendix is to briefly explain how is calculated the geometric stiffness matrix $[K_g(\Omega)]$, which results from the finite element discretization of the linear form

$$l_c(\mathbf{v}) = \int_{\mathcal{D}} \rho [R(\Omega)]^2 x_i \mathbf{e}_i \cdot \mathbf{v} d\mathbf{x} \quad . \quad (\text{A.1})$$

Let \mathbf{F}_c be the vector of \mathbb{R}^n of the finite element discretization of the centrifugal forces in the computational model, applied in the rotating frame, for the rotating bladed-disk structure. The geometric stiffness matrix $[K_g(\Omega)]$ is constructed from the corresponding stress state. The following static problem is solved:

$$[K_e] \mathbf{U}^{\text{geom}} = \mathbf{F}_c \quad (\text{A.2})$$

The computation of the static response \mathbf{U}^{geom} allows the corresponding stress tensor $\boldsymbol{\sigma}^{\text{geom}}$ to be constructed at any integration point of the finite element mesh.

Let $k_g(\mathbf{u}, \mathbf{v})$ be the bilinear form related to the geometric stiffness as explained in Equation (2.23) of Chapter 2

$$k_g(\mathbf{u}, \mathbf{v}) = \int_{\mathcal{D}} u_{s,i} \sigma_{ij}^{\text{geom}} v_{s,j} d\mathbf{x} \quad . \quad (\text{A.3})$$

For each finite element, the corresponding stress state is given by

$$\begin{pmatrix} \sigma_{11}^{\text{geom}} \\ \sigma_{22}^{\text{geom}} \\ \sigma_{11}^{\text{geom}} \\ \sigma_{12}^{\text{geom}} \\ \sigma_{13}^{\text{geom}} \\ \sigma_{23}^{\text{geom}} \end{pmatrix} = [D][B(\boldsymbol{\xi})]\tilde{\mathbf{U}} \quad , \quad (\text{A.4})$$

where $\tilde{\mathbf{U}}$ is the \mathbb{R}^{3q} -vector of the displacements of the q nodes of a finite element, where $[D]$ is the (6×6) elasticity matrix of the finite element constituted of the components of the fourth-order elasticity tensor, and where $[B(\boldsymbol{\xi})]$ is the $(6 \times 3q)$ interpolation matrix for the constructed with the derivatives of the interpolation functions. The geometric stiffness matrix is then obtained by assembling each finite element contribution of the geometric stiffness matrix.

Appendix B

Table of patterns

Pattern number	Arrangement	Pattern number	Arrangement
\mathcal{P}_0	24A	\mathcal{P}_{26}	15B9A
\mathcal{P}_1	$(5A1B)_4$	\mathcal{P}_{27}	3B6A12B3A
\mathcal{P}_2	$(AB)_{12}$	\mathcal{P}_{28}	3A21B
\mathcal{P}_3	$(4A4B)_3$	\mathcal{P}_{29}	$3A3B(3A6B)_2$
\mathcal{P}_4	4A2B3A2B5A2B3A2B	\mathcal{P}_{30}	$(3A3B)_23A9B$
\mathcal{P}_5	$(3A3B)_4$	\mathcal{P}_{31}	$(6A6B)_2$
\mathcal{P}_6	$(4A2B)_4$	\mathcal{P}_{32}	3B9A9B3A
\mathcal{P}_7	$AB2A2B(AB)_22A2B2AAB2B(AB)_2$	\mathcal{P}_{33}	3B21A
\mathcal{P}_8	2ABA2B2A3B(AB) ₂ 2AB3A3B	\mathcal{P}_{34}	6A6B3A9B
\mathcal{P}_9	$(2A2B)_6$	\mathcal{P}_{35}	18A6B
\mathcal{P}_{10}	4A4B(2A2B) ₂ 2A6B	\mathcal{P}_{36}	3B12A3B6A
\mathcal{P}_{11}	B4AB18A	\mathcal{P}_{37}	3B6A3B3A6B3A
\mathcal{P}_{12}	12A12B	\mathcal{P}_{38}	6A8B3A6B
\mathcal{P}_{13}	6B12A3B3A	\mathcal{P}_{39}	9A3B3A9B
\mathcal{P}_{14}	3B15A3B3A	\mathcal{P}_{40}	3B9A3B3A3B3A
\mathcal{P}_{15}	6A3B6A9B	\mathcal{P}_{41}	3B6A6B3A3B3A
\mathcal{P}_{16}	$(3B6A)_23B3A$	\mathcal{P}_{42}	3B9A6B6A
\mathcal{P}_{17}	3A6B3A12B	\mathcal{P}_{43}	$(3A3B)_4$
\mathcal{P}_{18}	3B12A6B3A	\mathcal{P}_{44}	$(3A9B)_2$
\mathcal{P}_{19}	18A6B	\mathcal{P}_{45}	$(9A3B)_2$
\mathcal{P}_{20}	3B12A6B3A		
\mathcal{P}_{21}	6B9A6B3A		
\mathcal{P}_{22}	6A3B3A12B		
\mathcal{P}_{23}	9A3B6A6B		
\mathcal{P}_{24}	14A9B		
\mathcal{P}_{25}	3A3B3A15B		

Appendix C

Implementation of three 3D finite elements in the house-code

In the industrial context of this thesis, ANSYS software is the finite element code used by the industrial. Indeed, the numerical developments of this work require to have similar functionalities, since the industrial meshes are considered at the same time as entry for the ANSYS users and for the developed house-code. This section is devoted to a brief description of the implementation of the 3-D solid finite elements with quadratic interpolation used in the development of the house-code written using the MATLAB language. Three types of solide elements have been developed:

- hexahedral 20-node solid finite element.
- pyramidal 13-node solid finite element.
- tetrahedral 10-node solid finite element.

C.1 Hexahedral finite element with 20 nodes

The HEX20 isoparametric 3D finite element is constructed with quadratic interpolations [118, 123]. There are 20 nodes yielding 60 degrees of freedom for such solid finite element. Figure C.1 displays a representation of the 20-node hexahedral finite element. Let (ξ, η, ζ) be the coordinates in the cartesian coordinate system $(O, \vec{e}_\xi, \vec{e}_\eta, \vec{e}_\zeta)$ of the corresponding reference finite element which occupies the domain $\{[-1, 1] \times [-1, 1] \times [-1, 1]\}$.

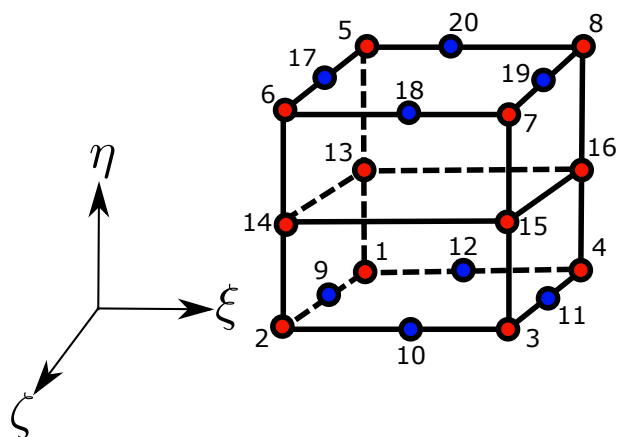


Figure C.1 – 20-node solid finite element.

C.1.1 Interpolation functions

Table C.1 summarizes the interpolation functions of the HEX20 finite element as functions of ξ, η, ζ .

$$\begin{aligned}
 N_1(\xi, \eta, \zeta) &= (1 - \xi)(1 - \eta)(1 - \zeta)(-2 - \xi - \eta - \zeta)/8 \\
 N_2(\xi, \eta, \zeta) &= (1 + \xi)(1 - \eta)(1 - \zeta)(-2 + \xi - \eta - \zeta)/8 \\
 N_3(\xi, \eta, \zeta) &= (1 + \xi)(1 + \eta)(1 - \zeta)(-2 + \xi + \eta - \zeta)/8 \\
 N_4(\xi, \eta, \zeta) &= (1 - \xi)(1 + \eta)(1 - \zeta)(-2 - \xi + \eta - \zeta)/8 \\
 N_5(\xi, \eta, \zeta) &= (1 - \xi)(1 - \eta)(1 + \zeta)(-2 - \xi - \eta + \zeta)/8 \\
 N_6(\xi, \eta, \zeta) &= (1 + \xi)(1 - \eta)(1 + \zeta)(-2 + \xi - \eta + \zeta)/8 \\
 N_7(\xi, \eta, \zeta) &= (1 + \xi)(1 + \eta)(1 + \zeta)(-2 + \xi + \eta + \zeta)/8 \\
 N_8(\xi, \eta, \zeta) &= (1 - \xi)(1 + \eta)(1 + \zeta)(-2 - \xi + \eta + \zeta)/8 \\
 N_9(\xi, \eta, \zeta) &= (1 - \xi^2)(1 - \eta)(1 - \zeta)/4 \\
 N_{10}(\xi, \eta, \zeta) &= (1 - \eta^2)(1 + \xi)(1 - \zeta)/4 \\
 N_{11}(\xi, \eta, \zeta) &= (1 - \xi^2)(1 + \eta)(1 - \zeta)/4 \\
 N_{12}(\xi, \eta, \zeta) &= (1 - \eta^2)(1 - \xi)(1 - \zeta)/4 \\
 N_{13}(\xi, \eta, \zeta) &= (1 - \zeta^2)(1 - \eta)(1 - \xi)/4 \\
 N_{14}(\xi, \eta, \zeta) &= (1 - \zeta^2)(1 + \xi)(1 - \eta)/4 \\
 N_{15}(\xi, \eta, \zeta) &= (1 - \zeta^2)(1 + \xi)(1 + \eta)/4 \\
 N_{16}(\xi, \eta, \zeta) &= (1 - \zeta^2)(1 + \eta)(1 - \xi)/4 \\
 N_{17}(\xi, \eta, \zeta) &= (1 - \xi^2)(1 - \eta)(1 + \zeta)/4 \\
 N_{18}(\xi, \eta, \zeta) &= (1 - \eta^2)(1 + \xi)(1 + \zeta)/4 \\
 N_{19}(\xi, \eta, \zeta) &= (1 - \xi^2)(1 + \eta)(1 + \zeta)/4 \\
 N_{20}(\xi, \eta, \zeta) &= (1 - \eta^2)(1 - \xi)(1 + \zeta)/4
 \end{aligned}$$

Table C.1 – Interpolation functions related to the HEX20 finite element

C.1.2 Numerical integration points

Table C.2 and Table C.3 give the integration points when using 27 Gauss integration points (complete integration) or 14 integration points (reduced integration used by ANSYS software). Note that the reduced numerical integration scheme allows the hourglass phenomenon to be avoided [40].

Point	ξ	η	ζ	Weight
1	$-\alpha$	$-\alpha$	$-\alpha$	c_1^3
2	$-\alpha$	$-\alpha$	0.	$c_1^2 c_2$
3	$-\alpha$	$-\alpha$	α	c_1^3
4	$-\alpha$	0.	$-\alpha$	$c_1^2 c_2$
5	$-\alpha$	0.	0.	$c_1 c_2^2$
6	$-\alpha$	0.	α	$c_1^2 c_2$
7	$-\alpha$	α	$-\alpha$	c_1^3
8	$-\alpha$	α	0.	$c_1^2 c_2$
9	$-\alpha$	α	α	c_1^3
10	0.	$-\alpha$	$-\alpha$	$c_1^2 c_2$
11	0.	$-\alpha$	0.	$c_1 c_2^2$
12	0.	$-\alpha$	α	$c_1^2 c_2$
13	0.	0.	$-\alpha$	$c_1 c_2^2$
14	0.	0.	0.	c_2^3
15	0.	0.	α	$c_1 c_2^2$
16	0.	α	$-\alpha$	$c_1^2 c_2$
17	0.	α	0.	$c_1 c_2^2$
18	0.	α	α	$c_1^2 c_2$
19	α	$-\alpha$	$-\alpha$	c_1^3
20	α	$-\alpha$	0.	$c_1^2 c_2$
21	α	$-\alpha$	α	c_1^3
22	α	0.	$-\alpha$	$c_1^2 c_2$
23	α	0.	0.	$c_1 c_2^2$
24	α	0.	α	$c_1^2 c_2$
25	α	α	$-\alpha$	c_1^3
26	α	α	0.	$c_1^2 c_2$
27	α	α	α	c_1^3

$$\begin{aligned} \alpha &= \sqrt{\frac{3}{5}} \\ \text{with } c_1 &= \frac{5}{9} \\ c_2 &= \frac{8}{9} \end{aligned}$$

Table C.2 – Localization of the 27 numerical integration points in the HEX20 finite element

Point	ξ	η	ζ	Weight
1	r	s	t	w_1
2	r	$-s$	t	w_1
3	r	$-s$	$-t$	w_1
4	r	s	$-t$	w_1
5	$-r$	s	t	w_1
6	$-r$	$-s$	t	w_1
7	$-r$	$-s$	$-t$	w_1
8	$-r$	s	$-t$	w_1
9	u	0	0	w_2
10	$-u$	0	0	w_2
11	0	$-v$	0	w_2
12	0	v	0	w_2
13	0	0	w	w_2
14	0	0	$-w$	w_2

with

$$\begin{aligned}
 r &= 0.758786910639329 \\
 s &= 0.758786910639329 \\
 t &= 0.758786910639329 \\
 u &= 0.795822425754222 \\
 v &= 0.795822425754222 \\
 w &= 0.795822425754222 \\
 w_1 &= 0.335180055401662 \\
 w_2 &= 0.886426592797784
 \end{aligned}$$

Table C.3 – Localization of the 14 numerical integration points in the HEX20 finite element

C.2 Pyramidal elements with 13 nodes

The PYR13 finite element is constructed with quadratic interpolations [118, 123]. There are 13 nodes yielding 39 degrees of freedom in this pyramidal element. Figure C.2 shows a representation of the 13-node pyramidal finite element. Let (ξ, η, ζ) be the coordinates in the cartesian coordinate systems $(O, \vec{e}_\xi, \vec{e}_\eta, \vec{e}_\zeta)$ of the corresponding reference finite element which occupies the domain $[-1, 1] \times [-1, 1]$ and for which $\zeta \in [0, 1]$.

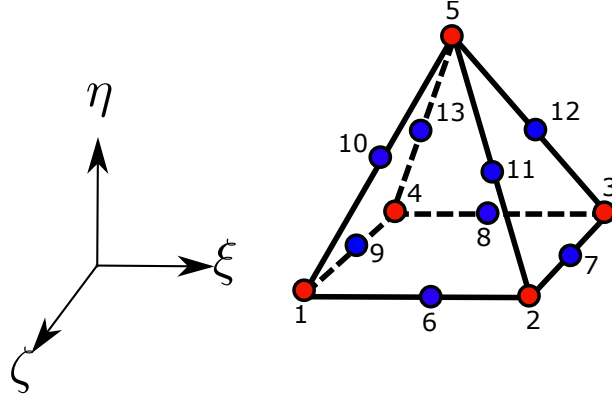


Figure C.2 – 13-node solid finite element

C.2.1 Interpolation functions

Table C.4 summarizes the interpolation functions of the PYR13 finite element as functions of ξ, η, ζ .

$$\begin{aligned}
 N_1(\xi, \eta, \zeta) &= ((-\xi + \eta + \zeta - 1)(-\xi - \eta + \zeta - 1)(\xi - 0.5))/(2(1 - \zeta)) \\
 N_2(\xi, \eta, \zeta) &= ((-\xi - \eta + \zeta - 1)(\xi - \eta + \zeta - 1)(\eta - 0.5))/(2(1 - \zeta)) \\
 N_3(\xi, \eta, \zeta) &= ((\xi - \eta + \zeta - 1)(\xi + \eta + \zeta - 1)(-\xi - 0.5))/(2(1 - \zeta)) \\
 N_4(\xi, \eta, \zeta) &= ((\xi + \eta + \zeta - 1)(-\xi + \eta + \zeta - 1)(-\eta - 0.5))/(2(1 - \zeta)) \\
 N_5(\xi, \eta, \zeta) &= 2\zeta(\zeta - 0.5) \\
 N_6(\xi, \eta, \zeta) &= -((-\xi + \eta + \zeta - 1)(-\xi - \eta + \zeta - 1)(\xi - \eta + \zeta - 1))/(2(1 - \zeta)) \\
 N_7(\xi, \eta, \zeta) &= -((-\xi - \eta + \zeta - 1)(\xi - \eta + \zeta - 1)(\xi + \eta + \zeta - 1))/(2(1 - \zeta)) \\
 N_8(\xi, \eta, \zeta) &= -((\xi - \eta + \zeta - 1)(\xi + \eta + \zeta - 1)(-\xi + \eta + \zeta - 1))/(2(1 - \zeta)) \\
 N_9(\xi, \eta, \zeta) &= -((\xi + \eta + \zeta - 1)(-\xi + \eta + \zeta - 1)(-\xi - \eta + \zeta - 1))/(2(1 - \zeta)) \\
 N_{10}(\xi, \eta, \zeta) &= (\zeta(-\xi + \eta + \zeta - 1)(-\xi - \eta + \zeta - 1))/((1 - \zeta)) \\
 N_{11}(\xi, \eta, \zeta) &= (\zeta(-\xi - \eta + \zeta - 1)(\xi - \eta + \zeta - 1))/((1 - \zeta)) \\
 N_{12}(\xi, \eta, \zeta) &= (\zeta(\xi - \eta + \zeta - 1)(\xi + \eta + \zeta - 1))/((1 - \zeta)) \\
 N_{13}(\xi, \eta, \zeta) &= (\zeta(\xi + \eta + \zeta - 1)(-\xi + \eta + \zeta - 1))/((1 - \zeta))
 \end{aligned}$$

Table C.4 – Interpolation functions related to the PYR13 finite element

C.2.2 Numerical integration points

The PYR13 numerical Gauss integration points are summarized in Table C.5.

Point	ξ	η	ζ	Weight
1	a	0.	h_1	p_1
2	0	a	h_1	p_1
3	$-a$	0.	h_1	p_1
4	0.	$-a$	h_1	p_1
5	0.	0.	h_2	p_2
6	0.	0.	h_3	p_3

$$\begin{aligned}
 p_1 &= 0.1024890634400000 \\
 p_2 &= 0.1100000000000000 \\
 p_3 &= 0.1467104129066667 \\
 \text{with } a &= 0.5702963741068025 \\
 h_1 &= 0.1666666666666666 \\
 h_2 &= 0.08063183038464675 \\
 h_3 &= 0.6098484849057127
 \end{aligned}$$

Table C.5 – Localization of the 6 numerical integration points in the PYR13 finite element

C.3 Tetrahedral element with 10 nodes

The TET10 finite element is constructed with quadratic interpolations [118, 123]. There are 10 nodes yielding 30 degrees of freedom in this tetrahedral element. Figure C.3 shows a representation of the 10-node pyramidal finite element. Let (ξ, η, ζ) be the coordinates in the cartesian coordinate systems $(O, \vec{e}_\xi, \vec{e}_\eta, \vec{e}_\zeta)$ of the corresponding reference finite element which occupies the domain $[0, 1] \times [0, 1] \times [0, 1]$.

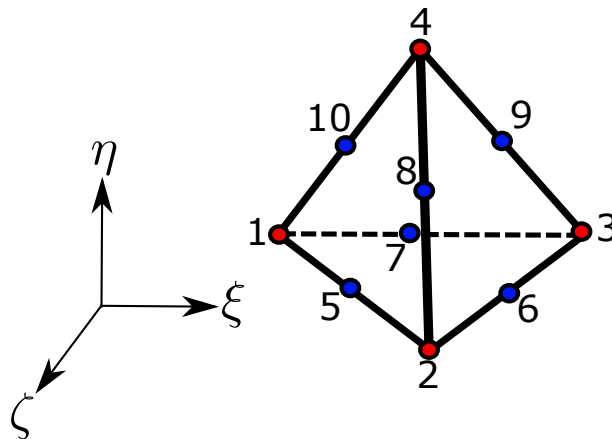


Figure C.3 – 10-node solid finite element

C.3.1 Interpolation functions

Table C.6 summarizes the interpolation functions of the TET10 finite element as functions of ξ, η, ζ .

C.3.2 Numerical integration points

The TET10 numerical Gauss integration points are summarized in Table C.7

$$\begin{aligned}
 N_1(\xi, \eta, \zeta) &= \eta(2\eta - 1) \\
 N_2(\xi, \eta, \zeta) &= \zeta(2\zeta - 1) \\
 N_3(\xi, \eta, \zeta) &= (1 - \xi - \eta - \zeta)(1 - 2\xi - 2\eta - 2\zeta) \\
 N_4(\xi, \eta, \zeta) &= \xi(2\xi - 1) \\
 N_5(\xi, \eta, \zeta) &= 4\eta\zeta \\
 N_6(\xi, \eta, \zeta) &= 4\zeta(1 - \xi - \eta - \zeta) \\
 N_7(\xi, \eta, \zeta) &= 4\eta(1 - \xi - \eta - \zeta) \\
 N_8(\xi, \eta, \zeta) &= 4\xi\eta \\
 N_9(\xi, \eta, \zeta) &= 4\xi\zeta \\
 N_{10}(\xi, \eta, \zeta) &= 4\xi(1 - \xi - \eta - \zeta)
 \end{aligned}$$

Table C.6 – Interpolation functions related to the TET10 finite element

Point	ξ	η	ζ	Weight
1	a	a	a	$\frac{1}{24}$
2	a	a	b	$\frac{1}{24}$
3	a	b	a	$\frac{1}{24}$
4	b	a	a	$\frac{1}{24}$

$$\text{with } \begin{aligned}
 a &= \frac{(5 - \sqrt{5})}{20} \\
 b &= \frac{(5 + 3\sqrt{5})}{20}
 \end{aligned}$$

Table C.7 – Localization of the 4 numerical integration points in the TET10 finite element

Bibliography

- [1] D. Hemberger, D. Filsinger, and H.-J. Bauer. Investigations on maximum amplitude amplification factor of real mistuned bladed structures. In *ASME Turbo Expo 2012: Turbine Technical Conference and Exposition*, pages 1041–1052. American Society of Mechanical Engineers, 2012.
- [2] M.P. Castanier and C. Pierre. Modeling and analysis of mistuned bladed disk vibration: current status and emerging directions. *Journal of Propulsion and Power*, 22(2):384–396, 2006.
- [3] M. Mbaye, C. Soize, J.-P. Ousty, and E. Capiez-Lernout. Robust analysis of design in vibration of turbomachines. *Journal of Turbomachinery*, 135(2):021008, 2013.
- [4] E.K. Armstrong. *An Investigation into the Coupling Between Turbine Disk and Blade Vibrations*. PhD thesis, University of Cambridge, 1956.
- [5] S.A. Tobias and R.N. Arnold. The influence of dynamical imperfection on the vibration of rotating disks. *Proceedings of the Institution of Mechanical Engineers*, 171(1):669–690, 1957.
- [6] D.S. Whitehead. Effect of mistuning on the vibration of turbo-machine blades induced by wakes. *Journal of Mechanical Engineering Science*, 8(1):15–21, 1966.
- [7] D.J. Ewins. The effects of detuning upon the forced vibrations of bladed disks. *Journal of Sound and Vibration*, 9(1):65–79, 1969.
- [8] R.C.F. Dye and T.A. Henry. Vibration amplitudes of compressor blades resulting from scatter in blade natural frequencies. *Journal of Engineering for Power*, 91(3):182–187, 1969.

- [9] Y.-J. Chan and D.J. Ewins. Management of the variability of vibration response levels in mistuned bladed discs using robust design concepts. part 2: tolerance design. *Mechanical Systems and Signal Processing*, 24(8):2792–2806, 2010.
- [10] C.H. Hodges. Confinement of vibration by structural irregularity. *Journal of Sound and Vibration*, 82(3):411–424, 1982.
- [11] C. Pierre. Mode localization and eigenvalue loci veering phenomena in disordered structures. *Journal of Sound and Vibration*, 126(3):485–502, 1988.
- [12] C-C Lin and M.P. Mignolet. An adaptive perturbation scheme for the analysis of mistuned bladed disks. *Journal of Engineering for Gas Turbines and Power*, 119(1):153–160, 1997.
- [13] D.S. Whitehead. The maximum factor by which forced vibration of blades can increase due to mistuning. *ASME Journal of Engineering for Gas Turbines and Power*, 120(1):115–119, 1998.
- [14] A.J. Rivas-Guerras and M.P. Mignolet. Local/global effects of mistuning on the forced response of bladed disks. In *ASME Turbo Expo 2001: Power for Land, Sea, and Air*, pages V004T01A002–V004T01A002. American Society of Mechanical Engineers, 2001.
- [15] P. Vargiu, C.M. Firrone, S. Zucca, and M.M. Gola. A reduced order model based on sector mistuning for the dynamic analysis of mistuned bladed disks. *International Journal of Mechanical Sciences*, 53(8):639–646, 2011.
- [16] W. Chen and C. Pierre. Vibration localization and wave conversion phenomena in a multi-coupled, nearly periodic, disordered truss beam. In *Dynamics Specialists Conference*, page 2115, Dallas, April 1992. AIAA.
- [17] S. Lust, P. Friedmann, and O. Bendiksen. Free and forced response of nearly periodic multi-span beams and multi-bay trusses. In *32nd Structures, Structural Dynamics, and Materials Conference*, page 999, Baltimore, April 1991. AIAA.
- [18] C. Pierre and E.H. Dowell. Localization of vibrations by structural irregularity. *Journal of Sound and Vibration*, 114(3):549–564, 1987.
- [19] C. Pierre and P.D. Cha. Strong mode localization in nearly periodic disordered structures. *AIAA journal*, 27(2):227–241, 1989.

-
- [20] H.P.W. Gottlieb. Extension of a text-book problem to curve veering for coupled pendulums. *Journal of Sound Vibration*, 113:185–187, 1987.
- [21] G. Ottarson and C. Pierre. On the effects of interblade coupling on the statistics of maximum forced response amplitudes in mistuned bladed disks. In *36th Structures, Structural Dynamics and Materials Conference*, page 1494. AIAA, April 1995.
- [22] J.H. Griffin and T.M. Hoosac. Model development and statistical investigation of turbine blade mistuning. *Journal of Vibration, Acoustics, Stress, and Reliability in Design*, 106(2):204–210, 1984.
- [23] M.P. Castanier and C. Pierre. Consideration on the benefits of intentional blade mistuning for the forced response of turbomachinery rotors. In *Analysis and Design Issues for Modern Aerospace Vehicles*, volume 55, pages 419–425, Dallas, November 1997. ASME.
- [24] M.P. Castanier and C. Pierre. Investigation of the combined effects of intentional and random mistuning on the forced response of bladed disks. In *34th AIAA/ASME/SAE/ASEE Joint Propulsion Conference and Exhibit*, page 3720, 1998.
- [25] M.P. Castanier and C. Pierre. Using intentional mistuning in the design of turbomachinery rotors. *AIAA journal*, 40(10):2077–2086, 2002.
- [26] H. Yiu and D.J. Ewins. Dependence on blade arrangements of mistuned bladed disc of the optimal and critical resonant responses. In *Rotating Machinery, Proceedings of the 6th International Symposium on Transport Phenomena and Dynamics of Rotating Machinery*, volume 1, pages 237–251, 1986.
- [27] A. Sinha. Computation of the maximum amplitude of a mistuned bladed disk assembly via infinity norm. *American Society of Mechanical Engineers, Aerospace Division (Publication) AD*, 55:427–432, 1997.
- [28] E.P. Petrov, R. Vitali, and R. Haftka. Optimization of mistuned bladed discs using gradient-based response surface approximations. In *41st Structures, Structural Dynamics, and Materials Conference and Exhibit*, page 1522, Atlanta, 2000. AIAA.

- [29] E.P. Petrov and D.J. Ewins. Search for the best blade arrangement in a mistuned bladed disc assembly. In *Proceedings of the 7th National Turbine Engine High Cycle Fatigue Conference*, Palm Beach Garden, 2002.
- [30] B-K. Choi, J. Lentz, A.J. Rivas-Guerra, and M.P. Mignolet. Optimization of intentional mistuning patterns for the reduction of the forced response effects of unintentional mistuning: Formulation and assessment. *Journal of Engineering for Gas Turbines and Power*, 125(1):131–140, 12 2002.
- [31] E.P. Petrov and D. Ewins. Analysis of the worst mistuning patterns in bladed disk assemblies. *Journal of Turbomachinery*, 125:623–631, 10 2003.
- [32] Y. Han, R. Murthy, M.P. Mignolet, and J. Lentz. Optimization of intentional mistuning patterns for the mitigation of the effects of random mistuning. *Journal of Engineering for Gas Turbines and Power*, 136(6):062505, 2014.
- [33] Yuanqiu Tan, Chaoping Zang, and E.P. Petrov. Mistuning sensitivity and optimization for bladed disks using high-fidelity models. *Mechanical Systems and Signal Processing*, 124:502–523, 2019.
- [34] B. Beirow, F. Figaschewsky, A. Kühhorn, and A. Bornhorn. Vibration analysis of an axial turbine blisk with optimized intentional mistuning pattern. *Journal of Sound and Vibration*, 442:11–27, 2019.
- [35] E. Capiez-Lernout, C. Soize, and M. Mbaye. Mistuning analysis and uncertainty quantification of an industrial bladed disk with geometrical nonlinearity. *Journal of Sound and Vibration*, 356:124–143, 2015.
- [36] A.S. Volmir. Flexible plates and shells (in russian), gos. *Iz. Tech. Th. Lit., Moscow*, 1956.
- [37] R.D. Wood and O.C. Zienkiewicz. Geometrically nonlinear finite element analysis of beams, frames, arches and axisymmetric shells. *Computers & Structures*, 7(6):725–735, 1977.
- [38] J.H. Argyris, P.C. Dunne, and D.W. Scharpf. On large displacement-small strain analysis of structures with rotational degrees of freedom. *Computer Methods in Applied Mechanics and Engineering*, 14(3):401–451, 1978.
- [39] K.J. Bathe and S. Bolourchi. Large displacement analysis of three-dimensional beam structures. *International Journal for Numerical Methods in Engineering*, 14(7):961–986, 1979.

-
- [40] T. Belytschko, J.S.-J. Ong, W.K. Liu, and J.M. Kennedy. Hourglass control in linear and nonlinear problems. *Computer Methods in Applied Mechanics and Engineering*, 43(3):251–276, 1984.
- [41] T. Belytschko, W.K. Liu, B. Moran, and K. Elkhodary. *Nonlinear Finite Elements for Continua and Structures*. John Wiley & sons, 2013.
- [42] J. Bonet and R.D. Wood. *Nonlinear Continuum Mechanics for Finite Element Analysis*. Cambridge university press, 1997.
- [43] R. De Borst, M.A. Crisfield, J.J.C. Remmers, and C.V. Verhoosel. *Nonlinear Finite Element Analysis of Solids and Structures*. John Wiley & Sons, 2012.
- [44] A.F. Vakakis. Dynamics of a nonlinear periodic structure with cyclic symmetry. *Acta Mechanica*, 95(1-4):197–226, 1992.
- [45] A. Picou, E. Capiiez-Lernout, C. Soize, and M. Mbaye. Effects of geometrical nonlinearities for a rotating intentionally mistuned bladed-disk. In *Conference on Noise and Vibration Engineering (ISMA 2018)*, pages 1–11. KU Leuven, 2018.
- [46] A. Picou, E. Capiiez-Lernout, C. Soize, and M. Mbaye. Robust dynamic analysis of detuned-mistuned rotating bladed disk with geometric nonlinearities. *Computational Mechanics*, pages 1–20, to appear, 2020.
- [47] S-T Wei and C. Pierre. Effects of dry friction damping on the occurrence of localized forced vibrations in nearly cyclic structures. *Journal of Sound and Vibration*, 129(3):397–416, 1989.
- [48] S. Nacivet, C. Pierre, F. Thouverez, and Louis Jézéquel. A dynamic lagrangian frequency–time method for the vibration of dry-friction-damped systems. *Journal of Sound and Vibration*, 265(1):201–219, 2003.
- [49] E. Ciğeroğlu and H.N. Özgüven. Nonlinear vibration analysis of bladed disks with dry friction dampers. *Journal of Sound and Vibration*, 295(3-5):1028–1043, 2006.
- [50] C. Joannin, B. Chouvion, F. Thouverez, M. Mbaye, and J.-P. Ousty. Nonlinear modal analysis of mistuned periodic structures subjected to dry friction. *Journal of Engineering for Gas Turbines and Power*, 138(7):072504, 2016.

- [51] T. Liu, D. Zhang, and Y. Xie. A nonlinear vibration analysis of forced response for a bladed-disk with dry friction dampers. *Journal of Low Frequency Noise, Vibration and Active Control*, page 1461348419834759, 2019.
- [52] W. Tang and B.I. Epureanu. Geometric optimization of dry friction ring dampers. *International Journal of Non-Linear Mechanics*, 109:40–49, 2019.
- [53] C. Touzé and M. Amabili. Nonlinear normal modes for damped geometrically nonlinear systems: Application to reduced-order modelling of harmonically forced structures. *Journal of Sound and Vibration*, 298(4-5):958–981, 2006.
- [54] M. Krack, L. Panning-von Scheidt, J. Wallaschek, C. Siewert, and A. Hartung. Reduced order modeling based on complex nonlinear modal analysis and its application to bladed disks with shroud contact. *Journal of Engineering for Gas Turbines and Power*, 135(10):102502, 2013.
- [55] W. Tang and B.I. Epureanu. Nonlinear dynamics of mistuned bladed disks with ring dampers. *International Journal of Non-Linear Mechanics*, 97:30–40, 2017.
- [56] S. Baek and B. Epureanu. Reduced-order models of blisks with small geometric mistuning. *Journal of Vibration and Acoustics*, 139(4):041003, 2017.
- [57] G. Battiato, C.M. Firrone, T.M. Berruti, and B.I. Epureanu. Reduced order modeling for multistage bladed disks with friction contacts at the flange joint. *Journal of Engineering for Gas Turbines and Power*, 140(5):052505, 2018.
- [58] M. Mitra and B.I. Epureanu. Dynamic modeling and projection-based reduction methods for bladed disks with nonlinear frictional and intermittent contact interfaces. *Applied Mechanics Reviews*, 2019.
- [59] S.M. Pourkiaee and S. Zucca. A reduced order model for nonlinear dynamics of mistuned bladed disks with shroud friction contacts. *Journal of Engineering for Gas Turbines and Power*, 141(1):011031, 2019.
- [60] A.A. Muravyov and S.A. Rizzi. Determination of nonlinear stiffness with application to random vibration of geometrically nonlinear structures. *Computers & Structures*, 81(15):1513–1523, 2003.

-
- [61] M.P. Mignolet, A. Przekop, S.A. Rizzi, and S.M. Spottswood. A review of indirect/non-intrusive reduced order modeling of nonlinear geometric structures. *Journal of Sound and Vibration*, 332(10):2437–2460, 2013.
- [62] R. Perez, X.Q. Wang, A. Matney, and M.P. Mignolet. Reduced order model for the geometric nonlinear response of complex structures. In *ASME 2012 International Design Engineering Technical Conferences and Computers and Information in Engineering Conference*, pages 599–613. American Society of Mechanical Engineers, 2012.
- [63] X.Q. Wang, R. Perez, and M.P. Mignolet. Nonlinear reduced order modeling of complex wing models. In *54th AIAA/ASME/ASCE/AHS/ASC Structures, Structural Dynamics, and Materials Conference*, page 1520, 2013.
- [64] X.Q. Wang, M.P. Mignolet, T. Eason, and S. Spottswood. Nonlinear reduced order modeling of curved beams: a comparison of methods. In *50th AIAA/ASME/ASCE/AHS/ASC Structures, Structural Dynamics, and Materials Conference 17th AIAA/ASME/AHS Adaptive Structures Conference 11th AIAA No*, page 2433, 2009.
- [65] R. Perez, X.Q. Wang, and M.P. Mignolet. Nonlinear reduced-order models for thermoelastodynamic response of isotropic and functionally graded panels. *AIAA journal*, 49(3):630–641, 2011.
- [66] R. Perez, X.Q. Wang, A. Matney, and M.P. Mignolet. Reduced order model for the geometric nonlinear response of complex structures. In *ASME 2012 International Design Engineering Technical Conferences and Computers and Information in Engineering Conference*, pages 599–613. American Society of Mechanical Engineers Digital Collection, 2013.
- [67] O. Thomas, A. Givois, A. Grolet, J.-F. Deü, C. Fuinel, F. Mathieu, B. Legrand, and L. Nicu. Finite elements based reduced order models for nonlinear dynamics of piezoelectric and dielectric laminated micro/nanostructures. In *EUROMECH Colloquium 603, Dynamics of micro and nano systems*, 2018.
- [68] D. Laxalde and F. Thouverez. Complex non-linear modal analysis for mechanical systems: Application to turbomachinery bladings with friction interfaces. *Journal of Sound and Vibration*, 322(4-5):1009–1025, 2009.

- [69] R. Lewandowski. Computational formulation for periodic vibration of geometrically nonlinear structures part 1: theoretical background. *International journal of solids and structures*, 34(15):1925–1947, 1997.
- [70] A. Grolet and F. Thouverez. Vibration analysis of a nonlinear system with cyclic symmetry. In *ASME Turbo Expo 2010: Power for Land, Sea, and Air*, pages 917–929. American Society of Mechanical Engineers, 2010.
- [71] A. Grolet and F. Thouverez. Free and forced vibration analysis of a nonlinear system with cyclic symmetry: Application to a simplified model. *Journal of Sound and Vibration*, 331(12):2911–2928, 2012.
- [72] A. Martin and F. Thouverez. Dynamic analysis and reduction of a cyclic symmetric system subjected to geometric nonlinearities. *Journal of Engineering for Gas Turbines and Power*, 141(4):041027, 2019.
- [73] S.R. Idelsohn and A. Cardona. A reduction method for nonlinear structural dynamic analysis. *Computer Methods in Applied Mechanics and Engineering*, 49(3):253–279, 1985.
- [74] P.M.A. Slaats, J. De Jongh, and A.A.H.J. Sauren. Model reduction tools for nonlinear structural dynamics. *Computers & structures*, 54(6):1155–1171, 1995.
- [75] A. Givois, A. Grolet, O. Thomas, and J.-F. Deü. On the frequency response computation of geometrically nonlinear flat structures using reduced-order finite element models. *Nonlinear Dynamics*, pages 1–35, 2018.
- [76] M. Loève. Probability theory. 1963. *Russian translation*, 1955.
- [77] P. Holmes, J.L. Lumley, G. Berkooz, and C.W. Rowley. *Turbulence, coherent structures, dynamical systems and symmetry*. Cambridge university press, 1997.
- [78] K. Kunisch and S. Volkwein. Galerkin proper orthogonal decomposition methods for parabolic problems. *Numerische mathematik*, 90(1):117–148, 2001.
- [79] M.F.A. Azeez and A.F. Vakakis. Proper orthogonal decomposition (pod) of a class of vibroimpact oscillations. *Journal of Sound and vibration*, 240(5):859–889, 2001.

-
- [80] K. Kunisch and S. Volkwein. Galerkin proper orthogonal decomposition methods for a general equation in fluid dynamics. *SIAM Journal on Numerical analysis*, 40(2):492–515, 2002.
- [81] M. Meyer and H.G. Matthies. Efficient model reduction in non-linear dynamics using the karhunen-loeve expansion and dual-weighted-residual methods. *Computational Mechanics*, 31(1-2):179–191, 2003.
- [82] R. Sampaio and C. Soize. Remarks on the efficiency of pod for model reduction in non-linear dynamics of continuous elastic systems. *International Journal for Numerical Methods in Engineering*, 72(1):22–45, 2007.
- [83] F.A. LülF, D.M. Tran, and R. Ohayon. Reduced bases for nonlinear structural dynamic systems: A comparative study. *Journal of Sound and Vibration*, 332(15):3897–3921, 2013.
- [84] F. Adrian LülF, D.M. Tran, H.G. Matthies, and R. Ohayon. An integrated method for the transient solution of reduced order models of geometrically nonlinear structures. *Computational Mechanics*, 55(2):327–344, 2015.
- [85] M.B. Aguirre, G. Jacquet-Richardet, A. Placzek, and D.M. Tran. Reduced order models for dynamic analysis of nonlinear rotating structures. In *ECCM-ECFD Conferences 2018*, 2018.
- [86] T. Hui, L. Wang, S. Chakrabarti, S. Ashar, S. Szczap, and A. Laude. Non-linear cyclic transient dynamic analysis for bladed disk tip deflection. In *16th International Symposium on Transport Phenomena and Dynamics of Rotating Machinery (ISROMAC 2016)*, 2016.
- [87] C.C. Huang, W.Y. Lin, F. Fujii, and K.M. Hsiao. An explicit method for geometrically nonlinear dynamic analysis of spatial beams. In *Proceedings of the World Congress on Engineering*, volume 2, 2015.
- [88] E. Capiez-Lernout, C. Soize, and R. Ohayon. Uncertainty quantification for an elasto-acoustic nonlinear reduced-order computational model. *Procedia engineering*, 199:1204–1209, 2017.
- [89] E. Capiez-Lernout, C. Soize, and M.P. Mignolet. Computational stochastic statics of an uncertain curved structure with geometrical nonlinearity in three-dimensional elasticity. *Computational Mechanics*, 49(1):87–97, 2012.

- [90] L.N. Shang, X.I.A. Pinqi, and D. H. Hodges. Geometrically exact nonlinear analysis of pre-twisted composite rotor blades. *Chinese Journal of Aeronautics*, 31(2):300–309, 2018.
- [91] M.P. Mignolet and C. Soize. Stochastic reduced order models for uncertain geometrically nonlinear dynamical systems. *Computer Methods in Applied Mechanics and Engineering*, 197(45-48):3951–3963, 2008.
- [92] M.P. Mignolet, W. Hu, and I. Jadic. On the forced response of harmonically and partially mistuned bladed disks. part 2: partial mistuning and applications. *International Journal of Rotating Machinery*, 6(1):43–56, 2000.
- [93] M.P. Mignolet, A.J. Rivas-Guerra, and J.P. Delor. Identification of mistuning characteristics of bladed disks from free response data -part 1. *Journal of Engineering for Gas Turbines and Power*, 123(2):395–403, 2001.
- [94] J. M. Brown, J. Slater, and R.V. Grandhi. Probabilistic analysis of geometric uncertainty effects on blade modal response. In *ASME Turbo Expo 2003, collocated with the 2003 International Joint Power Generation Conference*, pages 247–255. American Society of Mechanical Engineers, 2003.
- [95] S.-Y. Lee, M. Castanier, and C. Pierre. Assessment of probabilistic methods for mistuned bladed disk vibration. In *46th AIAA/ASME/ASCE/AHS/ASC Structures, Structural Dynamics and Materials Conference*, page 1990, 2005.
- [96] E. Capiez-Lernout and C. Soize. Nonparametric modeling of random uncertainties for dynamic response of mistuned bladed-disks. *Journal of Engineering for Gas Turbines and Power*, 126(3):610–618, 2004.
- [97] E. Capiez-Lernout, C. Soize, J.-P. Lombard, C. Dupont, and E. Seinturier. Blade manufacturing tolerances definition for a mistuned industrial bladed disk. *ASME Journal of Engineering for Gas Turbines and Power*, 127(2), 2005.
- [98] F. Nyssen, M. Arnst, and J.-C. Golinval. Modeling of uncertainties in bladed disks using a nonparametric approach. In *ASME 2014 International Design Engineering Technical Conferences and Computers and Information in Engineering Conference*, pages V008T11A068–V008T11A068. American Society of Mechanical Engineers, 2014.
- [99] C. Soize. *Uncertainty Quantification: An Accelerated Course with Advanced Applications in Computational Engineering*. Springer, 2017.

-
- [100] Y. Han and M.P. Mignolet. Optimization of intentional mistuning patterns for the mitigation of the effects of random mistuning. In *ASME Turbo Expo 2008: Power for Land, Sea, and Air*, pages 601–609. American Society of Mechanical Engineers, 2008.
- [101] E. Capiez-Lernout and C. Soize. An improvement of the uncertainty quantification in computational structural dynamics with nonlinear geometrical effects. *International Journal for Uncertainty Quantification*, 7(1):83–98, 2017.
- [102] E. Capiez-Lernout. *Dynamique des Structures Tournantes à Symétrie Cyclique en Présence d’Incertitudes Aléatoires: application au Désaccordage des Roues Aubagées*. PhD thesis, Université de Marne-la-Vallée, 2004.
- [103] M. Mbaye. *Conception Robuste en Vibration et Aéroélasticité des Roues Aubagées de Turbomachines*. PhD thesis, Université Paris-Est, 2009.
- [104] C. Soize. A nonparametric model of random uncertainties for reduced matrix models in structural dynamics. *Probabilistic Engineering Mechanics*, 15(3):277–294, 2000.
- [105] R. Henry. Calcul des fréquences et modes propres des structures répétitives circulaires. *Journal de Mécanique Appliquée*, 4(1):61–82, 1980.
- [106] R. Valid and R. Ohayon. Static and dynamic analysis of cyclically symmetric structures. *La Recherche Aérospatiale (english edition)*, 4:41–53, 1985.
- [107] D.L. Thomas. Dynamics of rotationally periodic structures. *International Journal for Numerical Methods in Engineering*, 14(1):81–102, 1979.
- [108] C. Desceliers and C. Soize. Nonlinear viscoelastodynamic equations of three-dimensional rotating structures in finite displacement and finite element discretization. *International Journal of Nonlinear Mechanics*, 39:343–368, 2004.
- [109] F.F. Ehrlich. *Handbook of Rotordynamics*. Number BOOK. Krieger, 1999.
- [110] JS Rao. *History of Rotating Machinery Dynamics*, volume 20. Springer Science & Business Media, 2011.
- [111] G. Genta. *Vibration of structures and machines: practical aspects*. Springer Science & Business Media, 2012.

- [112] O.C. Zienkiewicz and R. L. Taylor. *The finite element method*, volume 3. McGraw-hill London, 1977.
- [113] T.J.R. Hughes. *The Finite Element Method: Linear Static and Dynamic Finite Element Analysis*. Courier Corporation, 2012.
- [114] K.-J. Bathe and E.L. Wilson. *Numerical methods in finite element analysis*. Prentice Hall, New York, 1976.
- [115] M.A. Crisfield. *Non-linear finite element analysis of solids and structures*, volume 1. Wiley New York, 1993.
- [116] G.H. Golub and C.F. Van Loan. *Matrix Computations*, volume 3. Johns Hopkins University Press, 2012.
- [117] G.J. DeSalvo and J.A. Swanson. Ansys user's manual. *Swanson Analysis Systems*, 1989.
- [118] ASTER Manual. Shape functions and points of integration of the finite elements. *SAS IP inc*, 1998.
- [119] N. M. Newmark et al. A method of computation for structural dynamics. American Society of Civil Engineers, 1959.
- [120] M.A. Crisfield. An arc-length method including line searches and accelerations. *International Journal for Numerical Methods in Engineering*, 19(9):1269–1289, 1983.
- [121] E.T. Jaynes. Information theory and statistical mechanics. *Physical Review*, 106(4):620–630, 1957.
- [122] C.E. Shannon. A mathematical theory of communication. *Bell System Technology Journal*, pages 379–423 and 623–659, 1948.
- [123] G. Dhatt and G. Touzot. *Une Présentation de la Méthode des Eléments Finis*. Presses Université Laval, 1981.